

LA-UR-21-28568

Accepted Manuscript

Analytic model of dislocation density evolution in fcc polycrystals accounting for dislocation generation, storage, and dynamic recovery mechanisms

Hunter, Abigail
Preston, Dean Laverne

Provided by the author(s) and the Los Alamos National Laboratory (2022-04-21).

To be published in: International Journal of Plasticity

DOI to publisher's version: 10.1016/j.ijplas.2021.103178

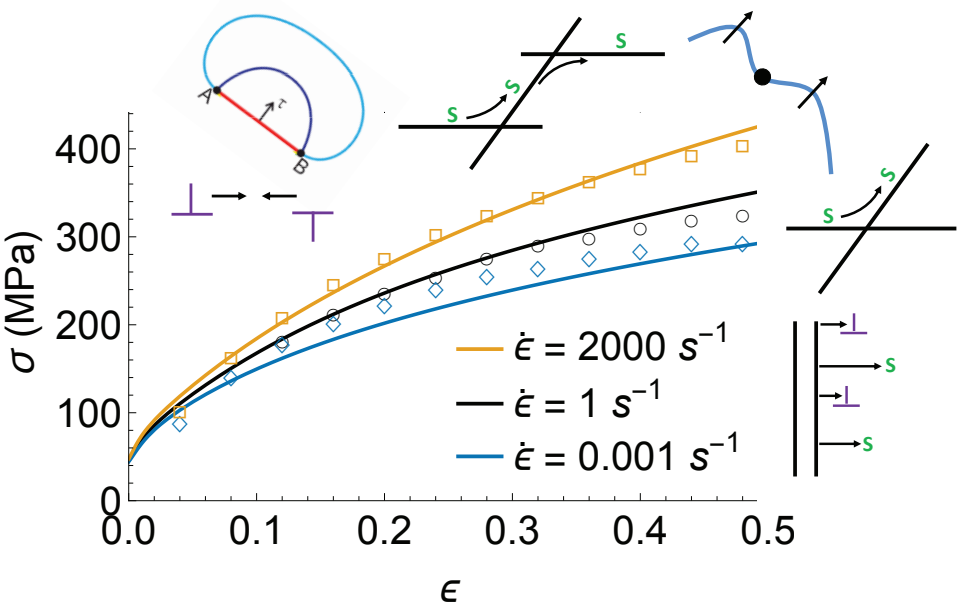
Permalink to record:

<http://permalink.lanl.gov/object/view?what=info:lanl-repo/lareport/LA-UR-21-28568>



Los Alamos National Laboratory, an affirmative action/equal opportunity employer, is operated by Triad National Security, LLC for the National Nuclear Security Administration of U.S. Department of Energy under contract 89233218CNA000001. By approving this article, the publisher recognizes that the U.S. Government retains nonexclusive, royalty-free license to publish or reproduce the published form of this contribution, or to allow others to do so, for U.S. Government purposes. Los Alamos National Laboratory requests that the publisher identify this article as work performed under the auspices of the U.S. Department of Energy. Los Alamos National Laboratory strongly supports academic freedom and a researcher's right to publish; as an institution, however, the Laboratory does not endorse the viewpoint of a publication or guarantee its technical correctness.

Graphical Abstract



Highlights

- Analytic model for the evolution of mobile/immobile dislocation densities is presented.
- Equations account for dislocation storage, dynamic recovery, and generation mechanisms.
- Model results for copper are compared to experimental data.
- Results are presented for varying temperatures and strain rates.

Analytic model of dislocation density evolution in *fcc* polycrystals accounting for dislocation generation, storage, and dynamic recovery mechanisms

Abigail Hunter^{1,*} and Dean L. Preston¹

¹X Computational Physics, Los Alamos National Laboratory, Los Alamos, NM

January 19, 2022

Abstract

An analytic model of the evolution of dislocation density in *fcc* polycrystals is described. The evolution equations approximately account for most known dislocation storage, dynamic recovery, and dislocation generation mechanisms in *fcc* polycrystals. Specifically, the model incorporates network (forest) and grain boundary storage, mobile-network and mobile-mobile annihilation, screw-screw annihilation via athermal and thermal single cross-slip, generation by double cross-slip (Koehler mechanism, including dipole formation), Frank-Read sources, grain boundary nucleation, and mobile-immobile dislocation nucleation due to shock loading. Single cross-slip is assumed to proceed through the Friedel-Escaig (FE) mechanism; the corresponding activation energy is calculated using a modified FE model. The activation energy for double cross-slip is calculated for the first time by extending the FE model. The exact evolution equations are integro-differential equations, and as such are difficult to implement in a code; hence, the evolution equations are simplified by making several approximations. Preliminary results on copper are presented, including comparisons to experimental data.

Keywords— dislocations, constitutive behavior, analytic functions, strengthening mechanisms, rate-dependent material

1 Introduction

It is well-known that dislocations mediate plastic flow in metals. While it is widely accepted that mobile-immobile (network or forest) dislocation intersection is the predominant rate-controlling mechanism in face-centered cubic (*fcc*) metals at low to modest strain rates for temperatures of order 300 K and higher (Friedel, 1964), many additional dislocation mechanisms have been observed experimentally. This includes dislocation multiplication via Frank-Read (FR) sources (Dehm, Legros,

and Heiland, 2006; Zhou, Huang, Sha, Xiao, Ma, Werner Höppel, Göken, Wu, Ameyama, Han, and Zhu, 2019), thermal and athermal cross-slip behavior (Oh, Legros, Kiener, and Dehm, 2009; Kim, Park, Park, Jang, Moon, Ha, Lee, Kang, Shin, and Lee, 2019), dislocation interaction with grain boundaries (Kacher, Eftink, Cui, and Robertson, 2014), including nucleation/emission, pileups, and absorption or storage mechanisms, in addition to annihilation between mobile-mobile and mobile-immobile dislocation populations. Transitions in these mechanisms as strain accumulates within a material is responsible for changes in the overall hardening response, and is often classified by stage I (unobstructed or ‘easy’ glide of dislocations), stage II (athermal, linear hardening) and stage III (dynamic recovery, in which the hardening rate starts to decrease) hardening (Rollet and Kocks, 1993; Püschl, 2002; Kocks and Mecking, 2003; Hughes and Hansen, 2018). Furthermore, microstructure, namely variation in grain size and morphology, is also known to play a significant role on material behavior (Mao, An, Z., and Wang, 2018; Dou, Wang, Geng, and Fan, 2019; Hansen and Ralph, 1982). Finally, variations in temperature, pressure, and strain rate can both impact currently operative mechanisms, and initiate new mechanisms, resulting in notable changes in the mechanical response (Oh et al., 2009; Remington, Allen, Bringa, Hawreliak, Ho, Lorenz, Lorenzana, McNaney, Meyers, Pollaine, Rosolankova, Sadik, Schneider, Swift, Wark, and Yaakobi, 2006; Kanel, Zaretsky, Razorenov, Ashitkov, and Fortov, 2017; Yaghoobi and Voyiadjis, 2018; Ravindran, Gandhi, Lovinger, Mello, and Ravichandran, 2001). Overall this presents an incredibly complex picture of how dislocations collectively evolve to produce the mechanical response of metals.

Due to the importance of structural materials within our community, it is no surprise that there have been many efforts to understand and model these underlying deformation mechanisms so that the corresponding material response can be predicted with high accuracy. Of course, thinking of the possible defects and mechanisms along with capturing the overall material response of a component or structure, this quickly becomes a problem that reaches across a wide range of length and time scales. Thus, there are valuable approaches that are operative on vastly different time/length scales that span this range, and also connect to each other in multi-scale efforts (Bertin, Sills, and Cai, 2020). At the smallest of scales there are atomistic approaches including Density Functional Theory (DFT), Molecular Statics (MS), and Molecular Dynamics (MD) (Rodney, Ventelon, Clouet, Pizzagalli, and Willaime, 2017; Aitken, Sorkin, and Zhang, 2019; Deo, Chen, and Dingreville, 2021). These approaches resolve every atom within a system and can investigate a wide variety of detailed defect physics. While these simulations are limited to small time durations and relatively small samples, they can provide a wealth of information about active deformation mechanisms within metals, in addition to providing key quantities for use in larger length scale models such as lattice parameters, elastic moduli, material γ -surfaces, activation energies etc. Moving up in time and length scales, there are also a class of mesoscale approaches, that no longer resolve individual atoms, but rather resolve individual defects of interest; in this case dislocations. Models at this scale include 2D and 3D Discrete Dislocation Dynamics (Po, Mohamed, Crosby, Erel, El-Azab, and Ghoniem, 2014; Lavenstein and El-Awady, 2019; Bertin and Capolungo, 2018), Phase Field (PF) approaches (Rodney, Le Bouar, and Finel, 2003; Beyerlein and Hunter, 2016; Mianroodi and Svendsen, 2015; Ruffini, Le Bouar, and Finel, 2017; Hunter, Leu, and Beyerlein, 2018), and Peierls-Nabarro (PN) approaches (Liu, Cheng, Wang, Chen, and Shen, 2017; Schoeck, 1994; Xiang, Wei, Ming, and Weinan, 2008), among others. While mesoscale approaches can model longer time frames and larger sample sizes in comparison to atomistic methods, these scales are not still not large enough to model realistic, bulk component sizes. However, simulated specimens are at length/time scales much closer to those used in small-scale experiments allowing for more direct comparison to experimental data (Lavenstein and El-Awady, 2019). Mesoscale approaches can still provide detailed information of both individual and collective dislocation motion and interaction with other dislocations and/or

microstructural features (Cao, Hunter, Beyerlein, and Koslowski, 2015; Chakraborty, Ma, Cui, Hunter, and Cao, 2021). Most parameters needed in these approaches can be directly informed by atomistic simulations (Hunter, Zhang, and Beyerlein, 2014; Kim, Mathew, Luscher, and Hunter, 2021), and depending on the problem, direct comparison can be made between atomistic and mesoscale simulations (Fan, Wang, El-Awady, Raabe, and Zaiser, 2021). The mesoscale approaches can also inform upwards, passing key information to larger length scale models. Again, moving up in time/length scales, models such as Crystal Plasticity (CP) (Luscher, Mayeur, Mourad, Hunter, and Kenamond, 2016; Mayeur, Mourad, Luscher, Hunter, and Kenamond, 2016) and Continuum Dislocation Dynamics (CDD) (Sandfeld, Thawinan, and Wieners, 2015; Starkey, Winther, and El-Azab, 2020; El-Azab and Po, 2018), become operative. In these models, dislocation densities are resolved rather than individual dislocations or individual atoms. In most cases, dislocation densities are evolved on separate active slip systems of interest, but can also be resolved in other ways depending on the framework (Nguyen, Zhang, Amores, Sanz, and Montans, 2021a). While this allows for much more realistic samples to be modeled, for example sizes on the scale of experimental test specimens (Nguyen, Fensin, and Luscher, 2021b; Yaghoobi, Voyiadjis, and Sundararaghavan, 2021), these approaches are still typically too resolved to reach length scales needed to design and model components since individual slip systems and microstructure, such as grain boundaries, are explicitly resolved. It is worth noting that the multiscale nature of this problem can also be addressed different ways. It has already been mentioned that information may be passed between different approaches in an effort to better inform larger length scale models. Conversely, there has also been development of concurrent approaches where models operative at different length and time scales are combined into a single simulation framework (Xu and Chen, 2019). Finally, this discussion leads us to models operative at the largest of length and time scales, which may evolve the plastic strain or mobile, immobile, or total dislocation densities, but information about the crystallography (such as individual slip systems), or the microstructure (such as grain boundaries) are not explicitly accounted for. Development of a model at this length scale is the primary focus of the current effort.

Capturing the evolution of the dislocation collective as a function of temperature and strain rate has been a challenge for continuum scale material models for some time now. Traditionally, many efforts developed phenomenological relationships between the material flow stress as a function of temperature and strain rate, and these are now commonly used, trusted models (Preston, Tonks, and Wallace, 2003; Follansbee and Kocks, 1988; Steinberg, Cochran, and Guinan, 1980; Zerilli and Armstrong, 1987; Nemat-Nasser and Li, 1998; Rusinek and Klepaczko, 2001; Sung, Kim, and Wagoner, 2010; Khan and Liu, 2012) (see also review by Salvado, Teixeira-Dias, Walley, Lea, and Cardoso (2017)). One common feature of these phenomenological models is that dislocations are not explicitly accounted for in any way, even in terms of dislocation density evolution. Rather than accounting for dislocation mechanisms explicitly, the effect of deformation mechanisms is, in essence, averaged, resulting in a need for several material-dependent parameters that are informed through fits to experimental data. Thanks to a vast number of experimental studies along with many computational studies at micro- and meso- scales, we have an understanding of many of the specific dislocation mechanisms that occur in *fcc* metals under a wide range of accessible loading conditions, including those just mentioned. Thus, much effort has been invested into the development of continuum constitutive models that explicitly include evolution of dislocation densities, although approaches can be quite varied.

Many approaches are built upon the framework developed by Kocks and Mecking (2003), which includes evolution of the total dislocation density and accounts for storage and dynamic recovery. While some approaches consider only the average dislocation density evolution (Kreyca and

Kozeschink, 2018), others consider two dislocation density populations, namely mobile and immobile populations (Roters, Raabe, and Gottstein, 2000; Shanthraj and Zikry, 2011; Zikry and Kao, 1996), which can then be extended to evolve on multiple active individual slip systems within the model (Ma and Roters, 2004). The mechanisms tied to the evolution of the mobile and immobile dislocation densities vary from model to model depending on the problem of interest, but typically include a term to account for some form of mobile dislocation generation (i.e., nucleation and/or multiplication) and also annihilation of both mobile and immobile dislocations. In addition, there is typically a coupling term in which mobile dislocation can be immobilized, generally accounting for the formation of junctions, locks, and/or trapping mechanisms. A majority of these models only consider relatively low strain rates (i.e., remaining in the thermally activated regime) due to their problems of interest. However, there has been some development of models that consider a wider range of strain rates (Austin and McDowell, 2011, 2012; Gao and Zhang, 2012; Rodríguez-Martínez, Rodríguez-Millán, Rusinek, and Arias, 2011; Lloyd, Clayton, Becker, and McDowell, 2014; Djordjevic, Vignjevic, Kiely, Case, De Vuyst, Campbell, and Hughes, 2018). Again, varying approaches are taken regarding the dislocation density evolution including evolving one (i.e., total or mobile dislocations) (Gao and Zhang, 2012; Rodríguez-Martínez et al., 2011) or two (i.e., mobile and immobile) dislocation populations (Austin and McDowell, 2011, 2012; Lloyd et al., 2014; Djordjevic et al., 2018).

While this previous work has accounted for dislocation density evolution in constitutive models, the mechanisms are typically grouped into broad classes such as nucleation, multiplication, and annihilation. The focus of this work is to develop continuum-scale expressions, including temperature and strain-rate dependence, for explicit dislocation mechanisms known to be operative in metals. More specifically, for dislocation generation mechanisms, we develop analytic terms that account for FR sources, dislocation generation via double cross-slip (i.e., the Koehler mechanism) (Koehler, 1952), nucleation of mobile dislocation from grain boundaries, and shock wave induced dislocation generation. Most of these terms are formulated so that they capture complex interactions between the mobile and immobile dislocation populations, thus generating both mobile and immobile dislocation densities. For example, in the case of FR sources, mobile dislocations are generated, propagate through the materials until they pile-up, which then creates a back stress that can eventually ‘turn off’ the FR source (Zhou et al., 2019; Motz, Schöberl, and Pippan, 2005). While mobile dislocations are initially generated, when the pile-up forms the piled-up dislocations go from mobile to immobile, hence the FR source can generate both mobile and immobile dislocations, a phenomenon captured within this model. In the case of dynamic recovery, this model includes single cross-slip (thermal and athermal terms), screw-screw annihilation, and annihilation between mobile-immobile and mobile-mobile dislocation populations. Finally, storage mechanisms include storage within the network and within grain boundaries. Because several of these terms are accounting for dislocation-grain boundary interaction, the overall evolution equations do depend on an average grain size, a dependency not considered in more traditional continuum-scale plasticity models (Preston et al., 2003; Follansbee and Kocks, 1988; Steinberg et al., 1980; Zerilli and Armstrong, 1987).

We specifically focus our formulation on *fcc* metals since they have been studied in depth and dislocation mechanisms as a function of temperature and strain rate are relatively well-known. Consequently, some of our terms account for *fcc*-specific mechanisms, such as cross-slip which is assumed to occur via the Friedel-Escaig mechanism. However, other terms may be more broadly applicable and determining this could be subject for future work. Broadly speaking the evolution equations proposed in this work are of the form:

$$\begin{aligned}
\dot{\rho}_m &= f_m(\hat{\sigma}, \dot{\epsilon}, \rho_m, \rho_i, \rho, T) \\
\dot{\rho}_i &= f_i(\hat{\sigma}, \dot{\epsilon}, \rho_m, \rho_i, \rho, T).
\end{aligned}
\tag{1}$$

Here ρ_m and ρ_i are, respectively, the mobile (m) and immobile (i) dislocation densities, $\dot{\epsilon}$ is the equivalent plastic strain rate, ρ is the material density, T is the temperature, and $\hat{\sigma}$ is the effective applied stress, which is defined as the difference between the applied von Mises stress, σ , and the back stress, σ_b ; $\hat{\sigma} = 0$ for $\sigma < \sigma_b$ (Hunter and Preston, 2015). The evolution equations are designed to be applicable over a wide range of strain rates (up to roughly 10^{10} s^{-1}), and at pressures up to 1000 GPa, hence the explicit dependence on the material density; specifically, the shear modulus, the Burgers vector, b , and stacking fault energies are functions of ρ , and in later equations this density dependence can also be indicated through a dependence on time, i.e., $b(t)$ may be used rather than $b(\rho)$. We also note here, that the evolution equations do rely on a set of coefficients indicated by $g_{\text{subscript}}$, where the *subscript* indicates the dislocation mechanism with which the parameter is associated. Since the model does not explicitly account for the material’s crystallography including individual slip systems and their geometry, and dislocation character, it is difficult to move away from fitting parameters entirely at the macroscale. However, these parameters can be approximated, which is discussed in more detail with the development of the evolution equations.

We should mention that the immobile dislocations in this model do not include geometrically necessary dislocations (GND) (Ashby, 1970; Kubin and Mortensen, 2003), only statistically stored dislocations (SSD). GNDs accumulate in strain gradient fields that are present, in particular, in polycrystals because of the intragranular misorientations (Jiang, Britton, and Wilkinson, 2012, 2013). The GND density is given by $\rho_{\text{GND}} = \epsilon/4bD$, where ϵ is the plastic strain and D is the mean grain diameter (Courtney, 2005). For example, a 50% strain of a 50 micron grain material results in a GND density of $10^{10}/\text{cm}^2$, which may be $\sim 10\%$ of the SSD density. We note that the model presented here does not account for lattice curvature or strain gradients, hence there is no need to employ a local (Das, Hofman, and Tarleton, 2018) or non-local (Xu, 2021) methodology to compute the Nye tensor (Nye, 1953) which yields the components of the GND density tensor. While the contribution of GNDs to the total dislocation density may seem relatively low, they are typically important indicators for microstructural ‘hotspots’ in which damage may eventually nucleate. For example, such correlations have been investigated in the development of fatigue cracks, particularly in nickel-based superalloys in which very hard non-metallic inclusions may be present (Zhang, Jiang, Shollock, Britton, and Dunne, 2015; Chen, Jiang, and Dunne, 2018). The model presented here is primarily focusing on capturing hardening behavior (largely due to SSDs) in a computationally efficient manner such that large samples or components can be modeled. Thus, a material’s microstructure, comprised of grain boundaries, triple junctions, inclusions, etc., is not explicitly accounted for. This, along with neglecting a GND density, would not allow for the identification of ‘hotspots’ for damage nucleation without further resolving the model. However, as described by Ashby (1970), when the GND density is large it contributes to hardening by generating a long-range back stress. A model for the back stress is utilized within this model (described later in Section 5.3), and the back stress can impact the dislocation density evolution. While this model is not explicitly dependent on a GND density, the effect is accounted for, and more sophisticated models could be employed.

In order to produce a complete material model, the evolution equations, Equation (1), must be used in conjunction with a kinetic equation relating the plastic strain rate to the flow stress:

$$\dot{\epsilon} = f(\hat{\sigma}, \rho_m, \rho_i, \rho, T). \quad (2)$$

Thus, this work builds on previous effort in which we developed such a kinetic equation using a mean-first-passage-time (MFPT) framework (Hunter and Preston, 2015). Our kinetic equation is a generalization of the standard low-strain-rate van't Hoff-Arrhenius form, $\dot{\epsilon} = \dot{\epsilon}_0 \exp(-E(\sigma)/k_B T)$ (Arrhenius, 1889), to very high stresses and plastic strain rates. The kinetic equation accounts for the dissolution of mobile-immobile dislocation intersections via thermal activation at low to moderate strain rates in addition to the effects of dislocation drag on mobile dislocations, which is the rate-limiting effect at moderate to high strain rates. Hence, the dislocation evolution equations formulated in this work do not account for the dissolution of junctions, as this mechanism is captured in the kinetic equation. In addition, effects of variation in temperature and material density on the glide velocity of mobile dislocations is captured with the kinetic equation, and is therefore, not included in the dislocation density evolutions. Furthermore, due to the MFPT framework on which the model is based, a smooth transition between the thermally activated and drag dominated regimes is captured without the need to switch models, particularly in the case of stress-driven systems. Previously, the kinetic equation has also been combined with an advanced model of the dislocation drag coefficient, which can impact the prediction of the flow stress at high strain rates (Blaschke, Hunter, and Preston, 2020a; Blaschke, Mottola, and Preston, 2020b).

Thus, by averaging over configurations, properly accounting for the effects of thermal fluctuations on the short-distance interactions, and accounting for a host of well-known dislocation maneuvers responsible for storage, dynamic recovery, and dislocation multiplication, it is possible to construct a reliable, practical analytic dislocation dynamics based model of the flow stress (strength) as a function of strain, strain rate, temperature, and material density. Such a model will be developed as a combination of the dislocation density evolution equations developed here, and the previously developed kinetic equation. We will present results of the complete model in comparison to experimental data for copper, which spans a wide range of strain rates and temperatures.

In Section 2 we derive the rates of mobile dislocation storage in the network of immobile dislocation and on grain boundaries. The next section concerns mobile-immobile and mobile-mobile annihilation rates during dislocation glide, as well as the rate at which screw-screw annihilation occurs as a result of single cross-slip, which can be either athermal or thermally activated. Our activation energy for single cross-slip is a modification of the well-known Friedel-Escaig result. Dislocation multiplication rates are calculated in Section 4. The model incorporates four dislocation generation mechanisms: FR sources, the Koehler mechanism for single-loop and edge-dipole formation, grain boundary nucleation of dislocation, and shock wave generation. Since the Koehler process involves double cross-slip, we derive the activation energy for double cross-slip. In Section 5 the results of the previous three sections are assembled into the dislocation density evolution equations. Our model for copper, including extensive comparisons to data, are presented in the next section. Finally, in Section 7 we summarize our findings. The effect of mass density variations on the mobile and immobile dislocation densities is described in Appendix A, and results on structure evolution at room temperature and constant plastic strain rate are provided in Appendix D.

2 Storage in the Network and Grain Boundaries

Storage of mobile dislocation in the network during stage II of the stress-strain curve occurs primarily through junction-forming interactions. Kubin, Devincre, and Hoc have carried out a thorough

study of storage mechanisms in *fcc* single crystals (Kubin, Devincere, and Hoc, 2008). They considered the dislocation intersections and reactions responsible for junction formation, the primary storage mechanism during stage II of the stress-strain curve, as well as the self-interactions and coplanar interactions that are important during stage I. They find that all of these contributions to the storage rate vary as the square root of the forest (immobile) dislocation density. Therefore, in the present model, storage in the network is represented by the following contributions to the evolution equations

$$\frac{d\rho_i^{sn}}{dt} = -\frac{d\rho_m^{sn}}{dt} = g_{sn} \frac{1}{b} \sqrt{\rho_i} \dot{\epsilon}. \quad (3)$$

where g_{sn} is a dimensionless proportionality constant. Our fits to stress-strain data shown in Section 6 yield $g_{sn} = 0.05$.

Mobile dislocation can also be stored along the grain boundaries, thus increasing the population of immobile dislocation. To obtain an expression for the storage rate of mobile dislocations in the grain boundaries, the mobile population is idealized as a simple cubic lattice of equal-length screw dislocation segments with orientations (and Burgers vectors) distributed with equal probability in the x , $-x$, y , or $-y$ directions; the glide direction is along z . The unit cell size is $\mathcal{L}_m = 1/\sqrt{\rho_m}$. The unit vector \hat{z} is taken to be the outward unit normal to a face of the grain, which is assumed to be a cube of volume V . Within the grain there are V/\mathcal{L}_m^3 segments, each of length \mathcal{L}_{seg} , for a total length of $V\mathcal{L}_{seg}/\mathcal{L}_m^3$, but this must equal $V\rho_m = V/\mathcal{L}_m^2$, hence $\mathcal{L}_{seg} = \mathcal{L}_m$. Thus, a single screw segment of length \mathcal{L}_m is attached to each node of the lattice with its Burgers vector in the x , $-x$, y , or $-y$ direction with equal probability. These segments move at velocity, v , along \hat{z} . When a segment encounters the face it is stored with probability p_s . In time dt the total length of mobile dislocation stored is

$$dl_m^s = p_s \cdot \frac{V^{2/3}}{\mathcal{L}_m^2} \cdot \frac{v dt}{\mathcal{L}_m} \cdot \mathcal{L}_m, \quad (4)$$

where v is the mean dislocation velocity. It follows from Equation (4) that the rate of change of the mobile and immobile dislocation densities due to storage on the grain boundaries is

$$\frac{d\rho_i^{s\partial}}{dt} = -\frac{d\rho_m^{s\partial}}{dt} = \frac{dl_m^s}{V dt} = \frac{p_s}{V^{1/3}} \rho_m v = p_s \frac{\dot{\epsilon}}{b V^{1/3}}. \quad (5)$$

While this result establishes the correct dependence of the storage rate on the grain volume and strain rate, our idealized system does not account for the *fcc* lattice structure, statistical variations in dislocation orientations and Burgers vectors, correlation effects, and dislocation line continuity. For a real *fcc* polycrystal, V should be replaced by $\pi D^3/6$, where D is the average grain size (diameter), and the resulting numerical coefficient, $(6/\pi)^{1/3} p_s$, must be generalized to a dimensionless coefficient $g_{s\partial}$

$$\frac{d\rho_i^{s\partial}}{dt} = -\frac{d\rho_m^{s\partial}}{dt} = g_{s\partial} \frac{\dot{\epsilon}}{b D}. \quad (6)$$

3 Dynamic Recovery

3.1 Mobile-Network and Mobile-Mobile Annihilation

To obtain an expression for the rate of mobile-immobile annihilation reactions, we once again consider the idealized mobile dislocation network described above in Section 2, but in addition the immobile dislocation is idealized as a simple cubic lattice of equal-length screw dislocation segments.

The unit cell size is $\mathcal{L}_i = 1/\sqrt{\rho_i}$, and the segments are of length \mathcal{L}_i . The Burgers vectors of the immobile screw segments, one per lattice site, are distributed randomly in the x, y, and z directions. Consider now a glide plane within the lattice coincident with an $x-z$ or $y-z$ plane in the network lattice, a strip of width $dz \gg \mathcal{L}_i$ lying in the glide plane, and a mobile screw segment gliding toward the strip. The number of immobile segments per unit area parallel to the mobile segment (one out of three) but having the opposite Burgers vector (probability 1/2) is $(1/3)(1/2)(1/\mathcal{L}_i^2) = 1/(6\mathcal{L}_i^2)$. When the mobile segment glides through the strip the length of mobile or immobile dislocation annihilated is $1/(6\mathcal{L}_i^2) \cdot \mathcal{L}_m dz \cdot \mathcal{L}_i = \mathcal{L}_m dz / 6\mathcal{L}_i$, and the corresponding rate of loss of dislocation is $\mathcal{L}_m v / 6\mathcal{L}_i$. Since the number of mobile dislocation segments per unit volume is \mathcal{L}_m^{-3} , the total rate of loss of mobile dislocation density, which equals the rate of loss of immobile density, is

$$\frac{d\rho_m^{mi}}{dt} = \frac{d\rho_i^{mi}}{dt} = -\frac{v}{6\mathcal{L}_m^2 \mathcal{L}_i} = -\frac{1}{6b} \sqrt{\rho_i} \dot{\epsilon}. \quad (7)$$

The coefficient 1/6, which is specific to our idealized system, must be generalized to a dimensionless coefficient, g_{ami} , for real materials:

$$\frac{d\rho_m^{mi}}{dt} = \frac{d\rho_i^{mi}}{dt} = -g_{ami} \frac{1}{b} \sqrt{\rho_i} \dot{\epsilon}. \quad (8)$$

Since 1/6 is of order 0.1, and allowing for deviations of one order of magnitude from this value for real materials, it is expected that $g_{ami} \sim 0.01 - 1$. We obtain $g_{ami} = 0.01$ from fits to stress-strain data; see Section 6.

Because of variations in the glide velocities of mobile segments, mobile dislocations can approach one another and undergo annihilation reactions. The rate is of the same form as Equation (8)

$$\frac{d\rho_m^{mm}}{dt} = -g_{amm} \frac{1}{b} \sqrt{\rho_m} \dot{\epsilon}. \quad (9)$$

3.2 Single Cross-Slip and Screw-Screw Annihilation

The only known mechanism for the annihilation of dislocations on different glide planes is single cross-slip of a screw dislocation followed by its annihilation with a screw of opposite sign (Burgers vectors are the negatives of one another) residing on either the cross-slip plane or on a slip plane parallel to the primary (initial) glide plane. If the screws are within a critical distance of each other then the annihilation takes place spontaneously, that is, athermally; this case is discussed in detail in Section 3.2.5. Here we consider only thermally-activated cross-slip. Several models have been proposed to describe the cross-slip process, including the models of Fleischer (1959), Washburn (1965), Schoeck and Seeger (1955), and Wolf (1960), and the Friedel-Escaig model (Friedel, 1957; Escaig, 1968). In general, both experimental and simulation results support, at least qualitatively, the Friedel-Escaig mechanism, which is shown schematically in Figure 1.

The essential idea underlying this mechanism is that an extended screw dislocation gliding along a close-packed plane in a *fcc* lattice contracts along a short section of length L_x into a perfect screw segment which easily cross-slips onto another close-packed plane; it then extends to a maximum width d_i ($i \sim$ interior to constrictions) on the cross slip plane. The *equilibrium* extended dislocation widths in the primary and cross-slip planes are denoted, respectively, by d_p and d_x . The fault width is determined by both the stacking fault energy and the shear stress in the plane of the stacking fault; hence, $d_p \neq d_x$ because the resolved shear stresses on the primary and cross-slip planes differ.

The activation energy is the sum of the constriction energy, i.e., the total energy of the constrictions on the primary and cross-slip planes, and the dissociation energy, which is the change in

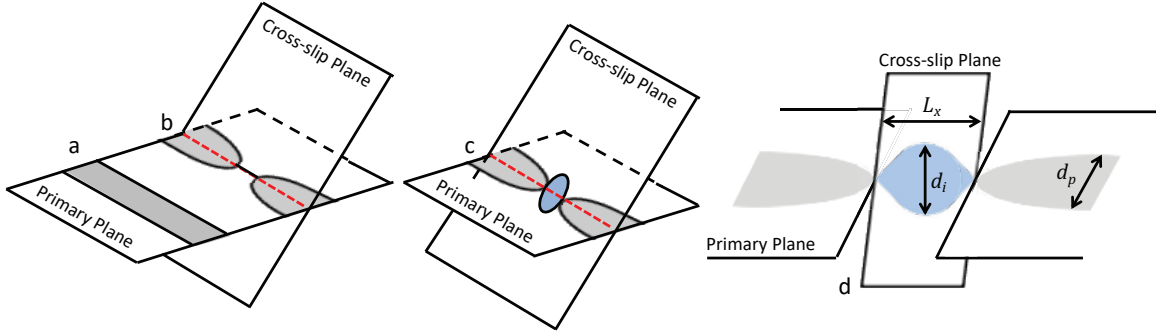


Figure 1: Friedel-Escaig cross-slip mechanism. The left-most figure shows a leading and trailing partial dislocation bounding a stacking fault region (gray region) gliding on the primary plane (a). Once the partial dislocations reach the cross-slip plane they constrict to form a perfect screw dislocation (b). The center figure shows the leading and trailing partial dislocations once again expanding, creating a stacking fault region (blue region) but now on the cross-slip plane (c). The right-most figure shows a more detailed view of the partial dislocations expanding on the cross-slip plane (d).

the elastic and fault energies from contraction to a perfect screw of length L_x followed by extension on the cross-slip plane. The constriction (dissociation) energy is calculated in Section 3.2.2 (3.2.3). Before calculating the constriction and dissociation energies we derive approximate expressions for the stress-dependent intrinsic stacking fault widths on the primary and cross-slip planes.

3.2.1 Fault Widths on the Primary and Cross-Slip Planes

Perfect dislocations in the *fcc* lattice have Burgers vectors of type $\mathbf{b} = (1/2) \langle 110 \rangle$, but dislocations in the *fcc* lattice are not perfect – they dissociate into Shockley partial dislocations with Burgers vectors that can be determined by reference to the Thompson tetrahedron. Without loss of generality and using the Thompson tetrahedron notation, we consider the following specific example: a dissociated screw with Burgers vector $\mathbf{b} = (1/2) [\bar{1} 0 1]$ and unit line sense vector $\hat{\xi} = (1/\sqrt{2}) [\bar{1} 0 1]$. This dislocation is dissociated into partials, $\mathbf{b} \rightarrow \mathbf{b}_1 + \mathbf{b}_2$, on the primary, $d = (111)$, glide plane, where $\mathbf{b}_1 = (1/6) [\bar{1} \bar{1} 2]$ and $\mathbf{b}_2 = (1/6) [\bar{2} 1 1]$. In $x - y$ coordinates with the partials parallel to the x -axis and located at $\pm y$, the repulsive force per unit length between them is given by Anderson, Hirth, and Lothe (2017),

$$F(y) = \frac{G}{4\pi y} \left\{ (\mathbf{b}_1 \cdot \hat{\xi}) (\mathbf{b}_2 \cdot \hat{\xi}) + \frac{1}{1-\nu} \mathbf{b}_1 \times \hat{\xi} \cdot \mathbf{b}_2 \times \hat{\xi} \right\}, \quad (10)$$

where G is the shear modulus and ν is Poisson's ratio. With $\nu = 1/3$, assumed henceforth, and $b = \sqrt{3}b_{1,2}$, the force can be written

$$\begin{aligned} F(y) &= \frac{\mathcal{A}}{2y}, \\ \mathcal{A} &= \frac{Gb^2}{16\pi}. \end{aligned} \quad (11)$$

Although $F(y)$ is strictly correct only for straight dislocations, the constriction angle $\tan^{-1}(dy/dx)$ is small (as will be shown later in this subsection), so use of Equation (11) incurs a negligible error.

We next consider cross-slip of the screw dislocation considered in the previous paragraph from the $d = (111)$ glide plane of the fcc lattice to the $a = (\bar{1}1\bar{1})$ plane. The Burgers vector of the leading (trailing) partial dislocation during glide is \mathbf{b}_1 (\mathbf{b}_2); on $d = (111)$, $\mathbf{b}_1 = (1/6) [\bar{1}\bar{1}2]$ and $\mathbf{b}_2 = (1/6) [\bar{2}11]$, while on $a = (\bar{1}1\bar{1})$, $\mathbf{b}_1 = (1/6) [\bar{2}\bar{1}1]$ and $\mathbf{b}_2 = (1/6) [\bar{1}12]$. The stacking fault is taken to lie in the $x - y$ ($x' - y'$) plane on the primary (cross-slip) plane with $\hat{\xi} = \hat{\mathbf{x}}$. The Burgers vectors are of the form $\mathbf{b}_i = b_i (\cos \theta \hat{x} + \sin \theta \hat{y})$ with $|\theta| = \pi/6$; θ is negative (positive) for the leading partial on the d (a) glide plane, and of the opposite sign for the trailing partial. Determination of the fault widths on the d and a planes requires the force per unit length on each of the partials; on the d -plane

$$\mathbf{F}^{(i)} = b_i (\cos \theta_i \sigma_{xz} + \sin \theta_i \sigma_{yz}) \hat{\mathbf{y}}, \quad (12)$$

with a similar expression for the a -plane. Since θ_1 and θ_2 are of opposite sign, the first term is the glide force on the extended dislocation, while the second term induces constriction or widening of the stacking fault. The fault width of an isolated screw dislocation in an external stress field is determined by requiring that the sum of the constriction/widening force, the repulsive partial-partial interaction, and the attractive fault force sum to zero. On the primary plane

$$-\frac{1}{2} b_i \sigma_{yz} + \frac{\mathcal{A}}{d_p} - \gamma = 0. \quad (13)$$

Solving for the fault width and using $b_i = b/\sqrt{3}$ gives

$$d_p = \frac{\mathcal{A}}{\gamma + b \sigma_{yz}/2\sqrt{3}} \equiv \frac{\mathcal{A}}{\gamma^{(p)}}. \quad (14)$$

On the cross-slip plane the sign of the first term in Equation (13) is reversed, therefore

$$d_x = \frac{\mathcal{A}}{\gamma - b \sigma_{y'z'}/2\sqrt{3}} \equiv \frac{\mathcal{A}}{\gamma^{(x)}}. \quad (15)$$

A cursory reference to Equations (14) and (15) would suggest that the fault is contracted (expanded) on the primary plane and expanded (contracted) on the cross-slip plane relative to the stress-free width. A simple analysis shows that this is not true in general. Transforming the components of the stress tensor from $x - y - z$ to $x' - y' - z'$ coordinates shows that

$$\sigma_{y'z'} = (1/9) \left[2\sqrt{2}(\sigma_{zz} - \sigma_{yy}) - 7\sigma_{yz} \right]. \quad (16)$$

If $\sigma_{yy} = \sigma_{zz}$ then $\sigma_{y'z'} = (-7/9) \sigma_{yz}$, so the fault is contracted ($\sigma_{yz} > 0$) or expanded ($\sigma_{yz} < 0$) on both planes, and the fault widths are approximately equal. In the following we assume that $\sigma_{yz} > 0$ and $\sigma_{y'z'} < 0$ since the fault widths would diverge for sufficiently large shear stresses of the opposite sign, an aspect of the dynamics that we do not take into account.

The goal of the present work is a practical J_2 model of plastic flow – the stress deviators appear only through their second-order rotational invariant, i.e. the flow stress. Consequently, the resolved shear stresses are taken to be proportional to the effective flow stress: $\sigma_{yz} \propto \hat{\sigma}$ and $-\sigma_{y'z'} \propto \hat{\sigma}$. Proportionality constants are introduced that absorb the factor $2\sqrt{3}$ in Equations (14) and (15); the stress-dependent fault energies are written

$$\gamma^{(p)} = \gamma + \alpha_p b \hat{\sigma}, \quad \gamma^{(x)} = \gamma + \alpha_x b \hat{\sigma}. \quad (17)$$

The proportionality constants, α_p and α_x , are expected to be of order 1/10.

At zero effective stress, $\hat{\sigma} = 0$, we have $d_p = d_x = d_0 = \mathcal{A}/\gamma$. If we assume that d_0 scales with the interatomic distance, i.e., $d_0(\rho) = d_0(\rho_0) (\rho_0/\rho)^{1/3}$, it follows that

$$\gamma(\rho) = \gamma(\rho_0) \frac{G_0(\rho)}{G_0(\rho_0)} \left(\frac{\rho_0}{\rho} \right)^{1/3}, \quad (18)$$

where G_0 is the $T = 0$ shear modulus (thermal softening of G is neglected); see Equation (219). For the back stress given by $\sigma_b = g_b b G \sqrt{\rho_i}$ (Hunter and Preston, 2015), and assuming shear modulus scaling of the flow stress (valid at stresses below the viscous drag regime), it follows that $\hat{\sigma}$ scales with the shear modulus. Equations (213) and (18) then imply

$$\gamma^{(p,x)}(\rho) = \gamma^{(p,x)}(\rho_0) \frac{G_0(\rho)}{G_0(\rho_0)} \left(\frac{\rho_0}{\rho} \right)^{1/3}, \quad (19)$$

Since $\mathcal{A} \sim G_0(\rho) \rho^{-2/3}$ it follows that $d_{p,x} \sim \rho^{-1/3}$, as expected.

Since the effective fault energies $\gamma^{(p,x)}$ increase linearly with $\hat{\sigma}$, the fault widths decrease as $\hat{\sigma}^{-1}$ at high stresses (strain rates); the fault width has decreased to b for $\hat{\sigma}/G = (16\pi\alpha_{p,x})^{-1} \sim 0.2$. Continuum theory breaks down at distances of order b . We accordingly take b to be our short-distance cutoff thus making b our minimum fault width and modify our above results for the stress-dependent stacking fault widths so that they asymptote to b as $\hat{\sigma} \rightarrow \infty$:

$$d_{p,x}(\hat{\sigma}) = \frac{\mathcal{A} + \alpha_{p,x} b^2 \hat{\sigma}}{\gamma + \alpha_{p,x} b \hat{\sigma}} = \frac{\mathcal{A}}{\Gamma^{(p,x)}}, \quad (20)$$

where

$$\Gamma^{(p,x)} = (1 + 16\pi\alpha_{p,x} \hat{\sigma}/G)^{-1} (\gamma + \alpha_{p,x} b \hat{\sigma}). \quad (21)$$

The additional term in the numerator of Equation (20), namely $\alpha_{p,x} b^2 \hat{\sigma}$, is significant only at very high strain rates, generally 10^6 s^{-1} and higher. Note that $d_{p,x}$ as given by Equation (20) scales with density as $\rho^{-1/3}$, as required. At large strain rates ($\gtrsim 10^6 \text{ s}^{-1}$) $d_{p,x}/b \rightarrow 1$, and consequently the activation energies will go to zero. This is apparent in figures of the activation energy evolution (e.g., Figures 2 and 4). We highlight that as the Arrhenius exponentials approach unity, the rate of dislocation annihilation by single cross-slip and generation by double cross-slip are no longer suppressed. Both of these terms in the dislocation density evolution equations are proportional to $\bar{\nu}/\dot{\epsilon}$, but the double cross-slip term is the larger of the two. Thus, our model predicts that the overall generation of dislocation at rates $\gtrsim 10^{10}/\text{s}$ is predominantly due to double cross-slip. While it is likely that the activation energies do decrease at rates $\gtrsim 10^6/\text{s}$, the drop to zero is due to a breakdown of continuum theory at these very high strain rates (i.e., it predicts that the stacking fault widths decrease to b). Hence, at very large strain rates ($\gtrsim 10^{10}/\text{s}$) the dominate effect of double cross-slip may not be entirely accurate, and this is reaching the strain rate limits of the model's applicability. Molecular dynamics simulations could be employed to develop improved sub-models for the activation energies at strain rates above $10^6/\text{s}$.

3.2.2 Constriction Energy

The constriction energy clearly depends on the shapes of the Shockley partial dislocations around the constriction, so we begin with the derivation of a differential equation for the shapes of the partials. During single cross-slip and assuming the Friedel-Escaig mechanism, two four-partial constrictions are formed, one at each end of the segment that cross-slip (see Figure 1(d)). Each of these four partial constrictions is a pair of exterior (on the primary plane) and interior (on the

cross-slip plane) two-partial constrictions. The fault widths on the primary and cross-slip planes, d_p and d_x , differ from each other because of the difference in the resolved shear stresses. The corresponding stress-dependent fault energies are given by $\Gamma^{(p)} = \mathcal{A}/d_p$ and $\Gamma^{(x)} = \mathcal{A}/d_x$; see Equations (20) and (21). The widths of the exterior faults on the primary plane asymptote to d_p , and the maximum width of the interior fault on the cross-slip plane is $d_i < d_x$; see Figure 1. The fault energy per unit length around a constriction on the primary or cross-slip plane is $\Gamma^{(p,x)} |y(x)|$, and the attractive force per unit length due to the fault is $-\partial_y (\Gamma^{(p,x)} |y|) = -\text{sign}(y) \Gamma^{(p,x)}$.

As in the well-known derivation of the wave equation for a string under tension, $\mathcal{T} y''$ is the restoring force per unit length on the dislocation in the line tension approximation. The restoring force describes the force needed to bend the straight dislocation lines, including the force required to lengthen the dislocations as the lines curve. There are two cases to consider: the exterior two-partial constriction on the primary (p) glide plane and the interior (i) two-partial constriction on the cross-slip plane. The line tension of each partial around the constrictions is approximately (Caillard and Martin, 2003; Escaig, 1968)

$$\mathcal{T}_{p,i} = \frac{G b_{1,2}^2}{4\pi} \ln \left(\frac{d_{p,i}}{b_{1,2}} \right) = \frac{4}{3} \mathcal{A} \ln \left(\frac{\sqrt{3} d_{p,i}}{b} \right). \quad (22)$$

Equilibrium requires that the sum of the restoring force, the partial-partial repulsion, and the fault-induced attraction sum to zero

$$\mathcal{T}_{p,i} \frac{d^2 y}{dx^2} + \frac{\mathcal{A}}{2y} - \Gamma^{(p,x)} = 0. \quad (23)$$

Note that $d^2 y/dx^2 < 0$ ($d^2 y/dx^2 > 0$) for $y > 0$ ($y < 0$). Integrating Equation (23) with respect to y gives

$$\left(\frac{dy}{dx} \right)^2 = \mathcal{T}_{p,i}^{-1} \left(-\mathcal{A} \ln y + 2\Gamma^{(p,x)} y + c \right), \quad (24)$$

where c is an integration constant. For the exterior constriction we require $y \rightarrow d_p/2$ as $x \rightarrow \infty$; using $\Gamma^{(p)} = \mathcal{A}/d_p$ this gives $c = \mathcal{A} [\ln(d_p/2) - 1]$. With the definition

$$\chi(t) = \ln(1/t) + t - 1, \quad (25)$$

the solution to our equilibrium ODE for an exterior constriction at the origin and $x, y > 0$ can be expressed

$$x(y) = \frac{d_p}{2} \left(\frac{\mathcal{T}_p}{\mathcal{A}} \right)^{1/2} \int_0^{2y/d_p} \chi^{-1/2}(t) dt. \quad (26)$$

For an interior constriction we require $y \rightarrow d_i/2$ as $x \rightarrow \infty$; using $\Gamma^{(x)} = \mathcal{A}/d_x$ this gives $c = \mathcal{A} [\ln(d_i/2) - d_i/d_x]$ and

$$x(y) = \frac{d_i}{2} \left(\frac{\mathcal{T}_i}{\mathcal{A}} \right)^{1/2} \int_0^{2y/d_i} \chi_i^{-1/2}(t) dt, \quad (27)$$

where

$$\chi_i(t, d_i/d_x) = \chi(t) + \left(1 - \frac{d_i}{d_x} \right) (1 - t). \quad (28)$$

The cross slip length L_x (see Figure 1) is given by

$$\begin{aligned} L_x &= 2 \int_0^{d_i/2} \frac{dx}{dy} \Big|_x dy = \left(\frac{\mathcal{T}_i}{\mathcal{A}} \right)^{1/2} d_i \int_0^1 dt \chi_i^{-1/2}(t, d_i/d_x) \\ &\approx \left(\frac{\mathcal{T}_i}{\mathcal{A}} \right)^{1/2} d_x \Lambda \left(\frac{d_i}{d_x} \right), \end{aligned} \quad (29)$$

where

$$\Lambda(z) = z \int_0^1 dt \{\chi(t) + (1-z)(1-t)\}^{-1/2} \approx \frac{8}{5} \ln \left(\frac{1}{1-z} \right). \quad (30)$$

This approximation is very good. The fault width on the cross-slip plane can be expressed in terms of the cross-slip length using $\Lambda^{-1}(z)$

$$\frac{d_i}{d_x} = \Lambda^{-1} \left(\sqrt{\frac{\mathcal{A}}{\mathcal{T}_i} \frac{L_x}{d_x}} \right) = 1 - \exp \left(-\frac{5}{8} \sqrt{\frac{\mathcal{A}}{\mathcal{T}_i} \frac{L_x}{d_x}} \right). \quad (31)$$

Atomistic simulations by Rasmussen, Vegge, Leffers, Pedersen, and Jacobsen (2000) indicate that the cross-slip length is of order the stacking fault width before cross-slip. Moreover, explicit calculation shows that the cross-slip energy is insensitive to the value of L_x . In view of these points, in this model the cross-slip length L_x will be set equal to d_p , the fault width before cross-slip.

We now evaluate the three contributions to the constriction energy, namely, the positive elastic partial-partial interaction energy, the decrease in the fault energy, and the increase in the self energies of the partials. Since there will always be pairs of interior or exterior two-partial constrictions during cross-slip, the constriction energies will always be for symmetric, four-partial constrictions.

To form a constriction, work must be done against the repulsive interaction between the partial dislocations. This elastic energy per unit length at fixed x is

$$2 \int_{d/2}^y -F(y') dy' = \mathcal{A} \int_y^{d/2} \frac{dy'}{y'} = \mathcal{A} \ln \left(\frac{d}{2y} \right) \quad (32)$$

where $d = d_p$ or d_i . The elastic energy of the four-partial constriction is then obtained by integrating over all x

$$E_e = \mathcal{A} \int_{-\infty}^{\infty} \ln \left[\frac{d}{2y(x)} \right] dx. \quad (33)$$

The decrease in the stacking fault energy is obviously

$$E_\gamma = -\gamma \int_{-\infty}^{\infty} [d - 2y(x)] dx. \quad (34)$$

The sum of the elastic and stacking fault energies assumes a very compact form for both interior and exterior constrictions

$$E_e + E_\gamma = \mathcal{T} \int_{-\infty}^{\infty} \left(\frac{dy}{dx} \right)^2 dx, \quad (35)$$

where $\mathcal{T} = \mathcal{T}_p$ or \mathcal{T}_i .

Before proceeding with the evaluation of the self energies of the partials during constriction, we first show that the bow-out angles of the partials around the constriction are small. A half-partial dislocation in the first quadrant is approximated as the sum of a line segment from the origin to the point $(l_c, d/2)$, where l_c is the half-width of the constriction, and the semi-infinite line parallel to the x -axis with endpoint $(l_c, d/2)$; here $d = d_p$ (d_i) for an exterior (interior) constriction. The constriction half-width is fixed by demanding that the area under the actual partial between the origin and l_c equals the area under the segment

$$\int_0^{l_c} y(x) dx = l_c y_c - \int_0^{y_c} x(y) dy = \frac{1}{2} l_c \frac{d}{2}, \quad (36)$$

where $y_c = y(l_c)$. The constriction half-width as a function of y_c is provided by Equations (26) and (27) for exterior and interior constrictions, respectively. For an exterior (primary plane) constriction

$$l_c = x(y_c) = \frac{d_p}{2} \left(\frac{\mathcal{T}_p}{\mathcal{A}} \right)^{1/2} \int_0^{2y_c/d_p} \chi^{-1/2}(t) dt. \quad (37)$$

Substituting this expression for l_c in Equation (36) results in a transcendental equation for y_c

$$\int_0^{2y_c/d_p} dt \left\{ \left(\frac{2y_c}{d_p} - \frac{1}{2} \right) \chi^{-1/2}(t) - \int_0^t dt' \chi^{-1/2}(t') \right\} = 0. \quad (38)$$

Its numerical solution is

$$\frac{2y_c}{d_p} = 0.7563. \quad (39)$$

The constriction angle, ϕ_p , is given by

$$\tan \phi_p = \frac{d_p}{2l_c} = \left(\frac{\mathcal{A}}{\mathcal{T}_p} \right)^{1/2} \left\{ \int_0^{2y_c/d_p} \chi^{-1/2}(t) dt \right\}^{-1} = 0.65 \left(\frac{\mathcal{A}}{\mathcal{T}_p} \right)^{1/2} = 0.56 \ln^{-1/2} \left(\sqrt{3} \frac{d_p}{b} \right), \quad (40)$$

where the last equality follows from Equation (22). The physically relevant range of values of d_p/b is approximately 1 - 10 based on estimates and measured values for Al, Pd, Au, Ni, Cu, and Ag (Hunter, Zhang, Beyerlein, Germann, and Koslowski, 2013). The exterior constriction angle varies from 18° at $d_p/b = 10$ to 32° at $d_p/b = 1$ (high stresses) with an average value of 22° . The bow-out on the primary plane is in fact a small-angle.

For an interior constriction, substitution of $l_c = x(y_c)$ from Equation (27) into Equation (36) yields an equation of the same form as Equation (38) but with $\chi(t) \rightarrow \chi_i(t, d_i/d_x)$. It was solved numerically for $2y_c/d_i$ as a function of $d_i/d_x < 1$ (It follows from both physical reasoning and Equation (31) that $d_i < d_x$.) The interior constriction angle is approximately given by

$$\begin{aligned} \tan \phi_i &= \frac{d_i}{2l_c} = \left(\frac{\mathcal{A}}{\mathcal{T}_i} \right)^{1/2} \left(1.07 - 0.38 \frac{d_i}{d_x} \right) \\ &= \ln^{-1/2} \left(\sqrt{3} \frac{d_i}{b} \right) \left(0.93 - 0.33 \frac{d_i}{d_x} \right). \end{aligned} \quad (41)$$

In order to estimate the range of values of ϕ_i we next obtain an approximation for d_i/d_x . Equation (31) with $L_x \rightarrow d_p$ depends on the ratio d_p/d_x . As noted after Equation (16) the fault widths d_p and d_x are approximately equal, hence we set $L_x = d_p \approx d_x$ in Equation (31) and then use Equation (22) to give

$$\frac{d_i}{d_x} = 1 - \exp \left(-\frac{5\sqrt{3}}{16} \ln^{-1/2} \left(\sqrt{3} \frac{d_i}{b} \right) \right). \quad (42)$$

A plot of d_i/b as a function of $d_x/b \in [1, 10]$ reveals a nearly linear relation. The optimal linear fit subject to the constraint that $d_i \rightarrow b$ as $d_x \rightarrow b$ is simply

$$d_i = (d_x + 3b)/4. \quad (43)$$

Substitution into Equation (41) gives $\tan \phi_i$ for interior constrictions as a function of d_x/b . We find that ϕ_i varies from 32° at $d_x/b = 10$ to about 40° at $d_x/b = 1$ with an average value of 36° . Although larger than the corresponding values for an exterior constriction, these angles are small enough to consider the bow-out as small.

The changes in the self energies of the partials during constriction will now be estimated in the piecewise-linear approximation that was used to estimate the bow-out angles. The self energies of straight segments of length l of the partials (Burgers vectors $b_{1,2}$) comprising an extended screw dislocation (Burgers vector $b = \sqrt{3}b_{1,2}$) are

$$W_s = S l \ln \left(\frac{l}{b_{1,2}} \right), \quad (44)$$

where (for $\nu = 1/3$)

$$S = \frac{G}{4\pi} \left\{ (\mathbf{b}_{1,2} \cdot \hat{\xi})^2 + \frac{1}{1-\nu} |\mathbf{b}_{1,2} \times \hat{\xi}|^2 \right\} \approx \frac{4}{3} \mathcal{A}. \quad (45)$$

During small-bow-out constriction the change in length of the partials is

$$\Delta l = l_c \left(\frac{1}{\cos \phi} - 1 \right) \approx \frac{l_c}{2} \tan^2 \phi. \quad (46)$$

The corresponding change in the self energy of a partial is

$$\Delta W_s = \frac{4}{3} \mathcal{A} \left[1 + \ln \left(\frac{l_c}{b_{1,2}} \right) \right] \Delta l = \frac{2}{3} \mathcal{A} l_c \left[1 + \ln \left(\frac{\sqrt{3} l_c}{b} \right) \right] \tan^2 \phi. \quad (47)$$

Finally, the self energy change of the four partials of a constriction may be written ($l_c = d/\tan \phi$)

$$E_s = \frac{4}{3} \mathcal{A} \left[1 + \ln \left(\frac{\sqrt{3} d}{2 b \tan \phi} \right) \right] d \tan \phi, \quad (48)$$

where $d = d_p$ or d_i and $\phi = \phi_p$ or ϕ_i .

In this piecewise-linear approximation the sum of the elastic interaction and stacking fault energies (see Equation (35)) is

$$E_e + E_\gamma = \mathcal{T} \int_{-\infty}^{\infty} \left(\frac{dy}{dx} \right)^2 dx = 2\mathcal{T} \int_0^{d/2} \frac{dy}{dx} dy \approx \mathcal{T} d \tan \phi. \quad (49)$$

For an exterior constriction with $\tan \phi$ given by Equation (40), Equation (49) gives $E_e + E_\gamma = 0.65 (\mathcal{A} \mathcal{T}_p)^{1/2} d_p$, whereas integrating dy/dx gives $E_e + E_\gamma = 0.55 (\mathcal{A} \mathcal{T}_p)^{1/2} d_p$.

The constriction energy is the sum $E_s + E_e + E_\gamma$:

$$E^{(c)} = \mathcal{A} b \left\{ \frac{\mathcal{T}}{\mathcal{A}} + 1 + \frac{4}{3} \ln \left(\frac{\sqrt{3} d}{2 b \tan \phi} \right) \right\} \frac{d}{b} \tan \phi. \quad (50)$$

For an exterior constriction with $\tan \phi$ given by Equation (40) the constriction energy is

$$E_p^{(c)} = \frac{0.75 \mathcal{A} b}{\ln^{1/2}(\sqrt{3} x)} \left\{ \ln(\sqrt{3} x) + 0.75 + \ln \left[\frac{x \ln^{1/2}(\sqrt{3} x)}{0.65} \right] \right\} x, \quad (51)$$

where $x = d_p/b$. This is well approximated by

$$E_p^{(c)} = 3.4 \mathcal{A} b \left(\frac{d_p}{b} - 1 \right). \quad (52)$$

Similarly, the energy of an interior constriction on the cross-slip plane is approximately

$$E_i^{(c)} = 1.3 \mathcal{A} b \left(\frac{d_x}{b} - 1 \right). \quad (53)$$

3.2.3 Single Cross-Slip Dissociation Energy

The change in elastic and fault energies as a result of contraction to a perfect screw of length L_x between the constriction points and the subsequent extension on the cross-slip plane is often referred to as the dissociation energy E_d . The elastic energy increase due to contraction on the primary plane to a perfect screw segment is $L_x \mathcal{A} \ln(d_p/2y_0)$, where y_0 cuts off the divergent short distance interaction. Expansion on the cross-slip plane then reduces the elastic energy by $L_x \mathcal{A} \ln(d_i/2y_0)$, thus the net change in the elastic energy is $L_x \mathcal{A} \ln(d_p/d_i)$. The initial collapse of the stacking fault decreases the fault energy by $L_x d_p \gamma^{(p)} = L_x \mathcal{A}$, but extension on the cross-slip plane increases it by $L_x d_i \gamma^{(x)} = L_x (d_i/d_x) \mathcal{A}$, giving a net change of $L_x \mathcal{A} (d_i/d_x - 1)$. The dissociation energy is given by

$$E^{(d)} = L_x \mathcal{A} \left[\ln \left(\frac{d_p}{d_i} \right) + \frac{d_i}{d_x} - 1 \right], \quad (54)$$

where $L_x = d_p$ was used. Equation (43) and the approximation $d_p \approx d_x = d$ gives

$$E^{(d)} \approx \mathcal{A} b \left[x \ln \left(\frac{4x}{x+3} \right) + \frac{3}{4} (1-x) \right] \approx 0.45 \mathcal{A} b (x-1), \quad (55)$$

where $x = d/b$. This is a rough approximation but acceptable since the constriction energy is an order of magnitude larger.

3.2.4 Single Cross-Slip Activation Energy

The net effect of cross-slip is the formation of: (1) external constrictions on the primary glide plane with a total energy $E_p^{(c)}$; (2) internal constrictions on the cross-slip plane with a total energy $E_i^{(c)}$; and (3) the dissociation energy $E^{(d)}$. The total energy change accompanying cross-slip is the sum of the constriction and dissociation energies, that is, the sum of Equations (52), (53) and (55). In the approximation $d_p \approx d_x = d$ ($\alpha_p \approx \alpha_x = \alpha$) the single cross-slip activation energy is

$$E_x = 5.15 \mathcal{A} b \left(\frac{d}{b} - 1 \right) = \frac{5.15 \mathcal{A} b}{1 + \alpha b \hat{\sigma} / \gamma} \left(\frac{d_0}{b} - 1 \right); \quad (56)$$

d_0 is the density-dependent (shear) stress-free fault width. For copper at nominal density and 300K, $G = 48$ GPa (Simmons and Wang, 1971), $\mathcal{A} b \approx 0.1$ eV, and for $\gamma = 50$ mJ m⁻² (see Section 6) and $\hat{\sigma} = 0$ we get $d_0/b = \mathcal{A}/b\gamma = 4.93$. Substitution into Equation (56) gives a stress-free activation energy of 2 eV. By way of comparison, Rasmussen et al. (2000) concluded that ‘‘Cross-slip is a thermally activated process with a stress-free activation energy of 2.7 eV’’. The activation energy of copper is plotted in Figure 2 as a function of strain rate and temperature. We note that the values shown in Figure 2 are slightly lower than that calculated by Rasmussen et al. (2000). The activation energy of 2.7 eV was a room temperature value calculated by Rasmussen, Jacobsen, Leffers, and Pedersen (1997) by means of molecular dynamics using the Verlet algorithm after the temperature was stabilized via Andersen thermalization. They mention that this result is higher than estimates by Bonneville, Escaig, and Martin (1988) and by Püschl and Schoeck (1993), so there is certainly variation in such calculations, particularly when accounting for temperature. The temperature dependence of the activation energies is discussed in more detail in Section 6.

It is of interest to consider the activation energy for large stresses. In that limit

$$E_x \sim \frac{0.1}{\alpha} \gamma b^2 \left(\frac{d_0}{b} - 1 \right) \frac{G}{\hat{\sigma}}, \quad \hat{\sigma} \rightarrow \infty, \quad (57)$$

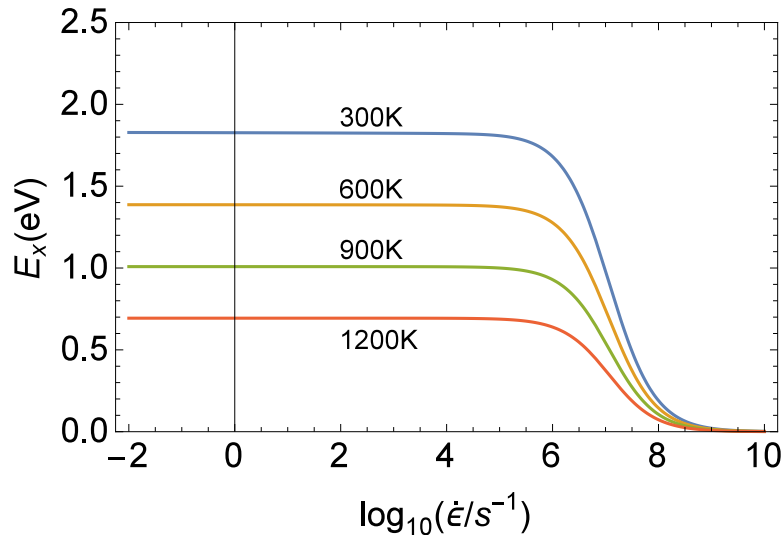


Figure 2: Single cross-slip activation energy as a function of strain rate and temperature. For these cases $\gamma = 50 \text{ mJ/ m}^2$.

so a plot of the cross-slip rate versus reciprocal stress on $\log - \log$ axes is a straight line of negative slope, as observed experimentally (Gilman, 1997).

We should mention that Equation (56), as well as Equation (160) in Section 4.2.1 for the double cross-slip activation energy, are not valid for metals with exceptionally high stacking fault energies, for example aluminum and palladium. The reason is that $d_0 \rightarrow b$, which is the atomic diameter in *fcc* metals, for $\gamma \rightarrow Gb/16\pi$, in which case the continuum dislocation theory we used to derive our stacking fault widths and activation energies breaks down. For aluminum at 300K with $G = 26 \text{ GPa}$, $b = 0.286 \text{ nm}$, and $\gamma = 140 \text{ mJ/m}^2$ (Hunter et al., 2014), we obtain $d_0/b = \mathcal{A}/b\gamma = 1.056$; $d_0 = b$ for $\gamma = Gb/16\pi = 148 \text{ mJ/m}^2$. On the other hand, for copper with $d_0/b \approx 5$, the continuum approximation is fine. Atomistic calculations of the stacking fault energies and activation energies are needed for aluminum and other metals with high stacking fault energies.

3.2.5 Annihilation due to Athermal and Thermal Single Cross-slip

As discussed, cross-slip contributes to dynamic recovery by making it possible for oppositely signed screw dislocations on different slip planes to annihilate (Kubin, Devincere, and Hoc, 2009, 2006). While cross-slip is enhanced at high temperatures and low strain rates (Püschl, 2002; Caillard and Martin, 2003; Li, Zhang, Yan, Yang, and Zhang, 2020), it can also happen athermally through spontaneous screw-screw annihilation (Rao, Dimiduk, El-Awady, Parthasarathy, Uchic, and Woodward, 2013). For the athermal case, we first look at the critical distances over which screw dislocations can spontaneously annihilate. Essmann and Mughrabi (1979) conducted experiments on copper and found no screw-screw dipoles with heights less than about 50 nm, which suggests that the screws spontaneously annihilate at distances up to 50 nm. However, as pointed out by Rasmussen et al. (2000) and Vegge, Rasmussen, Leffers, Pedersen, and Jacobsen (2001), those experiments do not rule out the presence of smaller dipoles. In sharp contrast to these experimental results, atomistic simulations by Rasmussen et al. (2000) and Vegge et al. (2001) indicate that spontaneous annihilation occurs only out to dipole heights of about 1 nm. Let h_c be the critical dipole height within which spontaneous annihilation occurs; annihilation of larger dipoles requires thermal activation.

Consider a segment of length L_x (cross-slip length) of a mobile screw dislocation gliding at velocity, v , and parallel segments of length L_x of opposite-signed immobile screw dislocations on the cross-slip planes. The areal number density of the parallel segments is $g_{ax} \rho_i$, hence the number of immobile segments with which the primary screw segment can mutually annihilate is $g_{ax} \rho_i h_c$ per unit distance along the primary slip plane; the corresponding mean free path for spontaneous annihilation is

$$L_f = \frac{1}{g_{ax} \rho_i h_c}. \quad (58)$$

The spontaneous (athermal) annihilation rate is v / L_f . At finite temperature the mobile segment may cross-slip via thermal activation to annihilate with immobile screw segments at dipole heights $h > h_c$. The mean annihilation rate per segment is equal to

$$\frac{v}{L_f} + g_{tx} \bar{v} \exp(-E_x(\hat{\sigma}) / k_B T) \equiv \frac{v}{L_f^{eff}}, \quad (59)$$

where k_B is the Boltzmann constant. The single cross-slip activation energy E_x is given by Equation (56). The plastic strain per annihilation in a crystal of volume V is ($\rho_m \sim L_x/V$, $L_f^{eff} \sim dx$ in Orowan relation)

$$d\epsilon = b (L_x/V) L_f^{eff}, \quad (60)$$

and the corresponding loss of dislocation is

$$d\rho_m^x = d\rho_i^x = -L_x / V. \quad (61)$$

From Equations (58) - (61) we obtain

$$\frac{d\rho_m^x}{d\epsilon} = \frac{d\rho_i^x}{d\epsilon} = -\frac{1}{b L_f^{eff}} = -\left\{ g_{ax} \frac{h_c}{b} \rho_i + g_{tx} \frac{\bar{v}}{b v} \exp(-E_x(\hat{\sigma}) / k_B T) \right\}. \quad (62)$$

The annihilation rate due to athermal and thermally activated single cross-slip followed by screw-screw annihilation is

$$\dot{\rho}_m^x = \dot{\rho}_i^x = -g_{ax} \frac{h_c}{b} \rho_i \dot{\epsilon} - g_{tx} \bar{v} \rho_m \exp(-E_x(\hat{\sigma}) / k_B T). \quad (63)$$

Like b , the critical dipole height varies as $\rho^{-1/3}$, i.e. $h_c = h_{c0} \eta^{-1/3}$.

4 Dislocation Multiplication

The dislocation sources included in this model are Frank-Read (FR) sources, Koehler sources, grain boundary nucleation, and dislocation generation from shock wave loading.

4.1 Frank-Read Sources

FR sources have been the subject of numerous theoretical and experimental studies over the decades since they were first described by Frank and Read (1950). It is now well established that they are one of the primary sources of dislocation during plastic deformation. We briefly describe the operation of a FR source (Steif and Clifton, 1979). Consider a dislocation pinned at two points, A and B , separated by a distance λ . It is assumed here that the pinning points are not impurities but instead consist of localized pileups in the network (the pileups may be formed as a result of the mobile

dislocation interacting with the network). FR sources can originate on grain boundaries, but this possibility is not accounted for in the present model. The dislocation connecting A and B bows out under the applied stress. If the effective applied stress (applied stress minus network back stress), $\hat{\sigma}$, exceeds the critical value

$$\sigma_c^{FR} = \frac{Gb}{\lambda}, \quad (64)$$

then the expansion of the bowing segment is unstable, so it continues to expand and loop around the pinning points until the two lobes on the back side of the source touch and self-annihilate over a length of order λ , leaving a new segment connecting A and B and an expanding outer loop. The new segment re-starts the process. Under sufficient loading, FR sources can emit many dislocation loops, thus contributing to the overall dislocation density. Note that only large sources operate at low stresses, or equivalently, relatively large stresses are needed to operate small sources.

It is worth highlighting that the nucleation of FR sources in 2D simulations is commonly governed by a relation that is analogous to Equation (64). For example, in the classic paper of Van der Giessen and Needleman (1995) on discrete dislocation plasticity, FR sources in 2D are modeled as dislocation dipoles where the distance between the dislocations, L_{nuc} is determined by the critical stress, σ_{nuc} , for dipole formation according to

$$L_{nuc} = \frac{1}{2\pi(1-\nu)} \frac{Gb}{\sigma_{nuc}}. \quad (65)$$

This expression ensures that the resolved shear stress, σ_{nuc} , balances the attractive shear stress that the two dislocations exert on one another.

The collective behavior of an ensemble of FR sources is immensely complex, and has never been thoroughly investigated. Since our goal here is to develop a practical model of plastic deformation, we must neglect the details while retaining the predominant features of FR source operation. In particular, we neglect FR-FR source interactions. For example, consider two equal-sized sources on the same glide plane formed at about the same time. In addition assume equal Burgers vectors. In this case the expanding loops mutually annihilate between the sources, resulting in larger expanding loops. If their Burgers vectors are opposite then annihilation cannot occur, in which case the evolution of each source is essentially that of a source in a half space. For arbitrary Burgers vectors, junction forming reactions could take place, though follow-up loops might Orowan loop around these obstacles. In general, the formation times will differ significantly, so one must consider the evolution of a small source near a larger one. In this case it seems that the larger source would stall the expansion of the smaller. However, sources on different glide planes should not prevent expansion of their neighbors to the grain boundaries. Thus, due to these complexities, we neglect FR-FR source interactions in the formulation presented here.

In Section 2 we presented our models for immobile dislocation generation via random homogeneous network and grain boundary storage of mobile dislocation. In contrast, FR sources can generate immobile dislocation by pileup formation either on grain boundaries or in the network around the sources. The dynamics of pileup formation is non-random, hence immobile dislocation generation by FR pileup formation is a mechanism distinct from the network and grain boundary storage considered in Section 2.

It is well known that back stresses resulting from loop generation control, in part, the source operation. In particular, the loop production rate is expected to decrease as the back stress builds and the radial velocities of the inner loops decrease with increasing back stress. While this model does account for FR sources turning off due to accumulated back stresses, it does not account for the rate decrease of the radial velocity of the generated dislocation loops.

Here we distinguish between FR sources, which are generating mobile dislocation, and FR configurations, which are sources only if $\hat{\sigma}$ is greater than the critical stress given by Equation (64). Alternatively, a FR configuration of size λ is not a source if $\lambda_c = Gb/\hat{\sigma} > \lambda$. Since $\lambda \gtrsim \mathcal{L}_i$ there are non-operative configurations if $\lambda_c = Gb/\hat{\sigma} > \mathcal{L}_i$, i.e. if the stress is less than Gb/\mathcal{L}_i .

The FR source operation in a polycrystal is roughly averaged by locating the source at the center of a grain. We idealize the formation of each dislocation loop of a FR source as occurring at $r = 0$, i.e. the midpoint of the source, and approximate the radial velocity of the loops at time t'' by the mean mobile dislocation velocity

$$v(t'') = \frac{\dot{\epsilon}(t'')}{b(t'') \rho_m(t'')} ; \quad (66)$$

the time dependence of the Burgers vector magnitude is due to variations in material density, hence $b(t'') = b_0 (\rho_0/\rho(t''))^{1/3}$ where ρ_0 is the ambient density. For a t' -source, that is, a source formed at t' , the outer loop radius at time t'' is

$$r(t'', t') = \int_{t'}^{t''} dt''' v(t'''). \quad (67)$$

The mean separation between adjacent expanding loops is approximately constant and roughly equal to the source size, λ ; this is evident in both electron micrographs of FR sources and from numerical simulations of source operation (Moulin, Condat, and Kubin, 1997; Faradjian, Friedman, and Chrzan, 1999; Jacques, Vallino, Serbena, and George, 2000). It follows that at time t'' the distance travelled by loop k ($k = 1$ is the outer loop) is given by

$$r_k(t'', t') = r(t'', t') - (k - 1)\lambda(t''), \quad (68)$$

where

$$\lambda(t'') = \lambda(t') (\rho(t')/\rho(t''))^{1/3}. \quad (69)$$

As loops expand from a FR source, mobile dislocation is lost through storage and annihilation mechanisms. The rate of loss of dislocation line length can be calculated using the results of Section 2 and Subsection 3.1. The rate of loss of dislocation from loop k at time t'' is

$$2\pi r_k \dot{r}_k (g_{ami} + g_{sn}) \rho_i^{1/2}(t''), \quad (70)$$

where $r_k \equiv r_k(t'', t')$ is the loop radius and the derivative is with respect to t'' . Note that annihilation reactions between the expanding loops and other mobile dislocations is neglected. The rate of generation of dislocation due to expansion is $2\pi \dot{r}_k$. It follows that

$$\frac{dl_m^{(k)}}{dt''} = 2\pi \dot{r}_k(t'', t') \left[1 - (g_{ami} + g_{sn}) r_k(t'', t') \rho_i^{1/2}(t'') \right], \quad (71)$$

where $l_m^{(k)}$ is the length of mobile dislocation in loop k .

We could straightforwardly continue this line of development to a final expression for the FR-generated mobile dislocation. This approach would entail integrating $v(t''')$ over t''' to obtain $r(t'', t')$, integrating Equation (71) over t'' to get the length of dislocation remaining in loop k , and finally integrating over t' , the source formation time. However, the resulting expression would be too complex for practical applications, thus we must make an approximation. We approximate $v(t''')$, $\rho_m(t''')$, $\rho_i(t''')$, $\lambda(t''')$, $b(t''')$, and $R(t''')$ for $t'' \in [t', t]$, where t is the current time, by their values

at t' , the time of source formation. This formation-time approximation retains the predominant physics and eliminates two integrations.

In the formation-time approximation the radius at time t'' of the outermost loop of a t' -source is

$$r(t'', t') = v(t') (t'' - t'). \quad (72)$$

Equation (68) is replaced by

$$r_k(t'', t') = v(t') (t'' - t') - (k - 1)\lambda(t'), \quad (73)$$

and Equation (71) becomes

$$\frac{dl_m^{(k)}}{dt''} = 2\pi v(t') \left[1 - (g_{ami} + g_{sn}) r_k(t'', t') \rho_i^{1/2}(t') \right]. \quad (74)$$

The formation time, t_{k0} , of loop k is the solution of $r_k(t_{k0}, t') = 0$

$$t_{k0}(t') = t' + \frac{(k - 1)\lambda(t')}{v(t')}. \quad (75)$$

Loop k of the t' -source has expanded to radius $R_k(t')$ at time

$$t_{Rk}(t') = t' + \frac{R_k(t') + (k - 1)\lambda(t')}{v(t')}. \quad (76)$$

Integrating Equation (74) over t'' from t_{k0} to t_{Rk} yields the mean length of dislocation remaining in loop k at radius $R_k(t')$

$$\begin{aligned} l_{Rk}(t') &= 2\pi R_k(t') \mathcal{D}_k(t'), \\ \mathcal{D}_k(t') &= 1 - \frac{1}{2} (g_{ami} + g_{sn}) R_k(t') \sqrt{\rho_i(t')} = 1 - R_k(t')/R_e(t'). \end{aligned} \quad (77)$$

The mean fraction of dislocation remaining in loop k at radius R_k is \mathcal{D}_k . It vanishes (by definition) at the loop extinction radius

$$R_e(t') = \frac{2}{(g_{ami} + g_{sn}) \sqrt{\rho_i(t')}}. \quad (78)$$

When loops from a FR source encounter a grain boundary in a polycrystal they will form a pileup; in general, the dislocations cannot penetrate the non-crystalline boundary, especially if the boundary is high angle. However, as a result of dislocation storage, pileups can also form in the immobile network. By invoking the Orowan relation with $v = dx/dt$, Equation (3) may be written as

$$\frac{d\rho_m}{dx} = -g_{sn} \sqrt{\rho_i} \rho_m, \quad (79)$$

which shows that the mean free path for network storage is

$$l_{sn}(t') = \frac{1}{g_{sn} \sqrt{\rho_i(t')}}. \quad (80)$$

We accordingly use $l_{sn}(t')$ as the radius at which the outermost loop of a t' -source is stored in the network. In the absence of cross-slip and grain boundary storage the immobile density evolution is simply $d\rho_i/d\epsilon = (g_{sn} - g_{ami}) \times b^{-1} \sqrt{\rho_i}$ at constant material density. Since the immobile density must increase with the plastic strain then $g_{sn} > g_{ami}$. It follows that $l_{sn}(t') < R_e(t')$. If $l_{sn}(t') <$

$R(t') = D(t')/2$ then the pileups are formed in the network, and if $R(t') < l_{sn}(t')$ the pileups are on the grain boundaries.

The outer radius of the dislocation pileup around a t' -source is

$$R_p(t') = \min [l_{sn}(t'), R(t')] . \quad (81)$$

It is trivial to prove that R_p is always less than the loop extinction radius, R_e . If $l_{sn} < R$ then $R_p/R_e = l_{sn}/R_e = (1 + g_{ami}/g_{sn})/2 < 1$, and if $R < l_{sn} < R_e$ then again $R_p/R_e < 1$. The pileup around a t' -source begins at time $t_p(t') = t' + \tau_p(t')$ where

$$\tau_p(t') = R_p(t')/v(t') \quad (82)$$

is the time required for the outermost loop to reach the pileup radius. The number of loops around the source at time $t_p(t')$ is

$$n_p(t') = R_p(t')/\lambda(t') . \quad (83)$$

The pileup creates a back stress on the source that reduces the net stress at the source, possibly below the critical stress for source operation. We now calculate the back stress exerted on the FR source.

The stress field around a circular dislocation loop was calculated by Langdon (2000). Following Langdon (2000) we take $\mathbf{b} = (0, b, 0)$. The stress field is obtained by line integration of the Peach-Koehler formula around a circular loop of radius r_0 . The integration direction is counterclockwise, hence the line sense vector at $(x, y, z) = (r_0, 0, 0)$ is $\hat{\xi} = (0, 1, 0)$. Since our interest is a loop formed by a FR source at the origin, the source also has $\mathbf{b} = (0, b, 0)$ and the initial straight segment must have $\hat{\xi} = (0, 1, 0)$ and bow out in the $+x$ -direction. The glide force per unit length on this segment is $-b\sigma_{yz}(1, 0, 0)$, thus bow out in the $+x$ -direction requires $\sigma_{yz} < 0$. In the limit $r/r_0 \rightarrow 0$, i.e. in the neighborhood of the source, the σ_{yz} component of the loop stress field is

$$\sigma_{yz}^{(loop)} = \frac{5}{18} \frac{G b}{r_0} . \quad (84)$$

Since the applied stress and the loop stress near the origin are of opposite sign, the loop exerts a back stress on the source.

We now approximately calculate the back stress due to the expanding loops around a FR source up to time $t_p(t')$, the beginning of pileup formation. Retardation is neglected, i.e. the back stress is calculated with the static stress fields of the loops. The maximum number of loops is $n_p(t')$; see Equation (83). To calculate the back stress it is necessary to account for the loss of loop dislocation to annihilation and storage. Let $k \leq n_p$ denote the number of loops around the source. The contribution of loop $j \leq k$ to the back stress must be reduced by a factor of $\mathcal{D}_j = 1 - R_j/R_e$, the fraction of loop dislocation remaining at radius $R_j = (k - j + 1)\lambda$; note that $R_1 = k\lambda$ is the radius of the outermost loop. Using Equation (84) we obtain the back stress as a function of R_1

$$\begin{aligned} \sigma_b^{(loop)}(R_1) &= \frac{5}{18} G b \sum_{j=1}^k \frac{\mathcal{D}_j(t')}{R_j(t')} = \frac{5}{18} G b \sum_{j=1}^k \left(\frac{1}{j\lambda(t')} - \frac{1}{R_e(t')} \right) , \\ &\approx \frac{5}{18} \sigma_c^{FR}(t') \left(\gamma_E + \ln \frac{R_1(t')}{\lambda(t')} - \frac{R_1(t')}{R_e(t')} \right) , \end{aligned} \quad (85)$$

where $\gamma_E = 0.577\dots$ is Euler's constant. $\sigma_b^{(loop)}(R_1)$ is an increasing function of R_1 up to R_e ($R_1 = R_e$ corresponds to $\mathcal{D}_n = 0$, $n = R_e/\lambda$), and since $R_p < R_e$ it is increasing for $R_1 \leq R_p$, as

expected. The source is turned off at $R_1 \leq R_p$ for an effective applied stress equal to

$$\hat{\sigma}(R_1) = \left[1 + \frac{5}{18} \left(\gamma_E + \ln \frac{R_1}{\lambda} - \frac{R_1}{R_e} \right) \right] \sigma_c^{FR} \quad (86)$$

which is $\mathcal{O}(\sigma_c^{FR})$. If $\hat{\sigma} \geq \hat{\sigma}(R_p)$ then $R_1 \rightarrow R_p$ and pileup formation begins. The distribution of loop radii changes from equally spaced to the equilibrium distribution of a circular pileup. We employ the radial distribution function derived by Chou (1972). Loop j changes its radius from $(n_p - j + 1) \lambda(t')$ to

$$R_j(t') = R_p(t') \left[1 - \left(\frac{j-1}{n_p} \right)^2 \right]^{1/2} = [n_p^2 - (j-1)^2]^{1/2} \lambda(t'). \quad (87)$$

Since $R_j^2 - R_{j+1}^2 = (R_p^2/n_p^2) (2j-1)$ we see that the loop spacing increases with j , i.e. the leading loops are the most closely spaced. The corresponding back stress is

$$\sigma_b^{(p)}(t_p(t')) = \frac{5}{18} G b \sum_{j=1}^{n_p} \left[\frac{1}{R_j(t')} - \frac{1}{R_e(t')} \right]. \quad (88)$$

Taking $j \rightarrow n_p - j + 1$ and using $n_p = R_p/\lambda$ the sum becomes

$$\frac{1}{\lambda(t')} \left[\sum_{j=1}^{n_p} \frac{1}{\sqrt{j(2n_p - j)}} - \frac{R_p(t')}{R_e(t')} \right]. \quad (89)$$

With the approximation

$$\sum_{j=1}^n \frac{1}{\sqrt{j(2n-j)}} \approx \int_0^n \frac{dx}{\sqrt{2nx - x^2}} = \frac{\pi}{2} \quad (90)$$

the pileup (p) back stress at time $t_p(t')$ is

$$\sigma_b^{(p)}(t_p(t')) = \frac{5}{18} \sigma_c^{FR}(t') \left[\frac{\pi}{2} - \frac{R_p(t')}{R_e(t')} \right]. \quad (91)$$

Continued operation of the source requires an effective applied stress greater than

$$\hat{\sigma}_{\Omega=1}(t') = \sigma_b^{(p)}(t_p(t')) + \sigma_c^{FR}(t') = \left\{ 1 + \frac{5}{18} \left[\frac{\pi}{2} - \frac{R_p(t')}{R_e(t')} \right] \right\} \sigma_c^{FR}(t'). \quad (92)$$

In order to minimize model complexity we henceforth neglect FR source formation at effective applied stresses less than this value, which is $\mathcal{O}(\sigma_c^{FR})$. In our model FR sources always form pileups and are extinguished by pileup back stresses.

For $t'' > t_p(t')$ the pileup back stress on a t' -source is

$$\sigma_b^{(p)}(t'') = \frac{5}{18} \frac{G b n(t'', t')}{R_p(t')} \left[\frac{\pi}{2} - \frac{R_p(t')}{R_e(t')} \right], \quad (93)$$

where

$$n(t'', t') = \frac{v(t')(t'' - t')}{\lambda(t')} \quad (94)$$

is the number of loops emitted by the t' -source up to time t'' . The FR source is extinguished when the net stress at the source, $\hat{\sigma} - \sigma_b^{(p)}$, is less than the critical stress for loop generation, namely $\sigma_c^{FR} = Gb/\lambda$, thus the condition for turning off the source is $\sigma_b^{(p)} = \hat{\sigma} - \sigma_c^{FR}$. The source ceases to operate at time $t_{op}(t') = t' + \tau_{op}(t')$, where τ_{op} is the operating time. Using Equation (94) we find that there are

$$n_{op}(t') = n(t_{op}(t'), t') = \frac{v(t')}{\lambda(t')} \tau_{op}(t') \quad (95)$$

loops in the pileup. The condition $\sigma_b^{(p)}(t_{op}(t')) = \hat{\sigma}(t') - \sigma_c^{FR}(t')$ plus Equations (82), (93), and (95) result in

$$\begin{aligned} \tau_{op}(t') &= \tau_p(t') \Omega(t'), \\ \Omega(t') &= (18/5) [\pi/2 - R_p(t')/R_e(t')]^{-1} [\hat{\sigma}(t')/\sigma_c^{FR}(t') - 1] \theta [\hat{\sigma}(t') - \hat{\sigma}_{\Omega=1}(t')] , \end{aligned} \quad (96)$$

where $\hat{\sigma}_{\Omega=1}(t')$ is the stress given in Equation (92) and for which $\Omega(t') = 1$; $\Omega(t') > 1$ for stresses greater than $\hat{\sigma}_{\Omega=1}(t')$. It follows that $\tau_{op}(t') \geq \tau_p(t')$ for $\hat{\sigma} \geq \hat{\sigma}_{\Omega=1}$ and $\tau_{op} = 0$ if $\hat{\sigma} < \hat{\sigma}_{\Omega=1}$.

To calculate the total length of mobile and immobile dislocation from a t' -source we must consider three cases: $t < t_p(t') = t' + \tau_p(t')$, $t_p(t') < t < t_{op}(t')$, and $t > t_{op}(t')$.

For $t < t_p(t')$ the loops are expanding toward $R_p(t')$ and the total length of mobile dislocation is approximately $\pi R_1^2(t, t')/\lambda(t')$ and therefore increasing quadratically with time.

For $t_p(t') < t < t_{op}(t')$ a pileup is forming with outer radius $R_p(t')$. Here we do not calculate the details of the pileup dynamics in order to separate the total dislocation into its mobile and immobile components. Instead we adopt the rough approximation that the inner $n_p - 1 \approx n_p$ loops are mobile and equally spaced at $\lambda(t')$, thus the total length of mobile dislocation is $\pi R_p^2(t')/\lambda(t')$, while the outer loops are in a narrow pileup with radius $R_p(t')$ and therefore immobile. At time $t_{op}(t')$ the pileup is comprised of $n_{\partial}(t') = n_{op}(t') - n_p(t')$ immobile loops of radius $R_p(t')$. The total length of immobile dislocation in the pileup for $t_p(t') < t < t_{op}(t')$ is

$$\begin{aligned} l_i^{FR}(t, t') &= 2 \pi R_p(t') n_{\partial}(t') \frac{t - t' - \tau_p(t')}{\tau_{op}(t') - \tau_p(t')} \\ &= 2 \pi R_p(t') \frac{v(t')}{\lambda(t')} (t - t' - \tau_p(t')) ; \end{aligned} \quad (97)$$

note that λ/v is the time between loop emissions.

When the source has ceased operating, that is $t > t_{op}(t')$, the previously mobile dislocation at $r < R_p$ becomes immobile; thus the length of immobile dislocation rapidly increases by $\pi R_p^2(t')/\lambda(t')$.

In view of the above results for $t < t_p(t')$, $t_p(t') < t < t_{op}(t')$, and $t > t_{op}(t')$ the lengths of mobile and immobile dislocation around a t' -source are

$$\begin{aligned} l_m^{FR}(t, t') &= \frac{\pi R_p^2(t')}{\lambda(t')} \left\{ \frac{(t - t')^2}{\tau_p^2} \theta(\tau_p + t' - t) + \theta(\tau_{op} + t' - t) \theta(t - t' - \tau_p) \right\} , \\ l_i^{FR}(t, t') &= 2 \pi R_p(t') \left\{ n_{\partial}(t') \frac{t - t' - \tau_p}{\tau_{op} - \tau_p} \theta(\tau_{op} + t' - t) \theta(t - t' - \tau_p) + \left[n_{\partial}(t') + \frac{R_p(t')}{2 \lambda(t')} \right] \theta(t - t' - \tau_{op}) \right\} , \end{aligned}$$

where $\tau_p \equiv \tau_p(t')$, $\tau_{op} \equiv \tau_{op}(t')$, $\Omega(t') \geq 1$, and

$$n_{\partial}(t') = \frac{v(t')}{\lambda(t')} [\tau_{op}(t') - \tau_p(t')] = \frac{R_p(t')}{\lambda(t')} [\Omega(t') - 1] . \quad (98)$$

Equations (98) may be more concisely expressed in terms of the variable $x = (t - t')/\tau_p(t')$:

$$\begin{aligned}
l_{m,i}^{FR}(t, t') &= \frac{\pi R_p^2(t')}{\lambda(t')} \mathcal{B}_{m,i}(t, t'; \Omega) \theta(\Omega - 1), \\
\mathcal{B}_m(t, t'; \Omega) &= x^2 \theta(1 - x) + \theta(\Omega - x) [1 - \theta(1 - x)], \\
\mathcal{B}_i(t, t'; \Omega) &= 2(x - 1) \theta(x - 1) \theta(\Omega - x) + (2\Omega - 1) [1 - \theta(\Omega - x)],
\end{aligned} \tag{99}$$

where $\Omega \equiv \Omega(t')$. The discontinuities in $\mathcal{B}_{m,i}$ and their time derivatives are of course unphysical artifacts of our simplified modeling of the complex process of FR source formation and dislocation generation. Such discontinuities are often problematic for numerical simulations. Therefore, in Appendix C we obtain smooth (C^∞) approximations to $\mathcal{B}_{m,i}$ and $\dot{\mathcal{B}}_{m,i}$.

The pileup radius, R_p , is the smaller of $l_{sn} = \mathcal{L}_i/g_{sn}$ or R , the mean grain radius. Stress-strain data are usually obtained for samples with initial dislocation densities $\gtrsim 10^9 \text{ cm}^{-2}$; the large-strain dislocation densities are generally $\lesssim 10^{12} \text{ cm}^{-2}$ (Williamson and Smallman, 1956; Borbely and Driver, 2005; Hu, Zhao, Fu, Li, and Liu, 2017; de Sousa, Sordi, and Brandao, 2018). The corresponding values of \mathcal{L}_i range from $0.01 \mu\text{m}$ to $0.3 \mu\text{m}$. Comparisons of our model to stress-strain data (shown below in Section 6) show that $g_{sn} \sim 0.1$, hence $3 \mu\text{m} \gtrsim l_{sn} \gtrsim 0.1 \mu\text{m}$. Since sample grain sizes (diameters) are typically $\gtrsim 10 \mu\text{m}$, i.e., $R \gtrsim 5 \mu\text{m}$, we conclude that generally $l_{sn} < R$, hence $R_p = \mathcal{L}_i/g_{sn}$. Henceforth we consider only network pileups for which

$$R_p(t')/R_e(t') = \frac{1}{2} (1 + g_{ami}/g_{sn}). \tag{100}$$

It follows from Equation (96) that

$$\Omega(\lambda(t'), \hat{\sigma}(t')) = (C_\Omega - 1)^{-1} (\lambda(t')/\lambda_c(t') - 1) \theta(\lambda(t')/\lambda_c(t') - C_\Omega), \tag{101}$$

where

$$\begin{aligned}
\lambda_c(t') &= Gb/\hat{\sigma}(t'), \\
C_\Omega &= 1 + \frac{5}{36} (\pi - 1 - \frac{g_{ami}}{g_{sn}}).
\end{aligned} \tag{102}$$

Our discussion of FR dislocation sources up to this point has focused on sources of a given size formed at time t' , namely $\lambda(t')$. We now consider the formation of FR sources via the intersection of mobile dislocations with the immobile dislocation network (i.e., forest dislocations). Analytic sub-models are obtained for:

- The size distribution, $f^{FR}(\lambda)$, of FR configurations, that is, mobile dislocations pinned at two points and bowing between them;
- The probability, $P_{op}(\lambda)$, that a randomly chosen FR configuration is operating, i.e., that it is a FR source;
- The size distribution of FR sources, $f_{op}^{FR}(\lambda)$;
- The mean of Ω over sources that form pileups;
- The mean source size, $\bar{\lambda}$.

These sub-models are constructed on the bases of one- and two-dimensional models for the mobile-network intersections. The two-dimensional model is presented in Appendix B. Subsequent results utilize the one-dimensional model.

4.1.1 Size distribution of FR configurations

In the one-dimensional model we consider the intersection of a mobile dislocation with a parallel linear array of immobile dislocations intersecting the glide plane. The forest dislocations are idealized as equally spaced by \mathcal{L}_i , the mean distance between immobile dislocations. When the mobile dislocation intersects the array of immobile dislocations the probability that an intersection node is formed at a given site in the array is P_{FR} . Consider an occupied site, i.e., a node. In a given direction from that site the probability that the next k sites are unoccupied while site $k + 1$ is occupied is

$$(1 - P_{FR})^k P_{FR}, \quad (103)$$

hence the probability of a segment of length n is

$$P(n) = 2P_{FR}(1 - P_{FR})^{n-1}. \quad (104)$$

The corresponding size distribution of FR configurations is

$$f^{FR}(\lambda) = \mathcal{N}\mathcal{L}_i^{-1}P_{FR}(1 - P_{FR})^{\lambda/\mathcal{L}_i-1}\theta(\lambda - \mathcal{L}_i), \quad (105)$$

where \mathcal{N} is a normalization factor. Since the integral of $f^{FR}(\lambda)$ over $\lambda \in [0, \infty)$ is unity, we obtain

$$f^{FR}(\lambda) = \mathcal{L}_i^{-1} \ln\left(\frac{1}{1 - P_{FR}}\right) (1 - P_{FR})^{\lambda/\mathcal{L}_i-1}\theta(\lambda - \mathcal{L}_i). \quad (106)$$

4.1.2 Operating probability

This is the probability that a randomly chosen FR configuration is operating, i.e., it is a FR source. We account only for FR configurations with $\lambda \geq C_\Omega\lambda_c = C_\Omega Gb/\hat{\sigma}$ (see Equation (101)), thus

$$P_{op}(\hat{\sigma}) = \int_{C_\Omega\lambda_c}^{R_p} d\lambda f^{FR}(\lambda) = \mathcal{L}_i \int_{C_\Omega\sigma_\mathcal{L}/\hat{\sigma}}^{1/g_{sn}} dx f^{FR}(\mathcal{L}_i x), \quad (107)$$

where $\sigma_\mathcal{L} = Gb/\mathcal{L}_i$. Since $1/g_{sn} \gg 1$ we take the upper limit of integration to ∞ and get

$$P_{op}(s) = 1 + [(1 - P_{FR})^{C_\Omega/s-1} - 1]\theta(C_\Omega - s), \quad (108)$$

where

$$s = \frac{\hat{\sigma}}{\sigma_\mathcal{L}} = \frac{\hat{\sigma}\mathcal{L}_i}{Gb}. \quad (109)$$

Henceforth we use the approximation

$$P_{op}(s) \approx 1 - e^{-\chi s/C_\Omega}, \quad (110)$$

where

$$\chi = 4 \ln^{-1}\left(\frac{1}{1 - P_{FR}}\right) (1 - P_{FR})^{2 \ln^{-1}[1/(1 - P_{FR})]-1}. \quad (111)$$

4.1.3 Size distribution of FR sources

The size distribution of FR sources is obtained from the size distribution of FR configurations. If the configuration size $\lambda > R_p$ then it is not operative. At effective applied stresses $\hat{\sigma} < C_\Omega \sigma_{\mathcal{L}}$, the size of the operating configurations satisfy $R_p \geq \lambda \geq C_\Omega \lambda_c \geq \mathcal{L}_i$ where $\lambda_c = Gb/\hat{\sigma}$. It may be that $C_\Omega \lambda_c < \mathcal{L}_i$ in which case all configurations with $\lambda \leq R_p$ are operating. The source size distribution is given by

$$\begin{aligned}
f_{op}^{FR}(\lambda) &= f^{FR}(\lambda) \left\{ \left(\int_{C_\Omega \lambda_c}^{R_p} f^{FR}(\lambda') d\lambda' \right)^{-1} \theta(\lambda - C_\Omega \lambda_c) \theta(C_\Omega \lambda_c - \mathcal{L}_i) \right. \\
&\quad \left. + \left(\int_{\mathcal{L}_i}^{R_p} f(\lambda') d\lambda' \right)^{-1} \theta(\lambda - \mathcal{L}_i) \theta(\mathcal{L}_i - C_\Omega \lambda_c) \right\} \theta(R_p - \lambda) \\
&= \mathcal{L}_i^{-1} \ln \left(\frac{1}{p} \right) p^{\lambda/\mathcal{L}_i} \left\{ \frac{\theta(\lambda - C_\Omega \lambda_c) \theta(C_\Omega \lambda_c - \mathcal{L}_i)}{p^{\lambda_c/\mathcal{L}_i} - p^{1/g_{sn}}} + \frac{\theta(\lambda - \mathcal{L}_i) \theta(\mathcal{L}_i - C_\Omega \lambda_c)}{p - p^{1/g_{sn}}} \right\} \theta(\mathcal{L}_i/g_{sn} - \lambda),
\end{aligned} \tag{112}$$

where $p = 1 - P_{FR}$.

4.1.4 Mean $\Omega(\lambda, \hat{\sigma})$ over source sizes

The mean of $\Omega(\lambda, \hat{\sigma})$ over FR sources that form pileups is

$$\bar{\Omega}_\lambda(\hat{\sigma}) = \int_0^\infty \Omega(\lambda, \hat{\sigma}) f_{op}^{FR}(\lambda) d\lambda, \tag{113}$$

where $\Omega(\lambda, \hat{\sigma})$ is given by Equation (101). We find

$$(C_\Omega - 1) \bar{\Omega}_\lambda(s) = \frac{s}{\ln(1/p)} - 1 + \frac{C_\Omega p^{C_\Omega/s} - (1/g_{sn}) s p^{1/g_{sn}}}{p^{C_\Omega/s} - p^{1/g_{sn}}} \theta(C_\Omega - s) + s \frac{p - (1/g_{sn}) p^{1/g_{sn}}}{p - p^{1/g_{sn}}} \theta(s - C_\Omega), \tag{114}$$

where $s = \hat{\sigma} \mathcal{L}_i / Gb$. We note that $\lim_{s \rightarrow C_\Omega+} \bar{\Omega}_\lambda(s) = \lim_{s \rightarrow C_\Omega-} \bar{\Omega}_\lambda(s)$ so $\bar{\Omega}_\lambda(s)$ is a continuous function of s . When the source size is R_p , its maximum value, the effective applied stress is $\hat{\sigma} = C_\Omega Gb / R_p$, which is equivalent to $s = C_\Omega \mathcal{L}_i / R_p = C_\Omega g_{sn} \equiv s_{min} \ll 1$.

We now construct a simple, but accurate, approximation for $\bar{\Omega}_\lambda$ based on the following limiting values

$$\begin{aligned}
\lim_{s \rightarrow s_{min}} \bar{\Omega}_\lambda(s) &= 1, \\
\bar{\Omega}_\lambda(s) &\sim \frac{s}{C_\Omega - 1} \left[\frac{p - (1/g_{sn}) p^{1/g_{sn}}}{p - p^{1/g_{sn}}} + \frac{1}{\ln(1/p)} \right] \equiv M_\Omega s, \quad s \rightarrow \infty.
\end{aligned} \tag{115}$$

Since $s_{min} \ll 1$, we make the approximation $\bar{\Omega}_\lambda(0) = 1$. Our approximation for $\bar{\Omega}_\lambda(s)$ is

$$\bar{\Omega}_\lambda(s) = M_\Omega s + 1. \tag{116}$$

4.1.5 Mean FR source size

The mean FR source size is

$$\bar{\lambda} = \int_0^\infty d\lambda \lambda f_{op}^{FR}(\lambda). \tag{117}$$

We obtain

$$\frac{\bar{\lambda}}{\mathcal{L}_i} = \frac{(C_\Omega/s)p^{C_\Omega/s} - (1/g_{sn})p^{1/g_{sn}}}{p^{C_\Omega/s} - p^{1/g_{sn}}} \theta(C_\Omega - s) + \frac{p - (1/g_{sn})p^{1/g_{sn}}}{p - p^{1/g_{sn}}} \theta(s - C_\Omega) + \frac{1}{\ln(1/p)} \quad (118)$$

where $s = \hat{\sigma}\mathcal{L}_i/Gb \geq C_\Omega g_{sn}$. If $s < C_\Omega g_{sn}$ then $C_\Omega \lambda_c > R_p$ in which case there are no FR sources that form pileups. The mean size has its maximum value, $R_p = l_{sn}$, for $s = C_\Omega g_{sn} = s_{min}$.

We now obtain a smooth approximation for $\bar{\lambda}/\mathcal{L}_i$ in the one-dimensional FR configuration formation model. The strategy is to construct a Padé approximant based on the $s \rightarrow C_\Omega g_{sn}$ and $s \rightarrow \infty$ limits of $\bar{\lambda}/\mathcal{L}_i$. The expansion of $\bar{\lambda}/\mathcal{L}_i$ to the first order in $s - C_\Omega g_{sn}$ is given by

$$\frac{\bar{\lambda}}{\mathcal{L}_i} = \frac{1}{g_{sn}} - \frac{1}{2g_{sn}^2}(s - C_\Omega g_{sn}) + \mathcal{O}(s - C_\Omega g_{sn})^2. \quad (119)$$

For $s \rightarrow \infty$ we obtain

$$\frac{\bar{\lambda}}{\mathcal{L}_i} \sim \frac{\bar{\lambda}_\infty}{\mathcal{L}_i} = \frac{p - (1/g_{sn})p^{1/g_{sn}}}{p - p^{1/g_{sn}}} + \frac{1}{\ln(1/p)}. \quad (120)$$

Our Padé approximant is

$$\frac{\bar{\lambda}}{\mathcal{L}_i} = \frac{(s/C_\Omega - 3g_{sn})\bar{\lambda}_\infty/\mathcal{L}_i + 2}{s/C_\Omega + g_{sn} - 2g_{sn}^2\bar{\lambda}_\infty/\mathcal{L}_i}. \quad (121)$$

Its expansion to first order in $s - C_\Omega g_{sn}$ is given by Equation (119).

We now consider the rate of formation of FR configurations. In crystal volume V the mobile dislocation has total length l_m , thus $\rho_m = l_m/V$. The mean time required to glide between network dislocations is $\Delta t = \mathcal{L}_i/v$. The mobile dislocation intersects the network at points which are on average a distance \mathcal{L}_i apart; hence, there are l_m/\mathcal{L}_i intersection points on average. An intersection results in a FR pinning point (A or B) with probability P_{FR} , hence P_{FR} accounts for the likelihood that the intersection point is a localized pileup. Consequently there are $P_{FR} l_m/\mathcal{L}_i$ points on the mobile dislocation that become pinning points of FR configurations in time Δt , thus there are $\tilde{g}_{FR} P_{FR} l_m/2\mathcal{L}_i$ FR sources formed by the mobile dislocation in V in time Δt . The rate of formation at time t' of FR configurations per unit volume is

$$\dot{n}_{FR}(t') = \frac{1}{V \Delta t} \tilde{g}_{FR} \frac{P_{FR} l_m}{2\mathcal{L}_i} \Big|_{t'} = \frac{1}{2} \tilde{g}_{FR} P_{FR} \frac{\rho_i(t') \dot{\epsilon}(t')}{b(t')}. \quad (122)$$

The rate of formation of FR sources is a fraction $P_{op}(\hat{\sigma})$ of \dot{n}_{FR}

$$\dot{n}_{op}^{FR}(t') = \frac{1}{2} \tilde{g}_{FR} P_{FR} P_{op}(\hat{\sigma}(t')) \frac{\rho_i(t') \dot{\epsilon}(t')}{b(t')}. \quad (123)$$

We emphasize that this is the rate of formation of t' -sources per unit t' -volume. The corresponding formation rate per unit t -volume (current volume) is clearly $\dot{n}_{op}^{FR}(t') \rho(t)/\rho(t')$. The number of t' -sources (sources formed in $(t', t' + dt')$) per unit t -volume is

$$\frac{\rho(t)}{\rho(t')} \dot{n}_{op}^{FR}(t') dt'. \quad (124)$$

We approximately calculate the mobile and immobile dislocation densities generated by FR sources by integrating the product of $l_{m,i}^{FR}(t, t')$ (see Equation (99)) for a mean source size and $\bar{\Omega}_\lambda$ with Equation (124) over t' from 0 to t

$$\begin{aligned} \rho_{m,i}^{FR}(t) &= \frac{g_{FR}}{g_{sn}^2} \rho(t) \int_0^t dt' \mathcal{B}_{m,i}(t, t'; \bar{\Omega}_\lambda(t')) f(t'), \\ f(t') &= \frac{\mathcal{L}_i}{\bar{\lambda}}(t') P_{op}(\hat{\sigma}(t')) \frac{\rho_i^{1/2}(t') \dot{\epsilon}(t')}{\rho(t') b(t')}, \end{aligned} \quad (125)$$

where $g_{FR} = (\pi/2) \tilde{g}_{FR} P_{FR}$ and we used $R_p = \mathcal{L}_i/g_{sn}$ and the approximation in Equation (116) for which $\theta(\bar{\Omega}_\lambda - 1) = 1$. From Equations (99) and (125) we obtain the time derivatives

$$\begin{aligned}\dot{\rho}_{m,i}^{FR}(t, t') &= \frac{g_{FR}}{g_{sn}^2} \rho(t) \int_0^t dt' \left[\dot{\mathcal{B}}_{m,i}(t, t'; \bar{\Omega}_\lambda(t')) + \frac{\dot{\rho}(t)}{\rho(t)} \mathcal{B}_{m,i}(t, t'; \bar{\Omega}_\lambda(t')) \right] f(t'), \\ \dot{\mathcal{B}}_m(t, t'; \bar{\Omega}_\lambda(t')) &= \frac{1}{\tau_p(t')} [2x\theta(1-x) - \delta(\bar{\Omega}_\lambda(t') - x)], \\ \dot{\mathcal{B}}_i(t, t'; \bar{\Omega}_\lambda(t')) &= \frac{1}{\tau_p(t')} [2\theta(x-1)\theta(\bar{\Omega}_\lambda(t') - x) + \delta(\bar{\Omega}_\lambda(t') - x)].\end{aligned}\quad (126)$$

Both $\rho_{m,i}^{FR}$ and $\dot{\rho}_{m,i}^{FR}$ are integrals over t' from 0 to t . The integrands depend on t and therefore must be re-calculated every time step in a numerical simulation. This can be circumvented only by resorting to an approximation. An obvious approximation is that both $\tau_p(t')$ and $\bar{\Omega}_\lambda(t')$ be replaced by their mean values on $[0, t]$

$$\begin{aligned}\tau_p(t') &\rightarrow t^{-1} \int_0^t \tau_p(t') dt', \\ \bar{\Omega}_\lambda(t') &\rightarrow t^{-1} \int_0^t \bar{\Omega}_\lambda(t') dt' = 1 + \frac{M\Omega}{t} \int_0^t s(t') dt' \equiv \bar{\Omega}_{\lambda t}(t).\end{aligned}\quad (127)$$

However, the time average of τ_p is problematic if the material is loaded, completely unloaded, and reloaded. For $R_P = l_{sn}$, $\tau_p(t') = \epsilon_p(t')/\dot{\epsilon}(t')$ where $\epsilon_p(t') = b(t')\rho_m(t')/g_{sn}\sqrt{\rho_i(t')}$, hence τ_p diverges when the material is unloaded ($\dot{\epsilon} \rightarrow 0$); $\dot{\epsilon}(t_0) = 0$. Consequently, the time average increases rapidly in a neighborhood of t_0 and is much larger than $\tau_p(t')$ for $t' > t_0$. As an alternative to the time average of τ_p we propose replacing $\tau_p(t')$ by the ratio of the time averages of ϵ_p and $\dot{\epsilon}$

$$\bar{\tau}_p(t) = \frac{\langle \epsilon_p \rangle_t}{\langle \dot{\epsilon} \rangle_t} = \frac{1}{\epsilon(t)} \int_0^t \epsilon_p(t') dt', \quad (128)$$

which does not diverge at t_0 . Numerical simulations show that $\bar{\tau}_p(t)$ is a much better approximation to $\tau_p(t')$ for $t' > t_0$ than the time average in Equation (127).

In this $\bar{\tau}_p - \bar{\Omega}$ approximation we have

$$\begin{aligned}\dot{\rho}_m^{FR}(t) &= \frac{g_{FR}}{g_{sn}^2} \rho(t) \left\{ \frac{1}{\bar{\tau}_p^2} \int_{\mathcal{R}(t-\bar{\tau}_p)}^t dt' \left[2(t-t') + \frac{\dot{\rho}(t)}{\rho(t)} (t-t')^2 \right] f(t') \right. \\ &\quad \left. - f_\theta(t - \bar{\tau}_p \bar{\Omega}) + \frac{\dot{\rho}(t)}{\rho(t)} \int_{\mathcal{R}(t-\bar{\tau}_p \bar{\Omega})}^{\mathcal{R}(t-\bar{\tau}_p)} dt' f(t') \right\}, \\ \dot{\rho}_i^{FR}(t) &= \frac{g_{FR}}{g_{sn}^2} \rho(t) \left\{ \frac{2}{\bar{\tau}_p} \int_{\mathcal{R}(t-\bar{\tau}_p \bar{\Omega})}^{\mathcal{R}(t-\bar{\tau}_p)} dt' \left[1 + \frac{\dot{\rho}(t)}{\rho(t)} (t-t') \right] f(t') + f_\theta(t - \bar{\tau}_p \bar{\Omega}) \right. \\ &\quad \left. + \frac{\dot{\rho}(t)}{\rho(t)} \left[(2\bar{\Omega} + 1) \int_0^{\mathcal{R}(t-\bar{\tau}_p \bar{\Omega})} dt' f(t') - 2 \int_0^{\mathcal{R}(t-\bar{\tau}_p)} dt' f(t') \right] \right\},\end{aligned}\quad (129)$$

where $\mathcal{R}(x) = x\theta(x)$ is the ramp function, $f(t)$ is defined in Equation (125), $\bar{\tau}_p \equiv \bar{\tau}_p(t)$, $\bar{\Omega} \equiv \bar{\Omega}_{\lambda t}(t)$, and $f_\theta(x) = f[\mathcal{R}(x)]\theta(x)$.

We now define six functions of t :

$$\begin{aligned}\{F_1(t), F_2(t), F_3(t)\} &= \int_{\mathcal{R}(t-\bar{\tau}_p)}^t dt' \{1, t', t'^2\} f(t'), \\ F_4(t) = \int_0^{\mathcal{R}(t-\bar{\tau}_p)} dt' f(t'), \quad F_5(t) &= \int_0^{\mathcal{R}(t-\bar{\tau}_p \bar{\Omega})} dt' f(t'), \quad F_6(t) = \int_{\mathcal{R}(t-\bar{\tau}_p \bar{\Omega})}^{\mathcal{R}(t-\bar{\tau}_p)} dt' t' f(t').\end{aligned}\quad (130)$$

The integro-differential Equations (129) can be replaced by eight coupled ordinary differential equations for $\rho_m(t)$, $\rho_i(t)$, and the $F_j(t)$, $j = 1, \dots, 6$:

$$\begin{aligned}
\dot{\rho}_m^{FR}(t) &= \frac{g_{FR}}{g_{sn}^2} \rho(t) \left\{ \frac{2}{\bar{\tau}_p^2} (tF_1(t) - F_2(t)) - f_\theta(t - \bar{\tau}_p \bar{\Omega}) \right. \\
&\quad \left. + \frac{\dot{\rho}(t)}{\rho(t)} \left[\frac{1}{\bar{\tau}_p^2} (t^2 F_1(t) - 2tF_2(t) + F_3(t)) + F_4(t) - F_5(t) \right] \right\}, \\
\dot{\rho}_i^{FR}(t) &= \frac{g_{FR}}{g_{sn}^2} \rho(t) \left\{ \frac{2}{\bar{\tau}_p} (F_4(t) - F_5(t)) + f_\theta(t - \bar{\tau}_p \bar{\Omega}) \right. \\
&\quad \left. + 2 \frac{\dot{\rho}(t)}{\rho(t)} \left[\left(\frac{t}{\bar{\tau}_p} - 1 \right) F_4(t) + \left(\bar{\Omega} + \frac{1}{2} - \frac{t}{\bar{\tau}_p} \right) F_5(t) - \frac{1}{\bar{\tau}_p} F_6(t) \right] \right\}, \\
\dot{F}_k(t) &= t^{k-1} f(t) - (1 - \dot{\bar{\tau}}_p) (t - \bar{\tau}_p)^{k-1} f_\theta(t - \bar{\tau}_p), \quad k = 1, 2, 3, \\
\dot{F}_4(t) &= (1 - \dot{\bar{\tau}}_p) f_\theta(t - \bar{\tau}_p), \\
\dot{F}_5(t) &= \left(1 - \dot{\bar{\tau}}_p \bar{\Omega} - \bar{\tau}_p \dot{\bar{\Omega}} \right) f_\theta(t - \bar{\tau}_p \bar{\Omega}), \\
\dot{F}_6(t) &= (t - \bar{\tau}_p) \dot{F}_4(t) - (t - \bar{\tau}_p \bar{\Omega}) \dot{F}_5(t), \tag{131}
\end{aligned}$$

where $\dot{\bar{\tau}}_p \equiv \dot{\bar{\tau}}_p(t) = t^{-1}[\tau_p(t) - \bar{\tau}_p(t)]$ and $\dot{\bar{\Omega}} \equiv \dot{\bar{\Omega}}_{\lambda t}(t) = t^{-1}[\bar{\Omega}_\lambda(t) - \bar{\Omega}_{\lambda t}(t)]$. The initial conditions on the F_i are $F_i(0) = 0$, $i = 1, \dots, 6$. Discontinuities can be trivially avoided by smearing $\theta(x)$, for example

$$\begin{aligned}
\theta(x) &\rightarrow \tilde{\theta}(x) = [1 + \exp(-x/\Delta x)]^{-1}, \\
\mathcal{R}(x) &\rightarrow x \tilde{\theta}(x), \tag{132}
\end{aligned}$$

where $\Delta x \ll 1$.

4.1.6 Initial Density of Frank-Read sources

For constant strain rate and material density, and $\epsilon < \bar{\epsilon}_p(\epsilon)$ (valid for sufficiently small strains), the set of FR equations in the $\bar{\tau}_p - \bar{\Omega}$ approximation (Equations (131)) collapse to

$$\begin{aligned}
\frac{d\rho_m^{FR}}{d\epsilon} &= \frac{2g_{FR}}{g_{sn}^2 b \bar{\epsilon}_p^2(\epsilon)} [\epsilon F_1(\epsilon, \dot{\epsilon}) - F_2(\epsilon)], \\
\frac{dF_1}{d\epsilon} &= \frac{\mathcal{L}_i}{\lambda}(\epsilon, \dot{\epsilon}) P_{op}(\epsilon, \dot{\epsilon}) \sqrt{\rho_i(\epsilon)} = f(\epsilon, \dot{\epsilon}), \\
\frac{dF_2}{d\epsilon} &= \epsilon f(\epsilon, \dot{\epsilon}), F_1(0, \dot{\epsilon}) = F_2(0, \dot{\epsilon}) = 0. \tag{133}
\end{aligned}$$

Consider constant $\dot{\epsilon}$ and $\epsilon \ll \epsilon_p$, i.e., strains sufficiently small that there are no FR pileups. In that case, $\mathcal{B}_m = (\epsilon - \epsilon')^2 / \epsilon_p^2(\epsilon')$ and we find

$$\rho_m^{FR}(\epsilon) \approx \frac{g_{FR} f(0, \dot{\epsilon})}{3g_{sn}^2 b \epsilon_p^2(0)} \epsilon^3. \tag{134}$$

The number density of FR sources is increasing linearly with ϵ and for $\epsilon \ll \epsilon_p$ the dislocation generated by each FR source is growing quadratically with ϵ ($l_m^{FR} \sim (\epsilon - \epsilon')^2$), thus the ϵ^3 increase. At these small strains the elimination of mobile dislocation via network storage, mobile-immobile annihilation, and cross-slip is linear in ϵ . An unphysical drop in the mobile dislocation density to

zero can be avoided by imposing constraints on the relative values of the $g_{\text{subscript}}$ (see Subsection 5.2) and by accounting for FR sources present in the material at $\epsilon = 0$ due to sample processing. Here we discuss how to account for the latter option, but to minimize model complexity we do not consider the most general case, that is, processing-induced FR sources both with and without pileups. We only account for FR sources formed during processing that are surrounded by multiple loops but no pileups. The processing is assumed to begin at an initial state without FR sources. The strain from the initial state will be denoted as ψ , the total processing strain is ψ_o , and strains greater than ψ_o will be symbolized, as usual, by ϵ , i.e., $\epsilon = \psi - \psi_o$. We assume that $\psi_o \lesssim 1/10$. The strain rate is denoted as $\dot{\psi}(\dot{\epsilon})$ for $\psi < \psi_o$ ($\epsilon \geq 0$). Since there are no pileups, $\psi < \bar{\psi}_p(\psi)$. The equations governing the processing-induced formation of FR sources and their subsequent evolution at strains $\psi > \psi_o$ ($\epsilon > 0$) are of the form Equation (133) with $\epsilon \rightarrow \psi$, $\dot{\epsilon} \rightarrow \dot{\psi}$, and $\bar{\epsilon}_p(\epsilon) \rightarrow \bar{\psi}_p(\psi)$. The mean pileup strain can be expressed as the sum of two terms

$$\begin{aligned}\bar{\psi}_p(\psi) &= \frac{1}{\psi} \left\{ \int_0^{\psi_o} d\psi' \psi_p(\psi') + \int_{\psi_o}^{\psi} d\psi' \psi_p(\psi') \right\} \\ &= \frac{1}{\psi} \left\{ \int_0^{\psi_o} d\psi' \psi_p(\psi') + \int_0^{\epsilon} d\epsilon' \epsilon_p(\epsilon') \right\} \\ &= (\psi_o + \epsilon)^{-1} [\psi_o \bar{\psi}_p(\psi_o) + \epsilon \bar{\epsilon}_p(\epsilon)] .\end{aligned}\tag{135}$$

The equations for the FR generation of mobile dislocation become

$$\begin{aligned}\frac{d\rho_m^{FR}}{d\epsilon} &= \frac{2g_{FR}}{g_{sn}^2 b} \left[\frac{\psi_o + \epsilon}{\psi \bar{\psi}_p(\psi_o) + \epsilon \bar{\epsilon}_p(\epsilon)} \right]^2 [(\psi_o + \epsilon) F_1(\epsilon, \dot{\epsilon}) - F_2(\epsilon)] , \\ \frac{dF_1}{d\epsilon} &= f(\epsilon, \dot{\epsilon}), \quad \frac{dF_2}{d\epsilon} = (\psi_o + \epsilon) f(\epsilon, \dot{\epsilon}).\end{aligned}\tag{136}$$

The initial conditions on $F_{1,2}$ are

$$F_1(0) = \int_0^{\psi_o} d\psi' f(\psi', \dot{\psi}), \quad F_2(0) = \int_0^{\psi_o} d\psi' \psi' f(\psi', \dot{\psi}).\tag{137}$$

Numerical dislocation density evolution calculations show that $f(\psi', \dot{\psi})$ does not vary by more than 10% from $\psi' = 0$ to $\psi' \sim 1/10$, hence $f(\psi', \dot{\psi}) \approx f(\psi_o, \dot{\psi})$. Therefore,

$$F_1(0) \approx \psi_o f(\psi_o, \dot{\psi}), \quad F_2(0) \approx \frac{1}{2} \psi_o^2 f(\psi_o, \dot{\psi}).\tag{138}$$

The sample processing that generates FR sources generally occurs at quasi-static strain rates while the mechanical testing at $\epsilon > 0$ is often carried out at much higher strain rates; here we assume that the strain rates are constant for $\psi < \psi_o$ and $\epsilon \geq 0$. Because of the change in strain rate the function f is discontinuous at $\psi = \psi_o$, i.e., $f(\psi_o, \dot{\psi}) \neq f(0, \dot{\epsilon})$. However, at immobile dislocation densities $\sim 10^{8-9} \text{ cm}^{-2}$ we have verified that $f(\psi_o, \dot{\psi}) \approx f(0, \dot{\epsilon}) \equiv f_o$. Numerical calculations also show that $\psi_p(\psi)$ is slowly varying for $\psi \lesssim 1/10$, hence

$$\bar{\psi}_p(\psi_o) \approx \psi_p(\psi_o) = \epsilon_p(\epsilon = 0) \equiv \epsilon_{po} = \frac{b}{g_{sn}} \frac{\rho_{mo}}{\sqrt{\rho_{io}}}.\tag{139}$$

Our equations governing the FR generation of mobile dislocation at constant $\dot{\epsilon}$ and material density for $\epsilon < \bar{\epsilon}_p(\epsilon)$ are given by Equation (136) with $\bar{\psi}_p(\psi_o) \rightarrow \epsilon_{po}$ and initial conditions

$$F_1(0) = \psi_o f_o, F_2(0) = \frac{1}{2} \psi_o^2 f_o, \quad (140)$$

plus the evolution equation for $\bar{\epsilon}_p(\epsilon)$:

$$\begin{aligned} \bar{\epsilon}'(\epsilon) &= [\epsilon_p(\epsilon) - \bar{\epsilon}_p(\epsilon) + \epsilon_o \epsilon_p'(0)/2] / (\epsilon + \epsilon_o), \\ \bar{\epsilon}_p(0) &= \epsilon_p(0) = \epsilon_{po}, \epsilon_o \ll 1, \end{aligned} \quad (141)$$

where $'$ in this case indicates the derivative with respect to strain.

For $\psi \in [0, \psi_o]$ the strain derivatives of $F_{1,2}(\psi, \dot{\psi})$ are $f(\psi, \dot{\psi})$ and $\psi f(\psi, \dot{\psi})$, respectively. From $f(\psi, \dot{\psi}) = f(0, \dot{\psi}) + f'(0, \dot{\psi}) \psi + \mathcal{O}(\psi^2)$ we obtain $F_1(\psi, \dot{\psi}) = f(0, \dot{\psi}) \psi + \mathcal{O}(\psi^2)$ and $F_2(\psi, \dot{\psi}) = f(0, \dot{\psi}) \psi^2/2 + \mathcal{O}(\psi^3)$; here $'$ indicates the derivative with respect to ψ . Using $\bar{\psi}_p(0) \approx \bar{\psi}_p(\psi_o) \approx \epsilon_{po}$ we have

$$\frac{\partial \rho_m^{FR}}{\partial \psi} \approx \frac{g_{FR}}{g_{sn}^2 b \epsilon_{po}^2} f(0, \dot{\psi}) \psi^2. \quad (142)$$

With the additional approximation $f(0, \dot{\psi}) \approx f(\psi_o, \dot{\psi}) \approx f(0, \dot{\epsilon}) = f_o$, integration of Equation (142) results in

$$\psi_o = \left(\frac{3 g_{sn}^2 b \epsilon_{po}^2 \rho_{mo}^{FR}}{g_{FR} f_o} \right)^{1/3} \quad (143)$$

where $\rho_{mo}^{FR} = \rho_m^{FR}(\psi_o) = \rho_m^{FR}(\epsilon = 0)$. Physically reasonable choices for ρ_{mo}^{FR} yield values of $\psi_o \lesssim 1/10$. In our comparisons of model predictions (see Section 6) to stress-strain data we use $\rho_{mo}^{FR} = 6 \times 10^8 \text{ cm}^{-2}$ which gives $\psi_o = 0.010$ at $\dot{\epsilon} = 2000 \text{ s}^{-1}$ and 298K, $\psi_o = 0.013$ at $\dot{\epsilon} = 0.001 \text{ s}^{-1}$ and 298K, and $\psi_o = 0.017$ for $\dot{\epsilon} = 2000 \text{ s}^{-1}$ and 673K.

It follows from Equation (124) that the number density of FR sources generated by the material processing is approximately

$$n_{op}^{FR}(\epsilon = 0) = \pi g_{FR} P_{op}(0, \dot{\epsilon}) \rho_{io} \psi_o / b, \quad (144)$$

where P_{op} is given by Equation (110). Since $\epsilon = 0$, $\hat{\sigma} = \sigma_y - \sigma_b$ where σ_y is the yield stress. Clearly, P_{op} and therefore the initial density of FR sources, $n_{op}^{FR}(\epsilon = 0)$, is an increasing function of the yield stress. An increase in the yield stress results in progressively smaller FR configurations becoming operative, that is, an increase in the FR source density. In contrast, 2D discrete dislocation plasticity simulations in which the sources are modeled as dislocation dipoles exhibit an increase in the yield strength as the source density is decreased (Balint, Deshpande, Needleman, and Van der Giessen, 2008), an effect that is attributed to source starvation in some cases (Xu, Balint, and Dini, 2019). While this seems like a disparity, there is agreement between these two approaches, and the key difference comes from how the overall source density is determined. In previous 2D discrete dislocation plasticity simulations (Balint et al., 2008; Xu et al., 2019), the distance between dipole sources is defined by Equation (65), which includes dependence on material parameters (which did not vary due to mass density or temperature in the previous applications) and a nucleation strength, σ_{nuc} , which has been previously taken as a Gaussian distributions defined by an average value plus the standard deviation. Certainly, with this approach higher stresses will activate more sources, which, in principle, agrees with the approach developed here. However, in these previous efforts the total source density is defined rather than calculated as in the model presented here. Thus, in the 2D discrete dislocation plasticity simulations, if the defined source density is sufficiently decreased,

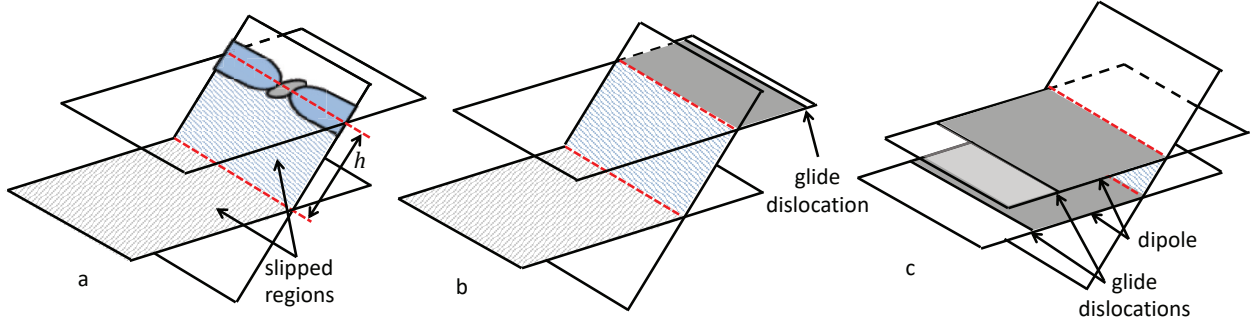


Figure 3: Double cross-slip mechanisms. Figure (a) shows the expansion of leading and trailing partial dislocations onto a second (upper) primary glide plane after gliding along the initial (lower) primary glide plane (gray hashed region) and the cross-slip plane (blue hashed region). Figure (b) shows generation via double cross-slip. In this case the dislocation cross-slipped a large enough distance, h , such that the second cross-slip event results in the bowing out and continued slip of the dislocation. Another nice schematic of this process can be found in Figure 1 of Gilman (1997). Figure (c) shows the alternate case when h is small and a dislocation dipole is formed.

there may be fewer sources active overall despite any increase in source density due to an increase in stress. In the current approach, while an initial source density is defined, the total number of sources can evolve and change during a simulation and is not limited by this initial value.

4.2 Koehler Mechanism: Dislocation Generation via Double Cross Slip

Double cross-slip for large h , the distance along the cross-slip plane between the lower and upper primary planes, can lead to the generation of a large expanding loop of mobile dislocation, while for small h an edge dislocation dipole is formed. The generation of dislocation following double cross-slip is called the Koehler mechanism (Koehler, 1952). Johnston and Gilman (1960) obtained experimental evidence for the Koehler mechanism. For large h the Koehler process generates, in addition to the large loop, a small loop comprised of two edge jogs and screw (approximately) segments on the lower and upper primary glide planes. The screw segments are attractive, which inhibits the formation of a subsequent large loop. It is assumed in this model that the large- h Koehler process generates a single large loop; in contrast, FR sources can create many loops. Another difference between Koehler and FR sources is that Koehler sources are thermally activated and FR sources are athermal.

4.2.1 Double Cross-Slip Activation Energy

Double cross slip occurs when a segment of a screw dislocation of length L_{xx} first cross-slips from the primary glide plane p to a cross-slip plane x , and then after advancing a distance h on x it cross-slips onto a glide plane p' parallel to the original primary plane (see schematics in Figure 3). Two extended segments bounded by constrictions are formed on x , and there is a single extended segment terminated by interior constrictions on p' . The maximum widths of the extended segments on x and p' are d_{ix} and d_{ip} , respectively.

The height h of the double cross-slip must be an integer multiple, n , of the distance between neighboring (close packed) primary planes along the cross-slip plane. It is a simple exercise to show that

$$h = n \frac{\sqrt{3}}{2} b. \quad (145)$$

When the first cross-slip event occurs, the energy increase is the sum of the constriction energies (one internal and one external) and the $p \rightarrow x$ dissociation energy. The extended segment with initial length L_{xx} on x extends in length by $2h$ with an associated increase in the dislocation self energy, and then cross-slips again resulting in the formation of interior constrictions on both x and p' . The $x \rightarrow p'$ dissociation energy is opposite in sign to the $p \rightarrow x$ dissociation energy, hence the net dissociation energy is zero. The configuration at the time of the second cross-slip is a kink-pair of width L_{xx} and height h in the screw dislocation. The kink-pair energy includes the self energies of the two extended segments on x and the interactions between the three finite and two semi-infinite extended segments. The double cross-slip activation energy is the sum of the constriction and kink-pair energies.

There are three contributions to the constriction energy: (1) the exterior constriction (four partials) on the primary glide plane with energy $E_p^{(c)}$ given by Equation (52); (2) the interior constriction on p' with energy given by Equation (53) for $E_i^{(c)}$ with $d_x \rightarrow d_p$; (3) two interior constrictions on the cross-slip plane, each associated with an extended segment of length h . The fault width of these segments, d_{ix} , is related to h through Equation (31) with $L_x \rightarrow h$ and $d_i \rightarrow d_{ix}$:

$$\frac{d_{ix}}{d_x} = 1 - \exp \left[-\frac{15}{32} n \ln^{-1/2} \left(\sqrt{3} \frac{d_{ix}}{b} \right) \frac{b}{d_x} \right], \quad (146)$$

where Equations (22) and (145) were used. Equation (146) was numerically solved for d_{ix}/b as a function of $d_x/b \in [1, 10]$ for $n = 1, 2, 3, 4$; larger values of n are not physically relevant, as discussed below. We found that $d_{ix}/b \leq 1$ for $n = 1, 2, 3$, and for $n = 4$ the mean value of d_{ix}/b is 1.49. Note that these small values of d_{ix} are consistent with cross-slip heights of only a few b ($h \approx 3.5b$ for $n = 4$). Since the fault widths of the segments on the cross-slip plane for $n = 1, 2, 3, 4$ are $\sim b$, the small-distance cutoff in our model, these segments will be treated as perfect (edge) dislocations; there are no dissociation or constriction energies for these segments. The double cross-slip constriction energy is equal to the sum of $E_p^{(c)}$ and $E_i^{(c)}$ with $d_x \rightarrow d_p$:

$$E_{xx}^{(c)} = 4.7 \mathcal{A} b \left(\frac{d_p}{b} - 1 \right). \quad (147)$$

We approximate the kink-pair (kp) energy as that of a kink-pair in a perfect (non-extended) screw dislocation, which is discussed in Anderson et al. (2017). Their result for the energy of the perfect kink-pair can be written

$$E_{xx}^{(kp)} = \frac{G b^2 h}{2 \pi} \tilde{w} \left(\frac{h}{L_{xx}}, \frac{L_{xx}}{b} \right), \quad (148)$$

where

$$\tilde{w}(x, y) = \frac{5}{2x} \left(\sqrt{1+x^2} - 1 \right) - 1 + \frac{1}{x} \ln \left(\frac{2}{1+\sqrt{1+x^2}} \right) + \frac{3}{2} \ln \left(\frac{xy}{x+\sqrt{1+x^2}} \right). \quad (149)$$

As for single cross-slip, we employ the approximation $L_{xx} = d_p$. The small- h expansion

$$\tilde{w}(h/d_p, d_p/b) \sim \frac{3}{2} \ln \left(\frac{h}{b} \right) - 1 - \frac{h}{2d_p} + \dots, \quad h \rightarrow 0, \quad (150)$$

shows that $E_{xx}^{(kp)}$ is negative for $h < e^{2/3} b \approx 2b$. This pathology is attributable to the inaccuracy in the self-energy of a short kink, and the unphysical 90° corners between the segments. As $h/d_p \rightarrow \infty$, \tilde{w} approaches a constant and is positive provided $L_{xx}/b = d_p/b > 2/e \approx 0.74$

$$\tilde{w}(h/d_p, d_p/b) \sim \frac{3}{2} \ln \left(\frac{e d_p}{2b} \right) - \left[\ln \left(\frac{h}{2d_p} \right) + \frac{5}{2} \right] \frac{d_p}{h} + \dots, \quad h \rightarrow \infty. \quad (151)$$

We now eliminate the unphysical negative kink-pair energies at small $x = h/d_p$ by replacing $\tilde{w}(x, d_p/b)$ with its tangent through the origin for $x \leq x_0$ where $(x_0, \tilde{w}(x_0))$ is the point of tangency:

$$\tilde{w}(x, d_p/b) \rightarrow w(x, d_p/b) = \tilde{w}(x_0, d_p/b) (x/x_0) [1 - \theta(x - x_0)] + \tilde{w}(x, d_p/b) \theta(x - x_0); \quad (152)$$

x_0 is the solution of

$$x_0 \frac{\partial \tilde{w}(x_0, d_p/b)}{\partial x_0} = \tilde{w}(x_0, d_p/b). \quad (153)$$

We next construct a Padé-like approximant for $x_0(d_p/b)$. For $d_p/b = 1$, $x_{01} \equiv x_0(1) \gg 1$, hence the large- x expansion of $\tilde{w}(x, d_p/b)$, Equation (151), can be used in Equation (153) which then assumes the simple form

$$\ln \left(\frac{x_{01}}{2} \right) - \frac{3}{4} \ln \left(\frac{e}{2} \right) x_{01} + 2 = 0; \quad (154)$$

the solution is $x_{01} = 18.37$. For $d_p/b \gtrsim 1$, we again substitute Equation (151) in Equation (153), expand to second order in $d_p/b - 1$ and $x_{01} - x_0$, solve the resulting quadratic for x_0 , and finally expand the solution to second order in $d_p/b - 1$

$$\begin{aligned} x_0(d_p/b) &= x_{01} - \frac{3c_2}{8c_1} x_{01}^2 \left[\frac{d_p}{b} - 1 - \frac{1}{4c_1^2} (2c_1^2 + 4c_1 - c_2) \left(\frac{d_p}{b} - 1 \right)^2 \right], \\ c_1 &= \ln \left(\frac{e}{2} \right) - \frac{4}{3x_{01}}, \quad c_2 = \frac{8}{3x_{01}}. \end{aligned} \quad (155)$$

Substitution of $x_{01} = 18.37$ yields

$$x_0(d_p/b) \approx 18.37 - 78 (d_p/b - 1) + 320 (d_p/b - 1)^2, \quad (156)$$

which is one-percent accurate for $d_p/b \leq 1.05$. When $d_p/b \gg 1$, in which case $x_0 \ll 1$, substitution of the small- x expansion of \tilde{w} in Equation (153) results in

$$x_0(d_p/b) = e^{5/3} \frac{b}{d_p}. \quad (157)$$

Equations (156) and (157) lead to the five-percent-accurate approximant

$$x_0(d_p/b) = \frac{18.37 - 78z + 320z^2 + 300e^{5/3}z^{7/2}/(1+z)}{1 + 300z^{7/2}}, \quad (158)$$

where $z = d_p/b - 1$.

The ratio of $x = h/d_p = \sqrt{3}nb/2d_p$ to $x_0(d_p/b)$ increases from $0.047n$ at $d_p/b = 1$ to $0.15n$ at $d_p/b = 10$, i.e. $x < x_0$ for $d_p/b \in [1, 10]$ and $n \leq 6$, hence the second term in Equation (152) vanishes for physically relevant values of d_p/b and n . Our approximation for the kink-pair energy is

$$(\mathcal{A}b)^{-1} E_{xx}^{(kp)} = 6n^2 \frac{\tilde{w}[x_0(d_p/b), d_p/b]}{(d_p/b) \cdot x_0(d_p/b)} \approx n^2 \ln \left(\frac{6}{1 + 5b/d_p} \right); \quad (159)$$

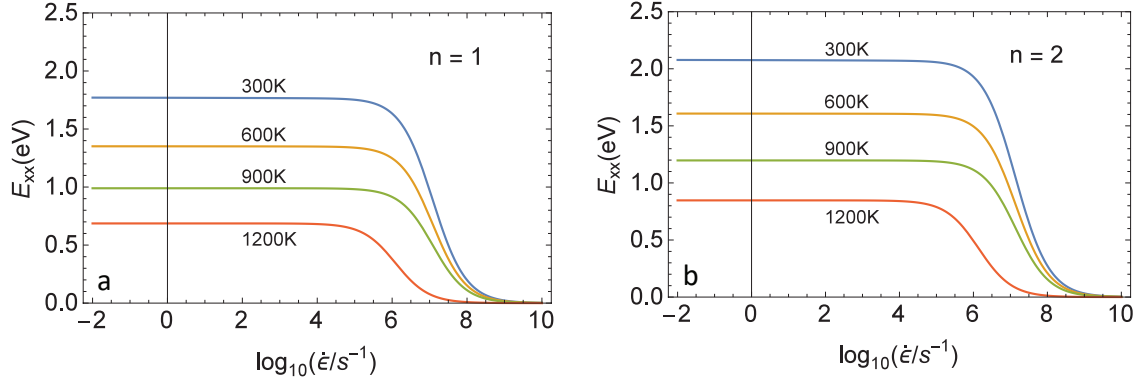


Figure 4: Double cross-slip activation energy as a function of strain rate and temperature for (a) $h = 0.22$ nm ($n = 1$) and (b) $h = 0.44$ nm ($n = 2$). For all cases $\gamma = 50$ mJ/ m².

the logarithmic approximation incurs an error $\leq 3\%$.

In double cross-slip the dissociation energy for the $x \rightarrow p'$ cross-slip is the negative of that for the $p \rightarrow x$ cross-slip, hence the net dissociation energy is zero. The double cross-slip activation energy is the sum of the constriction energy, Equation (147), and the kink-pair energy, Equation (159):

$$\begin{aligned}
 E_{xx}(\hat{\sigma}, n) &= \mathcal{A} b \left\{ 4.7 \left(\frac{d_p}{b} - 1 \right) + n^2 \ln \left(\frac{6}{1 + 5b/d_p} \right) \right\}, \\
 \frac{d_p}{b} &= \frac{\mathcal{A} + \alpha_p b^2 \hat{\sigma}}{b \gamma + \alpha_p b^2 \hat{\sigma}}.
 \end{aligned} \tag{160}$$

The double cross-slip activation energies E_{xx} of copper for $n = 1, 2$ are plotted in Figure 4 as a function of strain rate and temperature. For a discussion of the temperature dependence see Section 6. At very high shear stresses the activation energy varies as $\hat{\sigma}^{-1}$

$$E_{xx}(\hat{\sigma}, n) \sim \frac{\mathcal{A} b}{16 \pi \alpha_p} \left(4.7 + \frac{5}{6} n^2 \right) \left(1 - \frac{16 \pi \gamma}{G b} \right) \frac{G}{\hat{\sigma}}, \quad \hat{\sigma} \rightarrow \infty. \tag{161}$$

E_{xx} is the activation energy for Koehler loop formation, which is discussed in the next section.

4.2.2 Dislocation Generation by Double Cross-Slip

In Section 4.1, we concluded that grain boundary pileups can be neglected in grains with diameters greater than or of order 10 μm because of annihilation and storage mechanisms. Here we likewise neglect the potential impact of grain boundaries on dislocation generation by the Koehler mechanism.

The potential number of double cross-slip sites per unit volume is proportional to ρ_m/L_x , and the rate at which sites become thermally activated is, in the Arrhenius approximation, proportional to $\bar{\nu} \exp(-E_{xx}/k_B T)$. The rate of thermally-activated formation of double cross-slip sites per unit volume at time t' is

$$\dot{n}_{xx}(t') = \tilde{g}_{xx} \bar{\nu} \frac{\rho_m(t')}{L_{xx}(t')} \exp \left\{ -E_{xx}(\hat{\sigma}(t'), n) / k_B T(t') \right\}, \tag{162}$$

where the activation energy for double cross-slip, $E_{xx}(\hat{\sigma}, n)$, is given by Equation (160). Again we approximate L_{xx} by d_p , the fault width on the primary glide plane. The number of double-cross-slip sites formed during $(t', t' + dt')$ per unit t -volume (current volume) is (see also Equation (124))

$$\dot{n}_{xx}(t, t') dt' = \frac{\rho(t)}{\rho(t')} \dot{n}_{xx}(t') dt' = \tilde{g}_{xx} \bar{\nu} \frac{\rho_m(t')}{d_p(t')} \exp \left\{ -E_{xx}(\hat{\sigma}(t'), n) / k_B T(t') \right\} \frac{\rho(t)}{\rho(t')} dt'. \quad (163)$$

We now focus on the Koehler mechanism for large h , that is, $n > 1$ for which loops are formed. The total length at time t of a Koehler loop formed at time $t' \leq t$ is

$$l_m^{xx}(t, t') = 2 \pi r(t, t'). \quad (164)$$

We approximate the expansion velocity of a t' loop as equal to the mean dislocation velocity at time t' , as was done for FR sources (see Equation (72))

$$r(t'', t') = v(t') (t'' - t') = (t'' - t') \frac{\dot{\epsilon}(t')}{b(t') \rho_m(t')}; \quad (165)$$

the Burgers vector is time-dependent under dynamic loading conditions, in particular under shock wave loading, where the material compression can be large. The density of Koehler-generated dislocation at time t is

$$\begin{aligned} \rho_m^{xx}(t) &= \int_0^t dt' l_m^{xx}(t, t') \dot{n}_{xx}(t, t') \\ &= g_{xx} \bar{\nu} \rho(t) \int_0^t dt' (t - t') \frac{\dot{\epsilon}(t')}{\rho(t') b(t') d_p(t')} \exp \left\{ -\frac{E_{xx}(\hat{\sigma}(t'), n)}{k_B T(t')} \right\}, \end{aligned} \quad (166)$$

where $g_{xx} = 2\pi \tilde{g}_{xx}$. The time derivative is given by

$$\dot{\rho}_m^{xx}(t) = g_{xx} \bar{\nu} \int_0^t dt' \frac{\partial}{\partial t} [\rho(t) (t - t')] \frac{\dot{\epsilon}(t')}{\rho(t') b(t') d_p(t')} \exp \left\{ -\frac{E_{xx}(\hat{\sigma}(t'), n)}{k_B T(t')} \right\}. \quad (167)$$

Equation (167) renders the evolution equations integro-differential. This can be circumvented by defining the function

$$F^{xx}(t) = \int_0^t dt' (t - t') \frac{\rho_0 \dot{\epsilon}(t')}{\rho(t') b(t') d_p(t')} \exp \left\{ -\frac{E_{xx}(\hat{\sigma}(t'), n)}{k_B T(t')} \right\}, \quad (168)$$

hence

$$\begin{aligned} \dot{\rho}_m^{xx}(t) &= g_{xx} \bar{\nu} \frac{\rho(t)}{\rho_0} \left\{ \dot{F}^{xx}(t) + \frac{\dot{\rho}(t)}{\rho(t)} F^{xx}(t) \right\}, \\ \ddot{F}^{xx}(t) &= \frac{\rho_0}{\rho(t)} \frac{\dot{\epsilon}(t)}{b(t) d_p(t)} \exp \left\{ -\frac{E_{xx}(\hat{\sigma}(t), n)}{k_B T(t)} \right\}; \end{aligned} \quad (169)$$

the initial conditions on F^{xx} and its time derivative are $F^{xx}(0) = \dot{F}^{xx}(0) = 0$.

When the double cross-slip height is small, $n = 1$, a pair of edge dipoles is generated. As the dipoles extend toward the grain boundary, only immobile dislocation is being generated; the length of mobile dislocation throughout this process is essentially unchanged (see Figure 1 in Gilman (1997)). The rate of formation of Koehler edge dipoles per unit volume is given by Equation (163)

for $n = 1$. Assuming that the leading edges of the dipoles are moving at the mean dislocation speed, the length at time t of the two dipoles formed at $t' \leq t$ is

$$l_i^{dipole}(t, t') = 4 \int_{t'}^t dt'' v(t'') = 4 r(t, t'). \quad (170)$$

The factor of four accounts for the two dislocations in each of the two dipoles. The density of immobile dislocation generated by all Koehler dipole sources up to time t is given by

$$\begin{aligned} \rho_i^{xx}(t) &= \int_0^t dt' l_i^{dipole}(t, t') \dot{n}_{xx}^{dipole}(t, t') \\ &= \frac{2}{\pi} g_{xx} \bar{\nu} \rho(t) \int_0^t dt' (t - t') \frac{\dot{\epsilon}(t')}{\rho(t') b(t') d_p(t')} \exp \left\{ -\frac{E_{xx}(\hat{\sigma}(t'), 1)}{k_B T(t')} \right\}, \end{aligned} \quad (171)$$

Note that this is of the same form as Equation (166) but with $n = 1$ and $g_{xx} \rightarrow (2/\pi)g_{xx}$; the time derivative is trivially obtained from Equations (167) and (169).

4.3 Grain Boundary Nucleation of Mobile Dislocation

Mobile dislocation nucleation on the grain boundaries is presumably not an activated process, and is certainly independent of the network density. Intuitively, the rate increases with the applied stress – we assume proportionality – and is proportional to the plastic strain rate, which sets the time scale for athermal processes. Therefore the nucleation rate is proportional to the rate at which plastic work is being done. However, it is only the work done within a narrow boundary layer that can result in the generation of dislocation along the grain boundary. If we assume that the layer thickness is of order b then the rate at which mobile dislocation is generated in any grain is proportional to

$$\frac{\hat{\sigma} \dot{\epsilon} D^2 b}{G b^2}; \quad (172)$$

the numerator is proportional to the energy per unit time going into the boundary layer, and the denominator is proportional to the energy per unit length of the dislocation. Dividing by the grain volume gives the rate of mobile dislocation density generation by the grain boundaries

$$\dot{\rho}_m^{\partial} = g_{\partial} \frac{\hat{\sigma} \dot{\epsilon}}{G b D}. \quad (173)$$

This vanishes as $D \rightarrow \infty$, as it should.

4.4 Shock Wave Generation of Dislocation

Dislocation generation, evolution, and active mechanisms induced by shock waves has been investigated both experimentally and theoretically for about four decades, but a full understanding of the process still eludes us (Agarwal, Valisetty, and Dongare, 2020; Turneaure, Renganathan, Winey, and Gupta, 2018; Fan et al., 2021; Sharma, Turneaure, Winey, Rigg, Sinclair, Wang, Toyoda, and Gupta, 2020). We begin with brief summaries of several representative studies (although this is not a comprehensive review), then present our new model of shock-generated dislocation, and conclude with a discussion of the weak-shock limit of our model.

One of the earliest studies of shock-generated dislocation was that of Murr and Kuhlmann-Wilsdorf (1978) (MKW). They measured dislocation density and dislocation cell sizes in nickel

shock loaded to pressures from 8 GPa to 46 GPa. They found that the square root of the dislocation density, ρ_d , is proportional to the shock pressure, P_H , scaled by the shear modulus

$$\frac{P_H}{G(P_H)} = 0.007 \mu m \sqrt{\rho_d}. \quad (174)$$

Below we show that our new model is of the same form in the weak shock limit.

In his excellent book on materials dynamics, Meyers (1994) considers shock wave generation of dislocation. He tells us that dislocations are nucleated at the shock front by shear stresses and then move a short distance at sub-sonic speeds. He points out that pre-existing dislocations might relax part of the deviatoric stress in the shock, thereby reducing the amount of dislocation generated by the shock. He states that “dislocation density is not significantly altered by grain size” (Braga, Kestenbach, and Meyers, 1978). We have accordingly not accounted for the grain structure in our new model.

Podurets, Tkachenko, Ignatova, Lebedev, Igonin, and Raevsky (2013) determined dislocation densities in shock-loaded copper and tantalum from analyses of X-ray diffraction data. The dislocation density in copper was found to first increase with shock pressure, reach a maximum in the pressure range 30-40 GPa, and then decrease. It is suggested that the drop in density at high pressures is attributable to partial annealing at the higher temperatures in the stronger shocks. In contrast to copper, the density in tantalum increases monotonically with pressure. In both metals the dislocation density increases with the mean grain size, in disagreement with the findings of Braga et al. (1978).

Pang, Jones, Chiu, Millett, Whiteman, and Bourne (2014) investigated the orientation dependence of shock-generated dislocation in single-crystal tantalum. The dislocation density in their as-received tantalum was about $6 \times 10^8 \text{ cm}^{-2}$. After shock loading to 6.2 GPa the densities were $6 \times 10^{10} \text{ cm}^{-2}$ along [111], $4 \times 10^{10} \text{ cm}^{-2}$ along [011], and $2 \times 10^{10} \text{ cm}^{-2}$ along [001]. The dislocation densities increased by factors of 30-100 in a modest 62 kbar shock.

Austin and McDowell (2012) (AM) recently constructed a model of homogeneous dislocation nucleation by shocks. They comment that “the rise in shear stress behind the leading edge of a shock front serves as the driving force for dislocation generation and migration”. The nucleation is modeled as thermally-activated with an activation energy of the form $\Delta g = c G b^3 (1 - \tau/\tau_{hom})$ where $c \sim 1/10$, τ is the shear stress, and $\tau_{hom} \sim G/15$ is an athermal nucleation stress. We now estimate the ratio $\Delta g/k_B T$ for copper as a function of P_H , the Hugoniot (shock state) pressure. The ratio is evaluated at $P_{1/2}$, which is the pressure at the point on the shock path where the plastic strain attains one-half of its final (Hugoniot) value. The material density, the ratio τ/G ($2\tau =$ flow stress), and the temperature at $P_{1/2}$ as a function of P_H were obtained from Tonks (1993): $1 - \rho_0/\rho_{1/2} \approx 0.32 P_H - 0.1 P_H^2$, $\tau_{1/2}/G_{1/2} \approx 0.073 P_H - 0.018 P_H^2$, and $T_{1/2} \approx 293 + 250 P_H + 1000 P_H^2$. The shear modulus of copper as a function of density and temperature is given in Burakovsky, Greeff, and Preston (2003), and $b^3 = b_0^3 \rho_0/\rho$ with $b_0 = 0.255 \text{ nm}$ and $\rho_0 = 8.93 \text{ g cm}^{-3}$. We find $\Delta g_{1/2}/k_B T_{1/2} = 27.6 - 52.4 P_H + 33.5 P_H^2 - 7.24 P_H^3$ for $P_H \geq 0.2 \text{ Mbar}$, which decreases monotonically with P_H until it vanishes at about 1.4 Mbar. The Van’t Hoff-Arrhenius equation relating the nucleation rate to $\Delta g/k_B T$ is valid only when the activation energy, Δg , is much greater than the thermal energy: $\Delta g/k_B T \gg 1$ (Chandrasekhar, 1943; Hänggi, Talkner, and Borkovec, 1990; Hunter and Preston, 2015). In the AM model, $\Delta g/k_B T = 4.8, 3.5, 2.4,$ and 1.6 at shock pressures of 70, 80, 90, and 100 GPa in copper, hence the model rapidly loses fidelity as the shock pressure approaches 1 Mbar. In general, the AM model, based as it is on Van’t Hoff-Arrhenius thermal activation, is inapplicable at shock pressures of order 1 Mbar and higher. In contrast, our model is applicable to overdriven (megabar) shocks.

We now describe our model of shock-generated dislocation. We assume a steady shock wave, therefore the stress vs. material density of the shock process (compression path) is along the Rayleigh line

$$\sigma_n = \rho_0 u_s^2 \mu, \quad (175)$$

where σ_n is the normal compressive stress, u_s is the constant shock velocity, and $\mu = 1 - \rho_0/\rho$. Neglecting shear stresses we have $\sigma_n = P$. We assume a linear $u_s - u_p$ (u_p is the particle/material velocity) Hugoniot

$$u_s = c_0 + s u_p. \quad (176)$$

Mass conservation for a steady shock wave reads

$$u_p = u_s \mu_H, \quad (177)$$

where μ_H is the compression on the Hugoniot. Equations (175), (176), and (177) express the Rayleigh line as

$$P = \rho_0 c_0^2 \frac{\mu}{(1 - s \mu_H)^2}. \quad (178)$$

In uniaxial compression the incremental energy per unit mass is $dE = dW + dQ$ where

$$dW = -P dV = P \frac{d\rho}{\rho^2} \quad (179)$$

is the differential center-of-mass work done on unit mass of the material by the shock, and dQ is the incremental heat transferred to the material per unit mass. Since heat flow does not generate dislocation, we conclude that the energy required to form dislocation is provided by the work W . We make the reasonable assumption that a fixed fraction, $\xi \ll 1$, of the work goes into creating dislocation. An increment in the dislocation density along the Rayleigh line is equal to the incremental energy per unit volume going into dislocation, $\xi \rho dW$, divided by the energy per unit length of dislocation ($\sim G b^2$)

$$\frac{d\rho_{m,i}^{sh}}{dt} = g_{m,i}^{sh} \frac{P(\rho(t))}{G(\rho(t), T(t)) b^2(t)} \frac{\dot{\rho}(t)}{\rho(t)}, \quad (180)$$

where $P(\rho(t))$ is given by Equation (178), $b(t) = b_0 (\rho_0/\rho(t))^{1/3}$, and the $g_{m,i}^{sh}$ are dimensionless.

The dislocation generation rate Equation (180) can be expressed in terms of P , P_H , and \dot{P} using the relations

$$\begin{aligned} \frac{\dot{\rho}}{\rho} &= \frac{\dot{\mu}}{1 - \mu} = \frac{\dot{P}}{\rho_0 u_s^2 - P}, \\ \rho_0 u_s^2 &= \frac{P_H}{\mu_H} = \frac{2 s^2 P_H^2}{\rho_0 c_0^2 + 2 s P_H - \sqrt{\rho_0 c_0^2 (\rho_0 c_0^2 + 4 s P_H)}}. \end{aligned} \quad (181)$$

Equation (180) simplifies considerably for weak shocks. In this case, we can neglect the temperature dependence of G and expand it to lowest order in P

$$G(P) = G_0 + G'_0 P. \quad (182)$$

For weak shocks, $u_s \approx c_0$, hence $\rho_0 u_s^2 \approx \rho_0 c_0^2 = B_0 + (4/3) G_0$. Since $P \ll \rho_0 u_s^2$, Equation (181) gives $\dot{\rho}/\rho \approx \dot{P}/(B_0 + (4/3) G_0)$. With the approximations $B_0 \approx 3 G_0$ and $b \approx b_0$, Equation (180) for weak shocks can be integrated with the result

$$\rho_{m,i}^{sh} = \frac{g_{m,i}^{sh}}{4 G_0 b_0^2} \int_0^{P_H} \frac{P dP}{G_0 + G'_0 P} = g_{m,i}^{sh} \frac{P_H^2}{8 b_0^2 G_0 G_H} f\left(\frac{G'_0 P_H}{G_0}\right), \quad (183)$$

where

$$f(z) = 2 \left(1 + \frac{1}{z}\right) \left[1 - \frac{\ln(1+z)}{z}\right]. \quad (184)$$

For G'_0 of order unity (typical) and $P_H < G_0$ (weak shocks), $0 < z < 1$ and $f(z) \approx 1$. We then obtain

$$\frac{P_H}{\sqrt{G_0 G_H}} = \left(\frac{8}{g_{m,i}^{sh}}\right)^{1/2} b_0 \sqrt{\rho_{m,i}^{sh}}, \quad (185)$$

which is essentially of the same form as Equation (174) obtained by MKW. For nickel, with $b_0 = 2.49 \times 10^{-8}$ cm, the coefficient equals $0.007 \mu\text{m}$ (MKW) for $g^{sh} = 0.01$.

5 Dislocation Density Evolution Equations

The two integro-differential evolution equations describe changes in the mobile and network dislocation densities due to material density variations, several elementary dislocation mechanisms – network and grain boundary storage, mobile-mobile and mobile-immobile annihilation, single cross-slip and screw-screw annihilation, the Koehler mechanism, grain boundary nucleation, FR sources – and shock wave generation.

The evolution of the immobile dislocation density is described by the following equation,

$$\begin{aligned} \frac{d\rho_i}{dt} &= \frac{2}{3} \frac{\dot{\rho}}{\rho} \rho_i + (g_{sn} - g_{ami}) \frac{1}{b} \sqrt{\rho_i} \dot{\epsilon} + g_{s\partial} \frac{\dot{\epsilon}}{bD} - g_{ax} \frac{h_c}{b} \rho_i \dot{\epsilon} - g_{tx} \bar{\nu} \rho_m \exp\left[-\frac{E_x(\hat{\sigma})}{k_B T}\right] \\ &+ \frac{2}{\pi} g_{xx} \bar{\nu} \int_0^t dt' \frac{\partial}{\partial t} [\rho(t)(t-t')] \frac{\dot{\epsilon}(t')}{\rho(t') b(t') d_p(t')} \exp\left\{-\frac{E_{xx}(\hat{\sigma}(t'), 1)}{k_B T(t')}\right\} \\ &+ \frac{g_{FR}}{g_{sn}^2} \rho(t) \int_0^t dt' \left[\dot{\mathcal{B}}_i(x(t, t'), \bar{\Omega}_\lambda(t')) + \frac{\dot{\rho}(t')}{\rho(t')} \mathcal{B}_i(x(t, t'), \bar{\Omega}_\lambda(t')) \right] f(t') \\ &+ g_i^{sh} \frac{P(\rho)}{G(\rho, T)} \frac{\dot{\rho}}{b^2 \rho}, \end{aligned} \quad (186)$$

and the mobile dislocation density evolves according to

$$\begin{aligned} \frac{d\rho_m}{dt} &= \frac{2}{3} \frac{\dot{\rho}}{\rho} \rho_m - (g_{sn} + g_{ami}) \frac{1}{b} \sqrt{\rho_i} \dot{\epsilon} - g_{amm} \frac{1}{b} \sqrt{\rho_m} \dot{\epsilon} + \left(g_{\partial} \frac{\dot{\sigma}}{G(\rho, T)} - g_{s\partial}\right) \frac{\dot{\epsilon}}{bD} \\ &- g_{ax} \frac{h_c}{b} \rho_i \dot{\epsilon} - g_{tx} \bar{\nu} \rho_m \exp\left[-\frac{E_x(\hat{\sigma})}{k_B T}\right] \\ &+ g_{xx} \bar{\nu} \int_0^t dt' \frac{\partial}{\partial t} [\rho(t)(t-t')] \frac{\dot{\epsilon}(t')}{\rho(t') b(t') d_p(t')} \exp\left\{-\frac{E_{xx}(\hat{\sigma}(t'), n)}{k_B T(t')}\right\} \\ &+ \frac{g_{FR}}{g_{sn}^2} \rho(t) \int_0^t dt' \left[\dot{\mathcal{B}}_m(x(t, t'), \bar{\Omega}_\lambda(t')) + \frac{\dot{\rho}(t')}{\rho(t')} \mathcal{B}_m(x(t, t'), \bar{\Omega}_\lambda(t')) \right] f(t') \\ &+ g_m^{sh} \frac{P(\rho)}{G(\rho, T)} \frac{\dot{\rho}}{b^2 \rho}. \end{aligned} \quad (187)$$

Although not always explicitly indicated, all of the quantities ρ , ρ_i , ρ_m , T , $\dot{\epsilon}$, $\hat{\sigma}$, and D (mean grain diameter) are time dependent; we neglect the material density dependence of the mean phonon frequency, $\bar{\nu}$. The functions $\mathcal{B}_{i,m}$ and their time derivatives are given by Equations (99) and (126), Ω is defined in Equation (96), and $f(t')$ is defined in Equation (125). The single and double cross-slip activation energies, E_x and E_{xx} , as well as $d_p(t') \equiv d_p(\rho(t'), \hat{\sigma}(t'))$, are given by

Equations (56) and (160) (with some adjustment as discussed later in Section 6). $G(\rho, T)$ is the density- and temperature-dependent shear modulus (Burakovsky et al., 2003), and h_c is the distance within which opposite-signed screw dislocations spontaneously cross-slip and annihilate. The eleven $g_{\text{subscript}}$ are dimensionless coupling constants specific to the various dislocation mechanisms:

- g_{sn} : storage in the network (forest) of immobile dislocation;
- g_{ami} : mobile-immobile annihilation;
- g_{amm} : mobile-mobile annihilation;
- $g_{s\partial}$: storage on the grain boundaries;
- g_{∂} : grain boundary nucleation;
- g_{ax} : spontaneous (athermal) cross-slip and screw-screw annihilation;
- g_{tx} : thermally activated cross-slip and screw-screw annihilation;
- g_{xx} : double cross-slip with Koehler multiplication, including dipole formation.
- g_{FR} : Frank-Read sources;
- $g_{m,i}^{sh}$: shock wave generation of mobile and immobile dislocation.

More details about relationships between the $g_{\text{subscript}}$ parameters, and limits of the values are discussed later in Section 5.2.

A few comments regarding the thermal activation terms in the evolution equations are in order. In the evolution equations for constant strain rate ($t \rightarrow \epsilon$), the generic dependence of the single and double cross-slip terms on temperature and strain rate is $\exp(-E/k_B T)/\dot{\epsilon}$, thus high strain rate and low temperature are equivalent limits in that the thermal activation terms are suppressed in either case, and likewise these contributions are enhanced at low strain rates or high temperatures (Wang, Beyerlein, and LeSar, 2007).

5.1 Constant Material Density and Strain Rate

When the material density and strain rate are nearly constant, which is the case for stress-strain curves measured in the laboratory, Equations (186) and (187) simplify. The independent variable in the evolution equations is conveniently changed from the time, t , to the plastic strain, $\epsilon = \dot{\epsilon}t$. The dislocation density evolution equations for constant material density and strain rate are

$$\begin{aligned}
\frac{d\rho_i}{d\epsilon} &= (g_{sn} - g_{ami}) \frac{1}{b} \sqrt{\rho_i} + g_{s\partial} \frac{1}{bD} - g_{ax} \frac{h_c}{b} \rho_i - g_{tx} \frac{\bar{\nu}}{\dot{\epsilon}} \rho_m \exp \left[-\frac{E_x(\hat{\sigma})}{k_B T} \right] \\
&+ \frac{2}{\pi} g_{xx} \frac{\bar{\nu}}{\dot{\epsilon}} \frac{1}{b} \int_0^\epsilon d\epsilon' \frac{1}{d_p(\epsilon')} \exp \left[-\frac{E_{xx}(\hat{\sigma}(\epsilon'), 1)}{k_B T(\epsilon')} \right] \\
&+ \frac{g_{FR}}{g_{sn}^2} \frac{1}{b} \int_0^\epsilon d\epsilon' \frac{\partial}{\partial \epsilon} \mathcal{B}_i(x(\epsilon, \epsilon'), \bar{\Omega}_\lambda(\epsilon')) \frac{\mathcal{L}_i}{\lambda}(\epsilon') P_{op}(\hat{\sigma}(\epsilon') \rho_i^{1/2}(\epsilon')), \tag{188}
\end{aligned}$$

$$\begin{aligned}
\frac{d\rho_m}{d\epsilon} &= -(g_{sn} + g_{ami}) \frac{1}{b} \sqrt{\rho_i} - g_{amm} \frac{1}{b} \sqrt{\rho_m} + \left(g_{\partial} \frac{\hat{\sigma}}{G(\rho, T)} - g_{s\partial} \right) \frac{1}{bD} \\
&- g_{ax} \frac{h_c}{b} \rho_i - g_{tx} \frac{\bar{\nu}}{\dot{\epsilon}} \rho_m \exp \left[-\frac{E_x(\hat{\sigma})}{k_B T} \right] \\
&+ g_{xx} \frac{\bar{\nu}}{\dot{\epsilon}} \frac{1}{b} \int_0^\epsilon d\epsilon' \frac{1}{d_p(\epsilon')} \exp \left[-\frac{E_{xx}(\hat{\sigma}(\epsilon'), n)}{k_B T(\epsilon')} \right] \\
&+ \frac{g_{FR}}{g_{sn}^2} \frac{1}{b} \int_0^\epsilon d\epsilon' \frac{\partial}{\partial \epsilon} \mathcal{B}_m(x(\epsilon, \epsilon'), \bar{\Omega}_\lambda(\epsilon')) \frac{\mathcal{L}_i}{\lambda}(\epsilon') P_{op}(\hat{\sigma}(\epsilon') \rho_i^{1/2}(\epsilon')). \tag{189}
\end{aligned}$$

5.2 Parameter Relationships

In this subsection, we obtain constraints on the relative values of g_{sn} , g_{ami} , and g_{FR} . Since these parameters are independent of T , ρ , $\dot{\epsilon}$, and D , we consider constant ρ and $\dot{\epsilon}$, sufficiently low T that thermally-activated cross-slip is negligible, and $D \rightarrow \infty$ (i.e., a single crystal). In addition, we assume $\epsilon < \epsilon_p(\dot{\epsilon})$, i.e., strains small enough that there are no FR pileups hence no generation of immobile dislocation by FR sources. The immobile dislocation density then evolves according to

$$\frac{d\rho_i}{d\epsilon} = (g_{sn} - g_{ami}) \frac{1}{b} \sqrt{\rho_i} - g_{ax} \frac{h_c}{b} \rho_i. \quad (190)$$

The solution of this ODE is given in Appendix D. For $C_1 = 0$, i.e., $D \rightarrow \infty$, we have

$$\sqrt{\rho_i(\epsilon)} = \sqrt{\rho_{i\infty}} - (\sqrt{\rho_{i\infty}} - \sqrt{\rho_{io}}) \exp(-\epsilon/\epsilon_c), \quad (191)$$

where

$$\begin{aligned} \sqrt{\rho_{i\infty}} &= \frac{g_{sn} - g_{ami}}{4b g_{ax}}, \\ \epsilon_c &= 1/2g_{ax}; \end{aligned} \quad (192)$$

we used $h_c = 4b$ in Equation (192). The quantity $\rho_{i\infty}$ is the saturation (large strain) immobile density. Clearly we must require $g_{sn} > g_{ami}$.

Since our focus here is small strains, we expand $\sqrt{\rho_i(\epsilon)}$ to second order in ϵ

$$\begin{aligned} \sqrt{\rho_i(\epsilon)} &= \sqrt{\rho_{io}} \left[1 + \left(\sqrt{\frac{\rho_{i\infty}}{\rho_{io}}} - 1 \right) \left(\frac{\epsilon}{\epsilon_c} - \frac{\epsilon^2}{2\epsilon_c^2} + \dots \right) \right] \\ &\approx \sqrt{\rho_{io}} \left[1 + \sqrt{\frac{\rho_{i\infty}}{\rho_{io}}} \left(\frac{\epsilon}{\epsilon_c} - \frac{\epsilon^2}{2\epsilon_c^2} \right) \right]. \end{aligned} \quad (193)$$

Neglecting mobile-mobile annihilation ($g_{amm} = 0$) and athermal cross-slip ($\rho_{io} \ll b^{-2} \sim 10^{15} \text{ cm}^{-2}$), the mobile density evolution is governed by (see Equations (189) and (133))

$$\begin{aligned} \frac{d\rho_m}{d\epsilon} &= -(g_{sn} + g_{ami}) \frac{1}{b} \sqrt{\rho_i} - g_{ax} \frac{h_c}{b} \rho_i + \frac{2g_{FR}}{g_{sn}^2 b \bar{\epsilon}^2(\epsilon)} [\epsilon F_1(\epsilon, \dot{\epsilon}) - F_2(\epsilon, \dot{\epsilon})], \\ \frac{dF_1}{d\epsilon} &= f(\epsilon, \dot{\epsilon}), \quad \frac{dF_2}{d\epsilon} = \epsilon f(\epsilon, \dot{\epsilon}), \\ f(\epsilon, \dot{\epsilon}) &= \frac{\mathcal{L}_i}{\lambda}(\epsilon, \dot{\epsilon}) P_{op}(\epsilon, \dot{\epsilon}) \sqrt{\rho_i(\epsilon)}. \end{aligned} \quad (194)$$

We drop the explicit dependence of f on $\dot{\epsilon}$ and expand in ϵ

$$f(\epsilon) = f_o + f'_o \epsilon + \dots \quad (195)$$

It follows that

$$\frac{d\rho_m^{FR}}{d\epsilon} \approx \frac{g_{FR} f_o}{g_{sn}^2 b \bar{\epsilon}_{po}^2} = g_{FR} \frac{f_o \rho_{io}}{b^3 \rho_{mo}^2} \epsilon^2. \quad (196)$$

We find that the second-order term in the expansion of $\sqrt{\rho_i(\epsilon)}$, Equation (193), is much smaller than the FR term for $g_{FR} \gtrsim 10^{-3}$ and realistic values of g_{sn} , g_{ami} , and initial dislocation densities. Therefore,

$$\begin{aligned}\rho'_m &\equiv \frac{d\rho_m}{d\epsilon} \approx -(g_{sn} + g_{ami}) \frac{\sqrt{\rho_{io}}}{b} \left(1 + \frac{g_{sn} - g_{ami}}{2b\sqrt{\rho_{io}}} \epsilon - g_{FR} \frac{f_o \rho_{io}^{1/2}}{(g_{sn} + g_{ami}) b^2 \rho_{mo}^2} \epsilon^2 \right), \\ &\equiv \rho'_{mo} (1 + \alpha \epsilon - \beta \epsilon^2).\end{aligned}\quad (197)$$

The initial decrease in the mobile density due to storage and annihilation is offset by FR generation with increasing strain. However if g_{FR} is too small then ρ_m can drop to zero. We now calculate the minimum value of g_{FR} to ensure that $\rho_m(\epsilon) > 0$.

The minimum of ρ_m occurs at ϵ_o , $\rho'_m(\epsilon_o) = 0$. From Equation (197) we obtain

$$\begin{aligned}\epsilon_o &= (\alpha + \sqrt{\alpha^2 + 4\beta})/2\beta, \\ \rho_m(\epsilon_o) &= \rho_{mo} - \frac{1}{6} |\rho'_{mo}| \epsilon_o (\alpha \epsilon_o + 4).\end{aligned}\quad (198)$$

The maximum value of ϵ_o corresponds to $\rho_m = 0$

$$\begin{aligned}max \epsilon_o &= (\sqrt{k\alpha + 4} - 2) / \alpha, \\ k &= 6\rho_{mo} / |\rho'_{mo}|.\end{aligned}\quad (199)$$

The minimum value of $\beta \sim g_{FR}$ corresponds to $max \epsilon_o$ and yields the minimum g_{FR} for which $\rho_m(\epsilon) > 0$.

$$min \beta = \alpha^2 \frac{\sqrt{k\alpha + 4} - 1}{(\sqrt{k\alpha + 4} - 2)^2} \approx \frac{8\alpha^2}{k\alpha - 1}.\quad (200)$$

This approximation is accurate to 10% or better for $2 < k\alpha < 20$. Finally, we obtain

$$g_{FR} > \frac{2(g_{sn} + g_{ami})(g_{sn}^2 - g_{ami}^2)\rho_{mo}^2}{\left(3 \frac{g_{sn} - g_{ami}}{g_{sn} + g_{ami}} \frac{\rho_{mo}}{\rho_{io}} - 1\right) f_o \rho_{io}^{3/2}}.\quad (201)$$

5.3 Modeling the Back Stress

In this subsection we describe the back stress model used to calculate the effective applied stress, $\hat{\sigma}$, which was previously defined as the difference between the applied von Mises stress, σ , and the back stress, σ_b . While development of a back stress model is not a primary focus of the current work, it is an important feature of the model and is utilized both in the dislocation density evolution equations derived here, and in the kinetic equation presented previously in (Hunter and Preston, 2015). Specifically, we highlight here that the back stress model employed in this work is of a similar functional form, but different from the model used in the original kinetic equation publication. Previously, the back stress was defined as $\sigma_b = g_b b G \sqrt{\rho_i}$ (Hunter and Preston, 2015). This equation was derived from the equation first presented in 1955 by A. Seeger, who proposed that the internal or back stress opposing the glide of mobile dislocations is

$$\sigma_b = \alpha b G(\rho, T) \sqrt{N}, \quad (202)$$

where $\alpha \approx 1/5$ and N is the density of dislocations that are parallel to the mobile dislocation with the same Burgers vector (Seeger, 1955). We again start from this equation to develop a modified form of the back stress model. Here, however, we assume that N is proportional to the total dislocation density, $\rho_d = \rho_i + \rho_m$, rather than only the immobile dislocation density. Equation (202) may then be written as

$$\sigma_b = \alpha b G(\rho, T) \frac{b}{\mathcal{L}}, \quad (203)$$

where $\mathcal{L} = \rho_d^{-1/2}$ is the mean dislocation spacing. About a decade later, Kocks argued that the back stress is indeed of the form shown in Equation (203) but that in general \mathcal{L} is replaced by l which is “the average dislocation (or group) spacing” (Kocks, 1967). In modern parlance the “group spacing” is a mesoscopic length scale associated with dislocation patterning, e.g. deformation-induced dislocation cell structures (Hähner, Bay, and Zaiser, 1998). We now make the reasonable assumption that l increases nonlinearly with the mean dislocation spacing

$$\frac{l}{b} = c \left(\frac{\mathcal{L}}{b} \right)^{n_b}, \quad (204)$$

where $n_b \sim \mathcal{O}(1)$. It is worth mentioning that the Taylor equation, i.e., $\sigma \sim \sqrt{\rho_d}$, and the assumption of similitude (Ortiz and Repetto, 1999) imply $n_b = 1$ for dislocation cell formation. However, corrections to $\sigma \sim \sqrt{\rho_d}$ and departures from similitude would result in deviations of n_b from unity, thus we take $n_b \sim \mathcal{O}(1)$.

It follows from Equation (203) with $\mathcal{L} \rightarrow l$ and Equation (204) that

$$\sigma_b = g_b G(\rho, T) (b^2 \rho_d)^{n_b/2}, \quad (205)$$

where $g_b = \alpha/c$. We find that this back stress model in conjunction with our evolution equations provides very good fits to stress-strain data; see Section 6. Our fits yield $g_b = 0.1$ and $n_b = 2/3$, hence $n_b \sim \mathcal{O}(1)$ as expected. Nevertheless, future research to obtain a solid theoretical foundation for a back stress model is needed.

6 Results

In this final section we present comparisons of our (1D) model predictions to quasi-static and Hopkinson bar stress-strain data on OFE copper over a range of temperatures and strain rates (Chen and Gray III, 2004). For stress-strain curves measured experimentally, the plastic strain rate is nearly constant and the material density also remains very near to its value at ambient pressure. Consequently, the evolution of the immobile and mobile dislocation densities is governed by Equations (188) and (189). Since the pileup strain $\sim \rho_m \rho_i^{-1/2}$ and the dislocation densities increase with strain, it follows that ϵ_p increases with the strain and that $\epsilon < \epsilon_p(\epsilon)$ at sufficiently small strains. Our working assumption in fitting our model to stress-strain data is that $\epsilon < \bar{\epsilon}_p(\epsilon)$ up to the maximum strains in the stress-strain data.

Overall, six of the eleven $g_{\text{subscript}}$ and the value of P_{FR} for OFE copper were determined from fitting to the data. The values of these model parameters are given in Table 1, and this parameter set is used for all results shown here (i.e., they are utilized across a wide range of strain rates and temperature without adjustment). The parameter set chosen for use in a model can have notable

impact on the results, and when fitting to data the parameter set is generally not unique (e.g., see (Henry de Frahan, Belof, Cavallo, Raevsky, Ignatova, Lebedev, Ancheta, El-dasher, Florando, Gallegos, Johnsen, and LeBlanc, 2015)). Recent efforts have used more sophisticated methods to both optimize and quantify uncertainties in such parameter sets used in larger length scale approaches (Savage, Feng, and Knezevic, 2021; Walters, Biswas, Lawrence, Francom, Luscher, Fredenburg, Moran, Sweeney, Sandberg, Ahrens, and Bolme, 2018). While such work is very valuable, in this work, we have not attempted to fine-tune the values of the parameters using sophisticated numerical methods to optimize agreement with the data. Furthermore, the current model predictions were made in the single crystal limit (i.e., $D \rightarrow \infty$), thus $g_{s\partial} = g_{\partial} = 0$. While the data taken by Chen and Gray III (2004) was most likely using polycrystalline samples, an average grain size was not reported. Rather than try to approximate an average grain size, we assume a single crystal.

Table 1: Model parameter values for OFE copper calculations. No attempt was made to fine-tune the values to optimize agreement with the data. $g_{subscript}$ values that are not included in this table were taken equal to zero.

g_{sn}	g_{ami}	g_{xx}	g_{tx}	g_{ax}	g_{FR}	P_{FR}
0.05	0.01	1	0.1	0.4	0.1	0.1

For all simulations, we assumed an initial total dislocation density of 10^9 cm^{-2} with $\rho_{io} = 2 \times 10^8 \text{ cm}^{-2}$ and $\rho_{mo} = 8 \times 10^8 \text{ cm}^{-2}$; it follows that $\epsilon_{po} = 0.03$. In addition, the material properties for copper at room temperature and ambient pressure are given as: $b = 0.255 \text{ nm}$, $\rho_0 = 9.02 \text{ g cm}^{-3}$, $T_m = 1358 \text{ K}$ and $G = 46.5 \text{ GPa}$. Recall that the dislocation density evolution equations are also combined with the kinetic equation initially developed in Hunter and Preston (2015). In the original kinetic equation model, a constant drag coefficient was employed, which we also do for the simulations completed here. We used $B = 0.001 \text{ Poise}$ for all simulations. We note that the model is not limited to a constant drag coefficient, and later work has expanded this aspect of the model to include a drag coefficient dependence on temperature, pressure, and dislocation velocity (Blaschke et al., 2020a,b). Finally, the single and double cross-slip energies are decreasing functions of the stacking fault energy, γ . Unfortunately, there is a very large uncertainty in the value of γ for copper. This uncertainty is manifest in an extensive compilation of experimental and theoretical/computational values of γ published by Zhang, Grabowski, Körmann, Ruban, Gong, Reed, Hickel, and Neugebauer (2018). The mean of the 18 experimental values (we exclude two results with $\gamma \geq 150 \text{ mJ m}^{-2}$) is 56 mJ m^{-2} . The 37 theoretical/computational values, the majority of which were obtained at $T = 0$, range from 18 mJ m^{-2} to 78 mJ m^{-2} with a mean value of 43 mJ m^{-2} . In carrying out our model fits to stress-strain data at room temperature we assumed $\gamma = 50 \text{ mJ m}^{-2}$ which is the overall average of the experimental and theoretical/computational values in the compilation of Zhang et al. (2018).

Figure 5(a) presents the stress-strain results from the model as compared to experimental data (Chen and Gray III, 2004) for a temperature of 298K and strain rates of 0.001 s^{-1} , 1 s^{-1} , and 2000 s^{-1} . This is a relatively wide-range of strain rates, and the model produces reasonable fits in all cases. The model is applicable to higher strain rates as well, however this would require additional data for comparison. In addition, the shock generation term would also need to be included in the evolution equation for these cases. [Ultimately the results shown in Figure 5\(a\) are due to four primary mechanisms: Frank-Read source generation, athermal cross-slip, mobile-immobile](#)

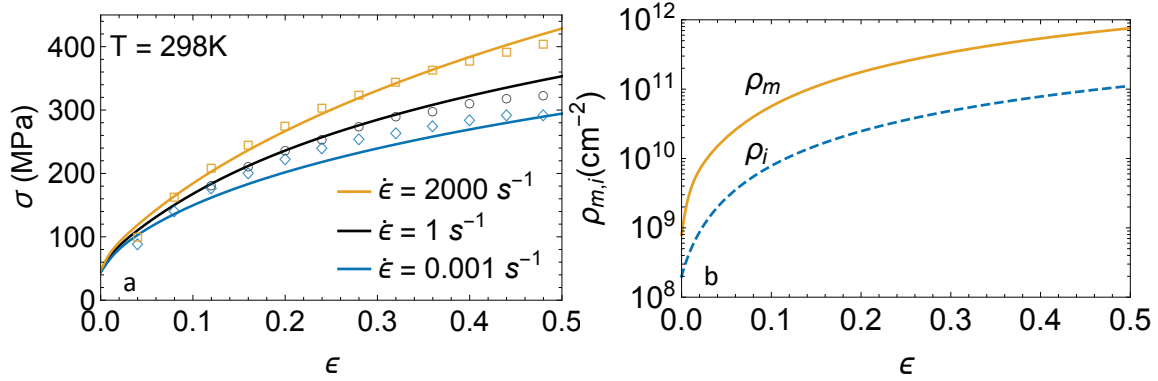


Figure 5: Figure (a) shows the model fit (solid curve) compared to room-temperature stress-strain data on OFE copper for strain rates of 0.001 s^{-1} , 1 s^{-1} , and 2000 s^{-1} . Figure (b) shows the evolution of the mobile and immobile dislocation densities for the case of 2000 s^{-1} .

annihilation, and storage in the network. While the corresponding parameters are non-zero, the thermally activated terms, thermally activated cross-slip and double cross-slip, will not substantially contribute to the dislocation density evolution at room temperature. In addition, Figure 5(b) shows the evolution of the mobile and immobile dislocation densities for this loading case. Overall, the predicted evolution of the network and mobile dislocations densities are found to be physically reasonable. The network density increases from $\sim 10^8\text{ cm}^{-2}$ to $\sim 10^{10-12}\text{ cm}^{-2}$ at strains $\sim 50\%$ and the mobile density increases from $\sim 10^9\text{ cm}^{-2}$ to $\sim 10^{11-12}\text{ cm}^{-2}$ at $\epsilon \sim 0.5$. We confirmed that $\epsilon < \bar{\epsilon}_p(\epsilon)$, as assumed.

Figure 6 presents the model predictions for higher temperatures, ranging from 673K-1073K, and at a strain rate of 2000 s^{-1} . For these cases, temperature dependent mechanisms, such as thermally activated cross-slip and screw-screw annihilation (g_{tx}), and double cross-slip with Koehler multiplication and dipole formation (g_{xx}), are active and play a larger role in the dislocation density evolution. This is in contrast to the dislocation evolution at room and lower temperatures, where we found that single and double cross-slip are negligible. Overall, the fits in Figure 6 are reasonable, however there is more error in these predictions with respect to the experimental data than seen in the room temperature data.

We highlight that in order to achieve the fits shown in Figure 6 an additional temperature dependence of the intrinsic stacking fault energy, γ , was included. For $\dot{\epsilon} \leq 10^4\text{ s}^{-1}$ and $\rho_{i,m} \in (10^8\text{ cm}^{-2}, 10^{12}\text{ cm}^{-2})$, the value of d_p , the stacking fault width on the primary plane, is very nearly independent of strain rate and dislocation density, but increases with increasing T . The reason for this is that $b\hat{\sigma} \ll \gamma$ at these rates and dislocation densities, therefore $d_p(\hat{\sigma}, T) \approx d_p(0, T) = G(\rho_0, T)b^2/16\pi\gamma$ and γ decreases with T . This dependence has been shown in recent computational results (Zhang et al., 2018; Li and Schönecker, 2017; Zhang and Korzhavyi, 2020), which exhibit a decrease in the stacking fault energies of Al, Ni, Cu, and Au with increasing temperature. In the case of copper they found a decrease from about 42 mJ m^{-2} at $T = 0$ to about 20 mJ m^{-2} at 1200K . They also emphasize that the temperature dependence of the stacking fault energy is unknown experimentally.

Considering the activation energies for single and double cross-slip, it follows that $E_x(\hat{\sigma}, T) \approx E_x(0, T)$ and $E_{xx}(\hat{\sigma}, T) \approx E_{xx}(0, T)$, where the T dependence is due primarily to γ . Since $\hat{\sigma}$ is negligible in the expressions for d_p , E_x and E_{xx} at $\dot{\epsilon} \leq 10^4\text{ s}^{-1}$, these quantities depend only on T ,

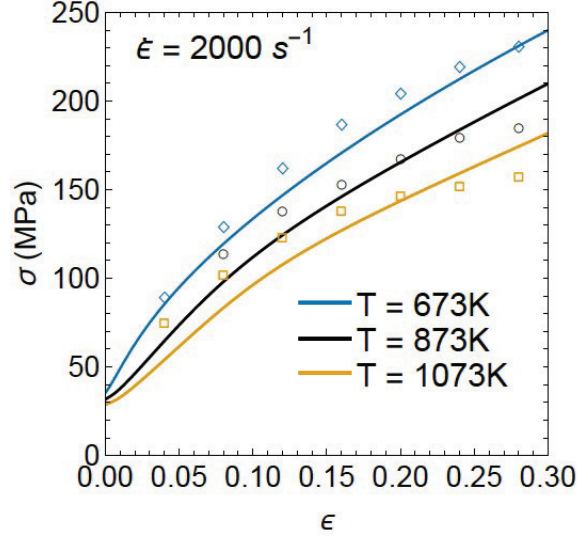


Figure 6: Model fit (solid curve) compared to stress-strain data on OFE copper at 673K, 873K, and 1073K and 2000 s^{-1}

hence for the isothermal stress-strain data under consideration the integrations in Equations (167) and (171) governing the Koehler generation of mobile and immobile dislocation are trivially carried out with the result

$$\begin{aligned} \frac{d\rho_m^{xx}}{d\epsilon} &= g_{xx} \frac{\bar{v}}{bd_p \dot{\epsilon}} \exp\left[-\frac{E_{xx}(n=2)}{k_B T}\right] \epsilon, \\ \frac{d\rho_i^{xx}}{d\epsilon} &= \frac{2}{\pi} g_{xx} \frac{\bar{v}}{bd_p \dot{\epsilon}} \exp\left[-\frac{E_{xx}(n=1)}{k_B T}\right] \epsilon. \end{aligned} \quad (206)$$

The evolution equations for single cross-slip are

$$\frac{d\rho_m^x}{d\epsilon} = \frac{d\rho_i^x}{d\epsilon} = -g_{ax} \frac{h_c}{b} \rho_i - g_{tx} \rho_m \frac{\bar{v}}{\dot{\epsilon}} \exp\left(-\frac{E_x}{k_B T}\right). \quad (207)$$

For $\dot{\epsilon} \gg 10^4 \text{ s}^{-1}$, $d_p \rightarrow b$, thus $E_x \rightarrow 0$ and $E_{xx} \rightarrow 0$.

Our fits to Hopkinson bar data at temperatures of 673 K, 873 K, and 1073 K are shown in Figure 6. We obtained satisfactory fits by setting $g_{tx} = 0.1$ and $g_{xx} = 1$, and then adjusting the value of γ at each temperature to optimize the fit. We found that γ decreases from 43 mJ m^{-2} at 673 K to 21 mJ m^{-2} at 1073 K; the temperature dependence in mJ m^{-2} is given by

$$\gamma(T) = 112 - 0.134T + 0.0000462T^2, \quad 600K < T < 1200K. \quad (208)$$

The activation energies E_x and E_{xx} are decreasing functions of γ ; see Equations (20), (56), and (160). For $\gamma(T)$ in Equation (208) the activation energies increase very nearly linearly with temperature within the temperature range of $600 \text{ K} < T < 1200 \text{ K}$

$$\begin{aligned} E_x(T) &= 0.00361 + 0.00232T, \\ E_{xx}(T, n=1) &= 0.0697 + 0.00215T, \\ E_{xx}(T, n=2) &= 0.318 + 0.00218T, \quad 600K < T < 1200K. \end{aligned} \quad (209)$$

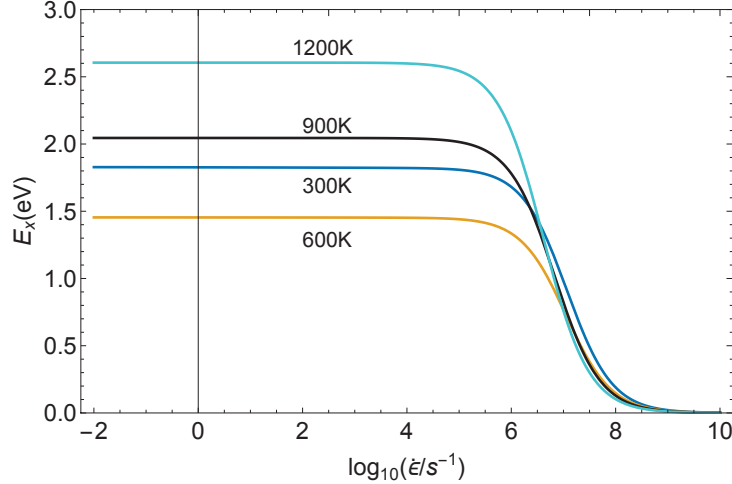


Figure 7: Single cross-slip activation energy as a function of strain rate and temperature, including a temperature dependence of the intrinsic stacking fault energy, γ .

These activation energies, with the inclusion of $\gamma(T)$, are plotted in Figures 7 and 8 for $T = 600$ K, 900 K, and 1200 K as functions of plastic strain rate. The activation energies at 300 K for $\gamma = 50$ mJ/m² are also shown in these figures. Figures 7 and 8 can be compared to Figures 2 and 4 that present similar information, however without the inclusion of a temperature dependent stacking fault energy. It can be seen that $\gamma(T)$ has a significant effect on the activation energies, essentially reversing the dependence of the activation energies on temperature. Interestingly, however, there appears to be competing effects. In Figures 7 and 8, the activation energies initially decrease from 300 K to 600 K, which follows the trend presented previously in Figures 2 and 4. Then from 600 K to 900 K, and then to 1200 K, the activation energies increase, in contrast to the trends shown in Figures 2 and 4.

A strong dependence of E_x on temperature could have a significant impact on theoretical/computational investigations of creep as well as on alloy design. Poirier (1976) investigated cross-slip as a recovery process that controls high-temperature creep and stated that his formalism was “relevant to such problems as the influence of the stacking fault energy on the creep rate of solid-solution alloys”. Cross-slip has been proposed as a creep controlling mechanism in several *fcc* (Jaffe and Dorn, 1962; Caillard and Martin, 1989) and hexagonal-close packed (*hcp*) (Vagarali and Langdon, 1981; Flynn, Mote, and Dorn, 1961) metals. Uniaxial creep tests on Zircaloy-4 (*hcp* below ~ 800 C) in 2015 at high stresses and temperatures of 300-600 C indicated that the cross-slip of screw dislocations was the creep rate controlling mechanism (Kombaiah and Murty, 2015). In these and other studies of cross-slip the Friedel (1959) and Poirier (1976) models of the activation energy were generally used. In these models the activation energy is a function of the applied stress and the stacking fault energy but not of the temperature. Given our result for the temperature dependence of E_x in Equation (209), that is, a linear increase with temperature, the Arrhenius exponentials are nearly constant at high temperatures, which might have a consequential effect on calculated creep rates. However, we emphasize and maintain that further research on the temperature dependence of the cross-slip activation energy is most definitely needed to inform studies of high-temperature creep in alloys.

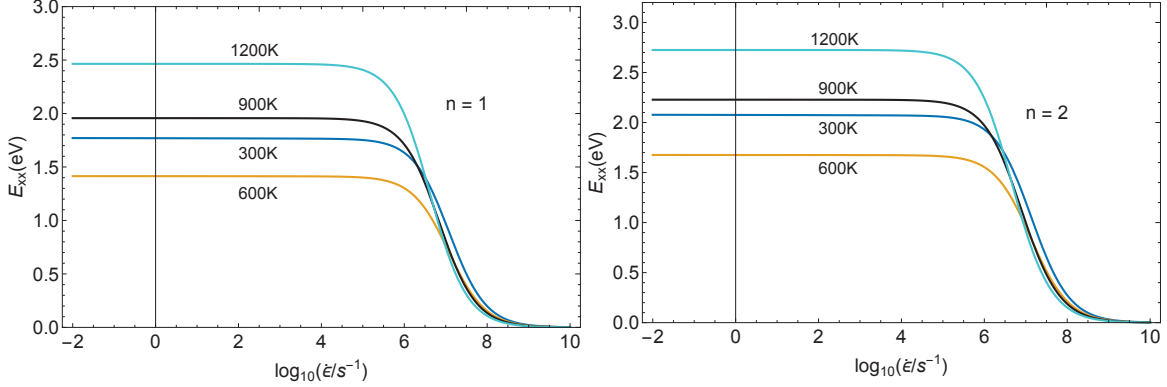


Figure 8: Double cross-slip activation energy as a function of strain rate and temperature for (a) $h = 0.22$ nm ($n = 1$) and (b) $h = 0.44$ nm ($n = 2$). This formulation of the double cross-slip activation energy includes a temperature dependence of the intrinsic stacking fault energy, γ .

6.1 Strain Rate Sensitivity

With reasonable comparison to stress-strain curves across both wide ranges of strain rate and temperature, we now compare our model predictions for the strain rate sensitivity (SRS) of copper to experimental and numerical results in the literature. We first consider the extensive room-temperature experimental results of Follansbee (1985) on OFHC copper at strain rates from 10^{-4} s^{-1} to 10^3 s^{-1} . Rates from 10^{-4} s^{-1} to 10^{-1} s^{-1} were achieved using a screw-driven mechanical testing machine and data at rates from 10^{-1} s^{-1} to 10^2 s^{-1} were measured using a servo-hydraulic testing machine with an optical extensometer. Data at the higher rates were obtained using a Hopkinson bar. The grain diameters were in the range 30 μm - 50 μm . Comparison of the Follansbee (1985) data at $\epsilon = 0.05, 0.1, 0.15,$ and 0.2 to those of Chen and Gray III (2004) used to extract our model parameters shows differences in measured flow stresses of at most 27 MPa ($\sim 10\%$) at 1 s^{-1} and a strain of 0.2 .

The strain rate sensitivity is defined as

$$m = \left. \frac{d \log \sigma}{d \log \dot{\epsilon}} \right|_{T, \epsilon}. \quad (210)$$

We note that m at fixed T and ϵ is nearly constant for 10^{-4} $s^{-1} \geq \dot{\epsilon} \leq 10^3$ s^{-1} . In the following we consider the mean SRS, $\bar{m}(T, \epsilon)$, over this range of strain rates.

In Figure 9(a) we compare our model prediction for $\bar{m}(298\text{K}, \epsilon)$ to the values of \bar{m} obtained from the room temperature Follansbee (1985) data at $\epsilon = 0.05, 0.1, 0.15,$ and 0.2 . Both our model and the Follansbee (1985) data exhibit an increase in \bar{m} with strain and \bar{m} lies within the range 0.005 - 0.02 . By way of comparison, Dao, Lu, Shen, and Suresh (2006) considered the SRS of ultrafine crystalline (ufc) copper with nanoscale twins. They provide a summary of experimental m values for ufc copper deformed at rates from 10^{-7} s^{-1} to 10^{-2} s^{-1} ; the values of m varied from 0.005 (ufc Cu without twins) to 0.036 , hence the SRS of ufc copper is comparable to that of polycrystalline copper.

Our model predictions for the temperature dependence of \bar{m} for five values of the plastic strain are shown in Figure 9(b). At $T \lesssim 500\text{K}$ the mean SRS increases with strain. In contrast, for $T \gtrsim 500\text{K}$ the mean SRS decreases with strain and approaches a value of approximately 0.032 . At a

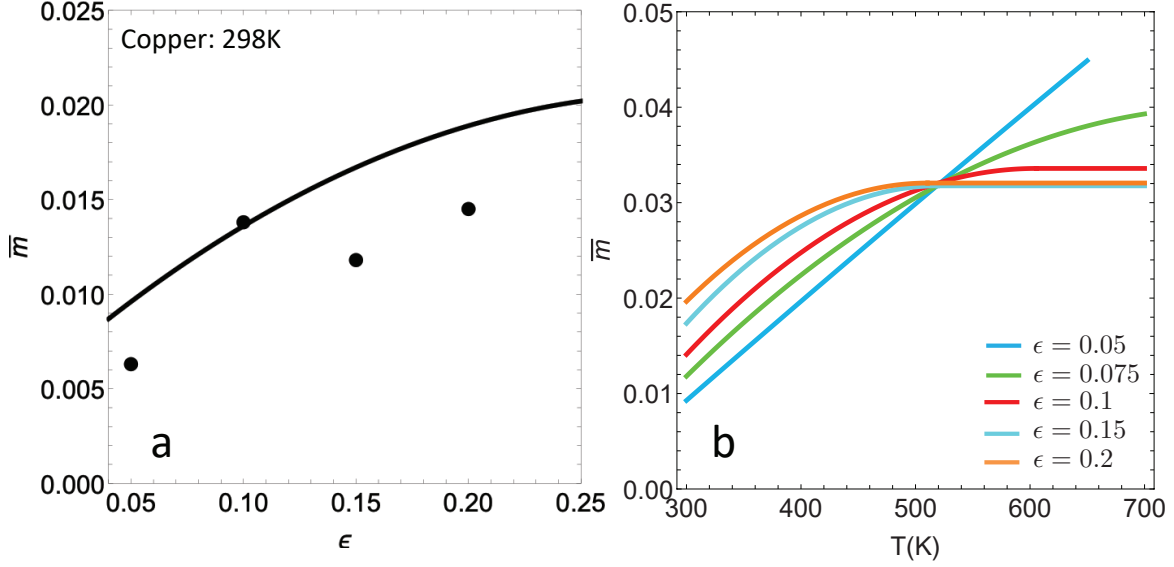


Figure 9: (a) Comparison of our model prediction for $\bar{m}(298\text{K}, \epsilon)$ (solid curve) to the values of \bar{m} obtained from the Follansbee (1985) data at $\epsilon = 0.05, 0.1, 0.15,$ and 0.2 . (b) Our model prediction for the temperature dependence of \bar{m} at plastic strains from 5% to 20% in copper.

given strain it is seen that \bar{m} is an increasing function of the temperature. It is interesting that a recent study of the SRS of nanograined nickel at rates from 0.001 s^{-1} to 0.04 s^{-1} likewise shows that the SRS increases with temperature (Wei, Wu, Wie, Nastasi, and Wang, 2021). Specifically, $m = 0.015, 0.027, 0.037,$ and 0.042 at room temperature, $473\text{K}, 573\text{K},$ and $673\text{K},$ respectively; these values of m are very close to those of copper as seen in Figure 9(b). In another study of the SRS of nanocrystalline nickel (Schwaiger, Moser, Dao, Chollacoop, and Suresh, 2003) it is concluded that the relatively soft grain-boundary affected zones (7 - 10 lattice parameters thick) have an SRS of 0.03 at strain rates in the range $0.01 \text{ s}^{-1} - 0.1 \text{ s}^{-1}$.

We encourage the experimental community to obtain stress-strain data on polycrystalline copper at temperatures $\gtrsim 300 \text{ C}$ and rates from 10^{-4} s^{-1} to 10^3 s^{-1} in order to check our model prediction that \bar{m} decreases with strain and approaches a constant.

7 Summary

In summary, we have developed dislocation evolution equations for both mobile and immobile dislocation densities by explicitly accounting for specific mechanisms known to be active in *fcc* polycrystals. Within this model, mechanisms considered to influence both the mobile and immobile dislocation density include storage in the network due to junction forming mechanisms and along grain boundaries, mobile-immobile annihilation, athermal and thermal single cross-slip, double cross-slip (as a generation mechanism, and including dipole formation), generation via Frank-Read (FR) sources and shock induced generation. Additionally, mobile-mobile dislocation annihilation and grain boundary nucleation are accounted for in the evolution of the mobile dislocation density, however these mechanisms do not directly influence the immobile dislocation density. By accounting for all these mechanisms explicitly in the evolution equations, this model is capable of investigating

the dominate active mechanisms that control the different stages of work hardening.

To create a complete model, these evolution equations must be combined with a constitutive relationship that describes the relationship between the plastic strain rate and flow stress. Here, we utilize a kinetic equation developed previously (Hunter and Preston, 2015). With all three equations, the model is applicable over a wide range of strain rates (up to roughly 10^{10} s^{-1}), at pressures up to 1000 GPa, and temperatures up to melt. Thus, all dislocation mechanisms derived to formulate the evolution equations include an explicit dependence on material density and temperature (unless the term is athermal). This formulation will provide unprecedented insight into the interplay and relative importance of various mechanisms in different regimes of temperature, strain and strain rate. To illustrate the applicability of the model, comparisons are made to stress-strain data that cover a wide range of temperatures and strain rates. The model shows very good comparison to all data sets, including up to relatively large amounts of strain accumulation (out to 50% strain).

While many mechanisms are accounted for in the dislocation evolution equations, there are still some known mechanisms that have yet to be included. For example, twinning and detwinning (Lee, Im, Yoo, Bitzek, Kiener, Richter, Kim, and Oh, 2013; Wang, Li, Anderoglu, Zhang, Misra, Huang, and Hirth, 2010; Shute, Myers, Xie, Li, Barbee Jr., Hodge, and Weertman, 2011; D’Hondt, Doquet, and Couzinié, 2021), and spiral or single arm sources (Oh et al., 2009; Cui, Lin, Liu, and Zhuang, 2014) are not accounted for in the model. In addition, the dislocation evolution equations are currently limited to dislocation mechanisms and processes that are operative in *fcc* polycrystals. For example, to extend the model to consider body-centered cubic (*bcc*) crystal structures the cross-slip terms would need to be formulated differently, as the Friedel-Escaig (FE) mechanism is not applicable for these materials. Similarly, twinning and detwinning have been shown to have a dominate role in the deformation of *hcp* materials (Yoo, 1981; Britton, Dunne, and Wilkinson, 2015; He, Li, Wang, and Mao, 2020), a mechanism not considered here, as just mentioned. These are examples as to how the model could be adjusted for alternate crystal structures. Such work will be the subject of future study. There are no such limitations in the formulation of the kinetic equation, which is formulated in detail in Hunter and Preston (2015). Additionally, while the model does account for some dislocation-grain boundary interactions, there are other known mechanisms that could be included, namely slip transfer, dislocation absorption and glide within boundaries, grain boundary migration and grain boundary sliding. The present model does have a dependence on the average grain size, however grain boundaries, including their structure and morphology, are not explicitly resolved. Finally, we also highlight that both the dislocation density evolution equations and the kinetic equation are currently only able to account for isotropic material response, which may not be appropriate for materials that exhibit strongly anisotropic material behavior. Extension of the model to consider anisotropy would be possible with further development, namely the mobile dislocation density would need refinement so that evolution on individual slip systems could be accounted for. This would require the construction of coupling terms between the mobile dislocation density on each slip system and the immobile dislocation density, which we view as the primary theoretical challenge in such an extension.

8 Acknowledgements

AH and DLP acknowledge valuable discussions with Dr. Kevin Larkin. AH and DLP also gratefully acknowledge support from the Materials project within the Physics and Engineering Models (PEM) Subprogram element of the Advanced Simulation and Computing (ASC) Program at Los Alamos National Laboratory (LANL). LANL, an affirmative action/equal opportunity employer, is operated

by Triad National Security, LLC, for the National Nuclear Security Administration of the U.S. Department of Energy under contract 89233218NCA000001.

Appendix A Mass Density Variations

In this model we account for dislocation density evolution up to pressures of several 100 GPa. Such extreme pressures can occur under shock wave loading, ramp wave loading, and laser drive (Remington et al., 2006; Krygier, Powell, McNaney, Huntington, Prisbrey, Remington, Rudd, Swift, Wehrenberg, Arsenlis, and Park, 2019; Brown, Davis, and Seagle, 2021). The changes in material density can be large; for example, the Hugoniot compression for a 80 GPa shock wave in 2034 Al is approximately 1.5 (Wallace, 1981). In the absence of dislocation storage, recovery, and multiplication processes, the dislocation density changes as a result of material density variations. The length of dislocation in a material element (fixed mass) varies as $\eta^{-1/3}$, where $\eta = \rho/\rho_0$ is the material compression (the current material density, ρ , divided by the material density under ambient conditions, ρ_0), and the volume of the material element varies as η^{-1} ; hence

$$\rho_{m,i}^\eta = \eta^{2/3} \rho_{m,i}^{(0)}, \quad (211)$$

where $\rho_{m,i}^{(0)}$ is the ambient mobile and immobile dislocation density. Differentiating Equation (211) with respect to time yields

$$\frac{d\rho_{m,i}^\eta}{dt} = \frac{2}{3} \frac{\dot{\rho}}{\rho} \rho_{m,i}^\eta. \quad (212)$$

This expression also accounts for density variations due to thermal expansion or contraction, but those density variations are small and generally negligible.

Quantities with dimensions of length scale in an obvious way with density, i.e., as $\rho^{-1/3}$. Specifically, the density dependence of the Burgers vector is

$$b(\rho) = b(\rho_0) \left(\frac{\rho_0}{\rho} \right)^{1/3}; \quad (213)$$

similar expressions hold for the mean grain diameter, D , and the critical dipole height, h_c (see Section 3.2.5). We note here that this density dependence is also indicated through a dependence on time in later equations. For example, $b(t)$ may be used rather than $b(\rho)$.

Perhaps less obvious is how the shear modulus and melt temperature vary with material density. Several models have been developed to address this issue (Guinan and Steinberg, 1975; Burakovsky et al., 2003; Burakovsky and Preston, 2006). In this work, we employ the model developed by Preston and Wallace (1992) for the shear modulus, and a Lindemann melt criterion for the melt temperature, which utilizes the analytic model developed by Burakovsky and Preston (2004) for the density-dependent Grüneisen parameter. These relationships are described next, however, we first note that other models may be used within this framework if so desired.

The ρ - and T -dependent shear modulus was modeled by Preston and Wallace (1992) as the product of the ρ -dependent $T = 0$ shear modulus and a linearly decreasing function of the reduced temperature T/T_m where $T_m(\rho)$ is the density-dependent melting temperature

$$G(\rho, T) = G(\rho, 0) \left(1 - \beta \frac{T}{T_m(\rho)} \right); \quad (214)$$

β is a constant. The Lindemann melting criterion relates $T_m(\rho)$ to the density-dependent Grüneisen parameter, $\Gamma(\rho)$:

$$\frac{d \ln T_m(\rho)}{d \ln \rho} = 2 \left(\Gamma(\rho) - \frac{1}{3} \right). \quad (215)$$

An analytic model of $\Gamma(\rho)$ has been constructed by Burakovsky and Preston (2004)

$$\Gamma(\rho) = \frac{1}{2} + \frac{\gamma_1}{\rho^{1/3}} + \frac{\gamma_2}{\rho^q}, \quad \gamma_1, \gamma_2, q = \text{constant}, q > 1, \quad (216)$$

through consideration of its low- and ultrahigh-pressure limits. For copper, $\gamma_1 = 1.87 (\text{g/cc})^{1/3}$, $\gamma_2 = 2.31 \times 10^4 (\text{g/cc})^q$, and $q = 4.7$. Equations (215) and (216) yield a model for the melting temperature as a function of density

$$T_m(\rho) = T_m(\rho_0) \left(\frac{\rho}{\rho_0} \right)^{1/3} \exp \left\{ 6 \gamma_1 \left(\frac{1}{\rho_0^{1/3}} - \frac{1}{\rho^{1/3}} \right) + \frac{2 \gamma_2}{q} \left(\frac{1}{\rho_0^q} - \frac{1}{\rho^q} \right) \right\}. \quad (217)$$

The melting temperature and the shear modulus along the solidus approximately satisfy the relation

$$\frac{G(\rho, T_m(\rho))}{\rho T_m(\rho)} = \frac{G(\rho_0, T_m(\rho_0))}{\rho_0 T_m(\rho_0)}, \quad (218)$$

which can be justified on the basis of either the theory of dislocation mediated melting or from the theory of the Debye solid (Burakovsky et al., 2003).

It follows from Equations (214), (217), and (218) that

$$G(\rho, 0) \equiv G_0(\rho) = G(\rho_0, 0) \left(\frac{\rho}{\rho_0} \right)^{4/3} \exp \left\{ 6 \gamma_1 \left(\frac{1}{\rho_0^{1/3}} - \frac{1}{\rho^{1/3}} \right) + \frac{2 \gamma_2}{q} \left(\frac{1}{\rho_0^q} - \frac{1}{\rho^q} \right) \right\}, \quad (219)$$

which completes our model for the ρ - and T -dependent shear modulus.

Appendix B FR source formation: 2D model

B.1 Size distributions of FR configurations

In this two-dimensional model, the intersections of the immobile dislocations with the glide plane are idealized as a square lattice of sites with lattice constant \mathcal{L}_i . Previous to node formation the mobile dislocation is parallel to the rows of unit cells, which is along the x -axis. One of the intersections nodes is taken to be the origin while the second is within an angle $\xi > 0$ from the x -axis. Define $r_n = (n - \frac{1}{2})\mathcal{L}_i$. Out to radius r_n the total number of lattice points at angles $\leq \xi$ is

$$\frac{\pi r_n^2}{\mathcal{L}_i^2} \frac{\xi}{\pi/2} = 2\xi \left(n - \frac{1}{2} \right)^2, \quad (220)$$

hence the number of lattice sites between r_n and r_{n+1} is

$$\frac{2\xi}{\mathcal{L}_i^2} (r_{n+1}^2 - r_n^2) = 4n\xi. \quad (221)$$

The probability that a particular site between r_n and r_{n+1} is occupied is

$$P_{FR} (1 - P_{FR})^{4n\xi - 1}. \quad (222)$$

The formation probability for a FR configuration of length $(1/2)(r_n + r_{n+1}) = n\mathcal{L}_i$ is the product of the probability that all sites out to $n\mathcal{L}_i$ are unoccupied

$$(1 - P_{FR})^{2\xi(n-1/2)^2} \approx (1 - P_{FR})^{2n(n-1)\xi} \quad (223)$$

and the probability, Equation (222), that a single site between r_n and r_{n+1} is occupied

$$P(n) = 4n\xi(1 - P_{FR})^{2n(n+1)\xi-1}. \quad (224)$$

At this point we make the reasonable approximation that $\xi \approx \pi/4 \approx 3/4$. The subsequent development could be trivially carried out for arbitrary $\xi < \pi/2$, but by fixing ξ we eliminate a model parameter. With the additional approximation $(3/2)n(n+1) - 1 \approx 3n^2/2$ we obtain

$$P(n) = 3n P_{FR} (1 - P_{FR})^{3n^2/2}. \quad (225)$$

The corresponding size distribution of FR configurations is

$$f^{FR}(\lambda) = \mathcal{N} \mathcal{L}_i^{-1} \cdot 3 \frac{\lambda}{\mathcal{L}_i} P_{FR} (1 - P_{FR})^{(3/2)(\lambda/\mathcal{L}_i)^2} \theta(\lambda - \mathcal{L}_i). \quad (226)$$

Normalizing the integral of f^{FR} over $\lambda \in [0, \infty)$ to unity results in

$$f^{FR}(\lambda) = \mathcal{L}_i^{-1} \ln \left(\frac{1}{1 - P_{FR}} \right) \frac{3\lambda}{\mathcal{L}_i} (1 - P_{FR})^{(3/2)(\lambda^2/\mathcal{L}_i^2 - 1)} \theta(\lambda - \mathcal{L}_i). \quad (227)$$

B.2 Operating probability

$$P_{op}(s) = 1 + \left[(1 - P_{FR})^{(3/2)(C_\Omega^2/s^2 - 1)} - 1 \right] \theta(C_\Omega - s), \quad (228)$$

where $s = \hat{\sigma} \mathcal{L}_i / Gb$. Our exponential approximation is

$$P_{op}(s) \approx 1 - e^{-\chi s / C_\Omega}, \quad (229)$$

where

$$\chi = 3 \ln^{-1/2} \left(\frac{1}{1 - P_{FR}} \right) (1 - P_{FR})^{(3/2)[\ln^{-1}(1/(1 - P_{FR})) - 1]}. \quad (230)$$

B.3 Size distribution of FR sources

$$f_{op}^{FR}(\lambda) = \mathcal{L}_i^{-1} \ln \left(\frac{1}{p} \right) \frac{3\lambda}{\mathcal{L}_i} p^{(3/2)\lambda^2/\mathcal{L}_i^2} \left\{ \frac{\theta(\lambda - C_\Omega \lambda_c) \theta(C_\Omega \lambda_c - \mathcal{L}_i)}{p^{(3/2)(\lambda_c/\mathcal{L}_i)^2} - p^{3/2} g_{sn}^2} + \frac{\theta(\lambda - \mathcal{L}_i) \theta(\mathcal{L}_i - C_\Omega \lambda_c)}{p^{3/2} - p^{3/2} g_{sn}^2} \right\} \theta(\mathcal{L}_i / g_{sn} - \lambda), \quad (231)$$

where $p = 1 - P_{FR}$.

B.4 Mean FR source size

The mean FR source size in the two-dimensional FR configuration formation model is given by

$$\begin{aligned} \frac{\bar{\lambda}}{\mathcal{L}_i} &= \frac{u(1/g_{sn}, p) - u(C_\Omega/s, p)}{p^{(3/2)(C_\Omega/s)^2} - p^{3/2} g_{sn}^2} \theta(C_\Omega - s) + \frac{u(1/g_{sn}, p) - u(1, p)}{p^{3/2} - p^{3/2} g_{sn}^2} \theta(s - C_\Omega), \\ u(x, p) &= \sqrt{\frac{\pi}{6}} \frac{\operatorname{erf} \left(\sqrt{\frac{3}{2}} \ln \left(\frac{1}{p} \right) x \right)}{\sqrt{\ln(1/p)}} - x p^{3x^2/2}. \end{aligned} \quad (232)$$

Appendix C Smooth Approximations to $\mathcal{B}_{m,i}$ and $\dot{\mathcal{B}}_{m,i}$

In the case of mobile dislocation we propose

$$\mathcal{B}_m(t, t'; \Omega) \approx \tanh(x^2) - \frac{1}{2} \tanh\left(\frac{x - \Omega}{w}\right) - \frac{1}{2}, \quad (233)$$

where $\Omega \equiv \Omega(t')$ and $x = (t - t')/\tau_p(t')$. Here w is the half-width of the approximation at $x = \Omega(t')$. For the immobile dislocation

$$\begin{aligned} \mathcal{B}_i(t, t'; \Omega) &\approx \left(\Omega - \frac{1}{2}\right) \left\{ 1 + \tanh\left[\frac{2\Omega - 1}{\Omega(\Omega - 1)} \left(x - \frac{\Omega + 1}{2}\right) - \tanh^{-1}\left(\frac{1}{2\Omega - 1}\right)\right] \right\}, \\ &\equiv \left(\Omega - \frac{1}{2}\right) [1 + h(x, \Omega)]. \end{aligned} \quad (234)$$

This form was constructed to agree in value and slope with $\mathcal{B}_i(t, t')$ in Equation (99) at $x = (\Omega + 1)/2$, i.e. $(t_p + t_{op})/2$, and have the correct asymptotic value. The time derivatives of Equations (233) and (234) are

$$\begin{aligned} \dot{\mathcal{B}}_m(t, t'; \Omega) &= \frac{1}{\tau_p(t')} \left\{ 2x \operatorname{sech}^2(x^2) - \frac{1}{2w} \operatorname{sech}^2\left(\frac{x - \Omega}{w}\right) \right\}, \\ \dot{\mathcal{B}}_i(t, t''; \Omega) &= \frac{2}{\tau_p(t')} \frac{(\Omega - 1/2)^2}{\Omega - 1} [1 - h^2(x, \Omega)]. \end{aligned} \quad (235)$$

Appendix D Network Evolution at Low Pressures, Room Temperature and Constant Strain Rate

We assume $P \ll B$, where B is the bulk modulus, thus the material density is essentially that at $P = 0$. When the deformation is taking place around room temperature and below, terms representing thermally activated processes, i.e. single cross-slip and the Koehler mechanism, are generally negligible in the evolution equations for plastic strain rates above quasi-static, $\dot{\epsilon} \geq 1 \text{ s}^{-1}$. In that case, the immobile density evolution equation is approximately independent of the mobile density:

$$\frac{d\rho_i}{dt} = \left\{ g_{s\partial} \frac{1}{bD} + (g_{sn} - g_{ami}) \frac{1}{b} \sqrt{\rho_i(t)} - g_{ax} \frac{h_c}{b} \rho_i(t) \right\} \dot{\epsilon}. \quad (236)$$

Writing this equation as

$$\frac{d\rho_i}{d\epsilon} = C_1 + 2C_2 \sqrt{\rho_i} - C_3 \rho_i, \quad (237)$$

its solution may be expressed

$$(x_\infty + x_+) \frac{\epsilon}{\epsilon_c} = x_\infty \ln\left(\frac{x_\infty - 1}{x_\infty - x(\epsilon)}\right) - x_+ \ln\left(\frac{x_+ + x(\epsilon)}{x_+ + 1}\right) \quad (238)$$

where

$$\begin{aligned} \sqrt{\rho_{i\infty}} &= \frac{C_2}{C_3} \left\{ \sqrt{1 + \frac{C_1 C_3}{C_2^2}} + 1 \right\}, & \sqrt{\rho_{i+}} &= \frac{C_2}{C_3} \left\{ \sqrt{1 + \frac{C_1 C_3}{C_2^2}} - 1 \right\}, \\ x_\infty &= \sqrt{\rho_{i\infty} / \rho_{i0}}, & x_+ &= \sqrt{\rho_{i+} / \rho_{i0}}, & x(\epsilon) &= \sqrt{\rho_i(\epsilon) / \rho_{i0}}, & \epsilon_c &= 2 / C_3. \end{aligned} \quad (239)$$

Note that the evolution with strain is independent of the strain rate. The immobile dislocation density approaches $\rho_{i\infty}$ as $\epsilon \rightarrow \infty$.

Consider $D \rightarrow \infty$, thus $C_1 = 0$. It follows that $\sqrt{\rho_{i\infty}} = 2C_2/C_3$ and $\sqrt{\rho_{i+}} = 0$, hence $x_+ = 0$. We can now solve Equation (238) for ρ_i

$$\sqrt{\rho_i(\epsilon)} = \sqrt{\rho_{i\infty}} + (\sqrt{\rho_{i0}} - \sqrt{\rho_{i\infty}}) \exp\left(-\frac{\epsilon}{\epsilon_c}\right). \quad (240)$$

References

- Agarwal, G., Valisetty, R. R., Dongare, A. M., 2020. Shock wave compression behavior and dislocation density evolution in al microstructures at the atomic scales and the mesoscales. *International Journal of Plasticity* 128, 102678.
- Aitken, Z. H., Sorkin, V., Zhang, Y.-W., 2019. Atomistic modeling of nanoscale plasticity in high-entropy alloys. *Journal of Materials Research* 34 (9), 1509–1532.
- Anderson, P., Hirth, J., Lothe, J., 2017. *Theory of Dislocations*. Cambridge University Press.
- Arrhenius, S., 1889. Ueber die reaktionsgeschwindigkeit bei der inversion von rohrzucker durch säuren. *Zeitschrift für Physikalische Chemie* 4, 226–248.
- Ashby, M. F., 1970. Deformation of plastically non-homogeneous materials. *Philosophical Magazine* 21 (170), 399.
- Austin, R. A., McDowell, D. L., 2011. A dislocation-based constitutive model for viscoplastic deformation of fcc metals at very high strain rates. *International Journal of Plasticity* 27, 1–24.
- Austin, R. A., McDowell, D. L., 2012. Parameterization of a rate-dependent model of shock-induced plasticity for copper, nickel, and aluminum. *International Journal of Plasticity* 32-33, 134–154.
- Balint, D. S., Deshpande, V. S., Needleman, A., Van der Giessen, E., 2008. Discrete dislocation plasticity analysis of the grain size dependence of the flow stress of polycrystals. *International Journal of Plasticity* 24, 2149–2172.
- Bertin, N., Capolungo, L., 2018. A fft-based formulation for discrete dislocation dynamics in heterogeneous media. *Journal of Computational Physics* 355, 366–384.
- Bertin, N., Sills, R. B., Cai, W., 2020. Frontiers in the simulation of dislocations. *Annual Review of Materials Research* 50, 437–464.
- Beyerlein, I. J., Hunter, A., 2016. Understanding dislocation mechanics at the mesoscale using phase field dislocation dynamics. *Philosophical Transactions of the Royal Society A* 374, 20150166.
- Blaschke, D. N., Hunter, A., Preston, D. L., 2020a. Analytic model of the remobilization of pinned glide dislocations: Including dislocation drag from phonon wind. *International Journal of Plasticity* 131, 102750.
- Blaschke, D. N., Mottola, E., Preston, D. L., 2020b. Dislocation drag from phonon wind in an isotropic crystal at large velocities. *Philosophical Magazine* 100 (5), 571–600.

- Bonneville, J., Escaig, B., Martin, J. L., 1988. A study of cross-slip activation parameters in pure copper. *Acta Metallurgica* 36, 1989–2002.
- Borbely, A., Driver, J. H., 2005. Dislocation density measurements by x-ray profile analysis in texture components of deformed metals. *Archive of Metallurgy and Materials* 50, 65.
- Braga, F., Kestenbach, H. J., Meyers, M. A., 1978. *The Effect of Polycrystallinity on the Shock Response of Copper*. Military Institute of Engineering, unpublished, Rio de Janeiro.
- Britton, T. B., Dunne, F. P. E., Wilkinson, A. J., 2015. On the mechanistic basis of deformation at the microscale in hexagonal close-packed metals. *Philosophical Transactions of the Royal Society A* 471, 20140881.
- Brown, J. L., Davis, J.-P., Seagle, C. T., 2021. Multi-megabar dynamic strength measurements of ta, au, pt, and ir. *Journal of Dynamic Behavior of Materials* 7, 196–206.
- Burakovsky, L., Greeff, C. W., Preston, D. L., 2003. Analytic model of the shear modulus at all temperatures and densities. *Physical Review B* 67 (9), 094107.
- Burakovsky, L., Preston, D. L., 2004. Analytic model of the grüneisen parameter all densities. *Journal of Physics and Chemistry of Solids* 65 (8-9), 1581–1587.
- Burakovsky, L., Preston, D. L., 2006. Shear moduli at all pressures: Generalized guinan-steinberg formula. *Journal of Physics and Chemistry of Solids* 67, 1930.
- Caillard, D., Martin, J. L., 1989. Some aspects of cross-slip mechanisms in metals and alloys. *Journal de Physique* 50 (18), 2455–2473.
- Caillard, D., Martin, J. L., 2003. *Thermally Activated Mechanisms in Crystal Plasticity*. Elsevier Ltd., Oxford.
- Cao, L., Hunter, A., Beyerlein, I. J., Koslowski, M., 2015. The role of partial mediated slip during quasi-static deformation of 3d nanocrystalline metals. *Journal of the Mechanics and Physics of Solids* 78, 415–426.
- Chakraborty, P., Ma, T., Cui, Y., Hunter, A., Cao, L., 2021. Elastic interaction-induced anisotropic growth of dislocation loop arrays. *Journal of Materials Research* 36, 3426–3435.
- Chandrasekhar, S., 1943. Stochastic problems in physics and astronomy. *Reviews of Modern Physics* 15 (1), 1–89.
- Chen, B., Jiang, J., Dunne, F. P. E., 2018. Is stored energy density the primary meso-scale mechanistic driver for fatigue crack nucleation? *International Journal of Plasticity* 101, 213–229.
- Chen, S. R., Gray III, G. T., 2004. Summary of the ptw model parameters. Tech. Rep. LA-CP-04-0920, Los Alamos National Laboratory.
- Chou, Y. T., 1972. Pileups of elliptical dislocation loops in a hexagonal crystal. *Journal of Applied Physics* 43 (8), 3271.
- Courtney, T. H. (Ed.), 2005. *Mechanical Behavior of Materials*, second edition Edition. Waveland Press, Inc.

- Cui, Y. N., Lin, P., Liu, Z. L., Zhuang, Z., 2014. Theoretical and numerical investigations of single arm dislocation source controlled plastic flow in fcc micropillars. *International Journal of Plasticity* 55, 279–292.
- Dao, M., Lu, L., Shen, Y. F., Suresh, S., 2006. Strength, strain-rate sensitivity and ductility of copper with nanoscale twins. *Acta Materialia* 54, 5421–5432.
- Das, S., Hofman, F., Tarleton, E., 2018. Consistent determination of geometrically necessary dislocation density from simulations and experiments. *International Journal of Plasticity* 109, 18–42.
- de Sousa, T. G., Sordi, V. L., Brandao, L. P., 2018. Dislocation density and texture in copper deformed by cold rolling and ecap. *Materials Research* 21, 1–6.
- Dehm, G., Legros, M., Heiland, B., 2006. In-situ tem straining experiments of al films on polymide using a novel fib design for specimen preparation. *Journal of Materials Science* 41, 4484–4489.
- Deo, C., Chen, E., Dingreville, R., 2021. Atomistic modeling of radiation damage in crystalline materials. *Modelling and Simulation in Materials Science and Engineering* in press.
- D’Hondt, C., Doquet, V., Couzinié, J. P., 2021. Direct monitoring of twinning/detwinning in a twip steel under reversed cyclic loading. *Materials Science and Engineering A* 814, 141250.
- Djordjevic, N., Vignjevic, R., Kiely, L., Case, S., De Vuyst, T., Campbell, J., Hughes, K., 2018. Modelling of shock waves in fcc and bcc metals using a combined continuum and dislocation kinetic approach. *International Journal of Plasticity* 105, 211–224.
- Dou, W., Wang, B., Geng, X., Fan, J., 2019. Grain size effect on strain-rate dependence of mechanical properties of polycrystalline copper. *Materials Science and Technology* 35 (11), 1401–1404.
- El-Azab, A., Po, G., 2018. Continuum dislocation dynamics: Classical theory and contemporary models. In: Andreoni, W., Yip, S. (Eds.), *Handbook of Materials Modeling*. Springer, Cham, Switzerland, pp. 1–25.
- Escaig, B., 1968. Cross-slip of screw dislocations in cubic structure with centered faces. *Journal de Physique* 29 (2-3), 225–239.
- Essmann, U., Mughrabi, H., 1979. Annihilation of dislocations during tensile and cyclic deformation and limits of dislocations densities. *Philosophical Magazine A* 40 (6), 731–756.
- Fan, H., Wang, Q., El-Awady, J. A., Raabe, D., Zaiser, M., 2021. Strain rate dependency of dislocation plasticity. *Nature Communications* 12 (1845), 1–11.
- Faradjian, A. K., Friedman, L. H., Chrzan, D. C., 1999. Frank-read sources within a continuum simulation. *Modelling and Simulation in Materials Science and Engineering* 7 (4), 479–494.
- Fleischer, R. L., 1959. Cross slip of extended dislocations. *Acta Metallurgica* 7 (2), 134–135.
- Flynn, P. W., Mote, J., Dorn, J. E., 1961. On the thermally activated mechanisms of prismatic slip in magnesium single crystals. *Transactions of the Metallurgical Society of the AIME* 221, 1148–1153.
- Follansbee, P. S., 1985. High strain rate deformation in fcc metals and alloys. Tech. Rep. LA-UR-85-3026, Los Alamos National Laboratory.

- Follansbee, P. S., Kocks, U. F., 1988. A constitutive description of the deformation of copper based on the use of the mechanical threshold stress as an internal state variable. *Acta Metallurgica* 36 (1), 81–93.
- Frank, F. C., Read, W. T. (Eds.), 1950. *Symposium on Plastic Deformation in Crystalline Solids*. Carnegie Inst. Tech., Pittsburgh.
- Friedel, J. (Ed.), 1957. *Dislocations and Mechanical Properties of Crystals*. Wiley, New York.
- Friedel, J., 1959. Internal stresses and fatigue in metals. Ed. GM Raßweiler and WJ Grube, Amsterdam, 220.
- Friedel, J. (Ed.), 1964. *Dislocations*. Pergamon Press, Oxford.
- Gao, C. Y., Zhang, L. C., 2012. Constitutive modelling of plasticity of fcc metals under extremely high strain rates. *International Journal of Plasticity* 32-33, 121–133.
- Gilman, J. J., 1997. Mechanism of the koehler dislocation multiplication process. *Philosophical Magazine A* 76 (2), 329–336.
- Guinan, M., Steinberg, D., 1975. Simple approach to extrapolating measured polycrystalline shear moduli to very high pressure. *Journal of Physics and Chemistry of Solids* 36, 829.
- Hähner, P., Bay, K., Zaiser, M., 1998. Fractal dislocation patterning during plastic deformation. *Physical Review Letters* 81, 2470.
- Hänggi, P., Talkner, P., Borkovec, M., 1990. Reaction-rate theory: fifty years after kramers. *Reviews of Modern Physics* 62 (2), 251–341.
- Hansen, N., Ralph, B., 1982. The strain and grain size dependence of the flow stress of copper. *Acta Metallurgica* 30, 411–417.
- He, Y., Li, B., Wang, C., Mao, S. X., 2020. Direct observation of dual-step twinning nucleation in hexagonal close-packed crystals. *Nature Communications* 11 (2483), 1–8.
- Henry de Frahan, M. T., Belof, J. L., Cavallo, R. M., Raevsky, V. A., Ignatova, O. N., Lebedev, A., Ancheta, D. S., El-dasher, B. S., Florando, J. N., Gallegos, G. F., Johnsen, E., LeBlanc, M. M., 2015. Experimental and numerical investigations of beryllium strength models using the rayleigh-taylor instability. *Journal of Applied Physics* 117, 225901.
- Hu, Q., Zhao, F., Fu, H., Li, K., Liu, F., 2017. Dislocation density and mechanical threshold stress in ofhc copper subjected to shpb loading and plate impact. *Materials Science and Engineering A* 695, 230–238.
- Hughes, D. A., Hansen, N., 2018. The microstructural origin of work hardening stages. *Acta Materialia* 148, 374–383.
- Hunter, A., Leu, B., Beyerlein, I. J., 2018. A review of slip transfer: applications of mesoscale techniques. *Journal of Materials Science* 53, 5584–5603.
- Hunter, A., Preston, D. L., 2015. Analytic model of the remobilization of pinned glide dislocations from quasi-static to high strain rates. *International Journal of Plasticity* 70, 1–29.

- Hunter, A., Zhang, R. F., Beyerlein, I. J., 2014. The core structure of dislocation and their relationship to the material γ -surface. *Journal of Applied Physics* 115, 134314.
- Hunter, A., Zhang, R. F., Beyerlein, I. J., Germann, T. C., Koslowski, M., 2013. Dependence of equilibrium stacking fault width in fcc metals on the γ -surface. *Modelling and Simulation in Materials Science and Engineering* 21 (025015), 1–19.
- Jacques, A., Vallino, F., Serbena, F., George, A., 2000. Dislocation multiplication in silicon at the onset of plasticity observed by in situ synchrotron x-ray topography. *Journal of Physics: Condensed Matter* 12 (49), 10045–10058.
- Jaffe, N., Dorn, J. E., 1962. Effect of stress on creep rate of high-purity aluminum in cross-slip region. *Transactions of the Metallurgical Society of the AIME* 224, 1167–1173.
- Jiang, J., Britton, T. B., Wilkinson, A. J., 2012. Accumulation of geometrically necessary dislocations near grain boundaries in deformed copper. *Philosophical Magazine Letters* 92 (11), 580–588.
- Jiang, J., Britton, T. B., Wilkinson, A. J., 2013. Evolution of dislocation density distributions in copper during tensile deformation. *Acta Materialia* 61, 7227–7239.
- Johnston, W. G., Gilman, J. J., 1960. Dislocation multiplication in lithium fluoride crystals. *Journal of Applied Physics* 31 (4), 632–643.
- Kacher, J., Eftink, B. P., Cui, B., Robertson, I. M., 2014. Dislocation interactions with grain boundaries. *Current Opinion in Solid State & Materials Science* 18, 227–243.
- Kanel, G. I., Zaretsky, E. B., Razorenov, S. V., Ashitkov, S. I., Fortov, V. E., 2017. Unusual plasticity and strength of metals at ultra-short load durations. *Physics-Uspekhi* 60 (5), 490–508.
- Khan, A. S., Liu, H., 2012. Variable strain rate sensitivity in an aluminum alloy: Response and constitutive modeling. *International Journal of Plasticity* 36, 1–14.
- Kim, H., Mathew, N., Luscher, D. J., Hunter, A., 2021. Phase field dislocation dynamics (pffd) modeling of non-schmid behavior in bcc metals informed by atomistic simulations. *Journal of the Mechanics and Physics of Solids* 152, 104460.
- Kim, S. D., Park, J. Y., Park, S. J., Jang, J., Moon, J., Ha, H.-Y., Lee, C.-H., Kang, J.-Y., Shin, J.-H., Lee, T.-H., 2019. Direct observation of dislocation plasticity in high-mn lightweight steel by *in-situ* tem. *Scientific Reports* 9, 15171.
- Kocks, U. F., 1967. On internal stresses due to a quasi-uniform distribution of dislocations. *Acta Metallurgica* 15 (8), 1415–1417.
- Kocks, U. F., Mecking, H., 2003. Physics and phenomenology of strain hardening: the fcc case. *Progress in Material Science* 48 (3), 171–273.
- Koehler, J. S., 1952. The nature of work-hardening. *Physical Review* 86 (1), 52–59.
- Kombaiah, B., Murty, K. L., 2015. Dislocation cross-slip controlled creep in zircaloy-4 at high stresses. *Materials Science and Engineering A* 623, 114–123.

- Kreyca, J., Kozeschink, E., 2018. State parameter-based constitutive modelling of stress strain curves in al-mg solid solutions. *International Journal of Plasticity* 103, 67–80.
- Krygier, A., Powell, P. D., McNaney, J. M., Huntington, C. M., Prisbrey, S. T., Remington, B. A., Rudd, R. E., Swift, D. C., Wehrenberg, C. E., Arsenlis, A., Park, H.-S., 2019. Extreme hardening of pb at high pressure and strain rate. *Physical Review Letters* 123, 205701.
- Kubin, L. P., Devincre, B., Hoc, T., 2006. Inhibited dynamic recovery and screw dislocation annihilation in multiple slip of fcc single crystals. *Philosophical Magazine* 86 (25-26), 4023–4036.
- Kubin, L. P., Devincre, B., Hoc, T., 2008. Modeling dislocation storage rates and mean free paths in face-centered cubic crystals. *Acta Materialia* 56 (20), 6040–6049.
- Kubin, L. P., Devincre, B., Hoc, T., 2009. Dynamic recovery and its orientation dependence in face-centered cubic crystals. *Acta Materialia* 57 (8), 2567–2575.
- Kubin, L. P., Mortensen, A., 2003. Geometrically necessary dislocations and strain-gradient plasticity: a few critical issues. *Scripta Materialia* 48, 119–125.
- Langdon, N., 2000. Explicit expression for stress field of a circular dislocation loop. *Theoretical and Applied Fracture Mechanics* 33 (3), 219–231.
- Lavenstein, S., El-Awady, J. A., 2019. Micro-scale fatigue mechanisms in metals: Insights gained from small-scale experiments and discrete dislocation simulations. *Current Opinion in Solid State & Materials Science* 23, 100765.
- Lee, S., Im, J., Yoo, Y., Bitzek, E., Kiener, D., Richter, G., Kim, B., Oh, S. H., 2013. Reversible cyclic deformation mechanism of gold nanowires by twinning-detwinning transition evidenced from *in situ* tem. *Nature Communications* 5 (3033), 1–10.
- Li, K. Q., Zhang, Z. J., Yan, J. X., Yang, J. B., Zhang, Z. F., 2020. Mechanism transition of cross slip with stress and temperature in face-centered cubic metals. *Journal of Materials Science & Technology* 57, 159–171.
- Li, X., Schönecker, S., 2017. First-principles prediction of the stacking fault energy of gold at finite temperature. *Acta Materialia* 135, 88–95.
- Liu, G., Cheng, X., Wang, J., Chen, K., Shen, Y., 2017. Improvement of nonlocal peierls-nabarro models. *Computational Materials Science* 131, 69–77.
- Lloyd, J. T., Clayton, J. D., Becker, R., McDowell, D. L., 2014. Simulation of shock wave propagation in single crystal and polycrystalline aluminum. *International Journal of Plasticity* 60, 118–144.
- Luscher, D. J., Mayeur, J. R., Mourad, H. M., Hunter, A., Kenamond, M., 2016. Coupling continuum dislocation transport with crystal plasticity for application to shock loading conditions. *International Journal of Plasticity* 76, 111–129.
- Ma, A., Roters, F., 2004. A constitutive model for fcc single crystals based on dislocation densities and its application to uniaxial compression of aluminum single crystals. *Acta Materialia* 52, 3603–3612.

- Mao, Z. N., An, X. H., Z., L. X., Wang, J. T., 2018. Opposite grain size dependence of strain rate sensitivity of copper at low vs high strain rates. *Materials Science and Engineering A* 738, 430–438.
- Mayeur, J. R., Mourad, H. M., Luscher, D. J., Hunter, A., Kenamond, M. A., 2016. Numerical implementation of a crystal plasticity model with dislocation transport for high rate applications. *Modelling and Simulation in Materials Science and Engineering* 24, 045013.
- Meyers, M. A., 1994. *Dynamic Behavior of Materials*. John Wiley & Sons, New York.
- Mianroodi, J. R., Svendsen, B., 2015. Atomistically determined phase-field modeling of dislocation dissociation, stacking fault formation, dislocation slip, and reactions in fcc systems. *Journal of the Mechanics and Physics of Solids* 77, 109–122.
- Motz, C., Schöberl, T., Pippan, R., 2005. Mechanical properties of micro-sized copper bending beams machined by the focused ion beam technique. *Acta Materialia* 53, 4269–4279.
- Moulin, A., Condat, M., Kubin, L. P., 1997. Simulation of frank-read sources in silicon. *Acta Materialia* 45 (6), 2339–2348.
- Murr, L. E., Kuhlmann-Wilsdorf, D., 1978. Experimental and theoretical observations on relationship between dislocation cell-size, dislocation density, residual hardness, peak pressure and pulse duration in shock-loaded nickel. *Acta Metallurgica* 26 (5), 847–857.
- Nemat-Nasser, S., Li, Y., 1998. Flow stress of f.c.c. polycrystals with application to ofhc cu. *Acta Materialia* 46 (2), 565–577.
- Nguyen, K., Zhang, M., Amores, V. J., Sanz, M. A., Montans, F. J., 2021a. Computational modeling of dislocation slip mechanisms in crystal plasticity: A short review. *Crystals* 11 (1), 42.
- Nguyen, T., Fensin, S. J., Luscher, D. J., 2021b. Dynamic crystal plasticity modeling of single crystal tantalum and validation using taylor cylinder impact tests. *International Journal of Plasticity* 139, 102940.
- Nye, J. F., 1953. Some geometrical relations in dislocated crystals. *Acta Metallurgica* 1, 153–162.
- Oh, S., Legros, M., Kiener, D., Dehm, G., 2009. *In situ* observation of dislocation nucleation and escape in a submicrometre aluminum single crystal. *Nature Materials* 8, 95–100.
- Ortiz, M., Repetto, E. A., 1999. Nonconvex energy minimization and dislocation structures in ductile single crystals. *Journal of the Mechanics and Physics of Solids* 47 (2), 397–462.
- Pang, B., Jones, I., Chiu, Y., Millett, J., Whiteman, G., Bourne, N., 2014. Orientation dependence of shock induced dislocations in tantalum single crystals. *J. Phys.: Conf. Ser.* 522, 012029.
- Po, G., Mohamed, M. S., Crosby, T., Erel, C., El-Azab, A., Ghoniem, N., 2014. Recent progress in discrete dislocation dynamics and its applications to micro plasticity. *Journal of the Minerals, Metals and Materials Society* 66 (10), 2108–2120.
- Podurets, A. M., Tkachenko, M. I., Ignatova, O. N., Lebedev, A. I., Igonin, V. V., Raevsky, V. A., 2013. Dislocation density in copper and tantalum subjected to shock compression depending on loading parameters and original microstructure. *Physics of Metals and Metallography* 114 (5), 440–447.

- Poirier, J. P., 1976. On the symmetrical role of cross-slip of screw dislocations and climb of edge dislocations as recovery processes controlling high-temperature creep. *Rev. Phys. Appl. (Paris)* 11 (6), 731–738.
- Preston, D. L., Tonks, D. L., Wallace, D. C., 2003. Model of plastic deformation for extreme loading conditions. *Journal of Applied Physics* 93 (1), 211–220.
- Preston, D. L., Wallace, D. C., 1992. A model of the shear modulus. *Solid State Communications* 81 (3), 277–281.
- Püschl, W., 2002. Models for dislocation cross-slip in close-packed crystal structures: a critical review. *Progress in Material Science* 47 (4), 415–461.
- Püschl, W., Schoeck, G., 1993. Calculation of cross-slip parameters in fcc crystals. *Materials Science and Engineering A* 164, 286–289.
- Rao, S. I., Dimiduk, D. M., El-Awady, J. A., Parthasarathy, T. A., Uchic, M. D., Woodward, C., 2013. Spontaneous athermal cross-slip nucleation at screw dislocation intersections in fcc metals in Ni_2 intermetallics investigated via atomistic simulations. *Philosophical Magazine* 93 (22), 3012–3028.
- Rasmussen, T., Jacobsen, K. W., Leffers, T., Pedersen, O. B., 1997. Simulations of the atomic structure, energetics, and cross slip of screw dislocations in copper. *Physical Review B* 56, 2977–2990.
- Rasmussen, T., Vegge, T., Leffers, T., Pedersen, O. B., Jacobsen, K. W., 2000. Simulation of structure and annihilation of screw dislocation dipoles. *Philosophical Magazine A* 80 (5), 1273–1290.
- Ravindran, S., Gandhi, V., Lovinger, Z., Mello, M., Ravichandran, G., 2001. Dynamic strength of copper at high pressures using pressure shear plate experiments. *Journal of Dynamic Behavior of Materials* 7, 248–261.
- Remington, B. A., Allen, P., Bringa, E. M., Hawreliak, J., Ho, D., Lorenz, K. T., Lorenzana, H., McNaney, J. M., Meyers, M. A., Pollaine, S. W. ., Rosolankova, K., Sadik, B., Schneider, M. S., Swift, D., Wark, J., Yaakobi, B., 2006. Material dynamics under extreme conditions of pressure and strain rate. *Materials Science and Technology* 22 (4), 474–488.
- Rodney, D., Le Bouar, Y., Finel, A., 2003. Phase field methods and dislocations. *Acta Materialia* 51 (1), 17–30.
- Rodney, D., Ventelon, L., Clouet, E., Pizzagalli, L., Willaime, F., 2017. Ab initio modeling of dislocation core properties in metals and semiconductors. *Acta Materialia* 124, 663–659.
- Rodríguez-Martínez, J. A., Rodríguez-Millán, M., Rusinek, A., Arias, A., 2011. A dislocation-based constitutive description for modeling the behavior of fcc metals within wide ranges of strain rate and temperature. *Mechanics of Materials* 43 (12), 901–912.
- Rollet, A. D., Kocks, U. F., 1993. A review of the stage of work hardening. *Solid State Phenomena* 35-36, 1–18.

- Roters, F., Raabe, D., Gottstein, G., 2000. Work hardening in heterogeneous alloys – a microstructural approach based on three internal state variables. *Acta Materialia* 48, 4181–4189.
- Ruffini, A., Le Bouar, Y., Finel, A., 2017. Three-dimensional phase-field model of dislocations for a heterogeneous face-centered cubic crystal. *Journal of the Mechanics and Physics of Solids* 105, 95–115.
- Rusinek, A., Klepaczko, J. R., 2001. Shear testing of a sheet steel at wide range of strain rates and a constitutive relation with strain-rate and temperature dependence of the flow stress. *International Journal of Plasticity* 17 (1), 87–115.
- Salvado, F. C., Teixeira-Dias, F., Walley, S. M., Lea, L. J., Cardoso, J. B., 2017. A review on the strain rate dependency of the dynamic viscoplastic response of fcc metals. *Progress in Material Science* 88, 186–231.
- Sandfeld, S., Thawinan, E., Wieners, C., 2015. A link between microstructure evolution and macroscopic response in elasto-plasticity: Formulation and numerical approximation of the higher-dimensional continuum dislocation dynamics theory. *International Journal of Plasticity* 72, 1–20.
- Savage, D. J., Feng, Z., Knezevic, M., 2021. Identification of crystal plasticity model parameters by multi-objective optimization integrating microstructural evolution and mechanical data. *Computer Methods in Applied Mechanics and Engineering* 379, 113747.
- Schoeck, G., 1994. The generalized peierls-nabarro model. *Philosophical Magazine A* 69 (6), 1085–1095.
- Schoeck, G., Seeger, A., 1955. Report on the conference on defects in crystalline solids. Tech. rep., The Physical Society, London.
- Schwaiger, R., Moser, B., Dao, M., Chollacoop, N., Suresh, S., 2003. Some critical experiments on the strain-rate sensitivity of nanocrystalline nickel. *Acta Materialia* 51, 5159–5172.
- Seeger, A., 1955. Bestrahlungsfehlordnung und diffusionsvorgänge in edelmetallen. *Zeitschrift für Naturforschung* 10 (3), 251–253.
- Shanthraj, P., Zikry, M. A., 2011. Dislocation density evolution and interactions in crystalline materials. *Acta Materialia* 59, 7695–7702.
- Sharma, S. M., Turneaure, S. J., Winey, J. M., Rigg, P. A., Sinclair, N., Wang, X., Toyoda, Y., Gupta, Y. M., 2020. Real-time observation of stacking faults in gold shock compressed to 150 gpa. *Physical Review X* 10, 011010.
- Shute, C. J., Myers, B. D., Xie, S., Li, S.-Y., Barbee Jr., T. W., Hodge, A. M., Weertman, J. R., 2011. Detwinning, damage and crack initiation during cyclic loading of cu samples containing aligned nanotwins. *Acta Materialia* 59, 4569–4577.
- Simmons, G., Wang, H., 1971. *Single Crystal Elastic Constants and Calculated Aggregate Properties: A Handbook*. The M.I.T. Press, Cambridge, Massachusetts.
- Starkey, K., Winther, G., El-Azab, A., 2020. Theoretical development of continuum dislocation dynamics for finite-deformation crystal plasticity at the mesoscale. *Journal of the Mechanics and Physics of Solids* 139, 103926.

- Steif, P. S., Clifton, R. J., 1979. On the kinetics of a frank-read source. *Materials Science and Engineering* 41 (2), 251–258.
- Steinberg, D. J., Cochran, S., Guinan, M., 1980. A constitutive model for metals applicable at high-strain rate. *Journal of Applied Physics* 51 (3), 1498–1504.
- Sung, J. H., Kim, J. H., Wagoner, R. H., 2010. A plastic constitutive equation incorporating strain, strain-rate, and temperature. *International Journal of Plasticity* 26 (12), 1746–1771.
- Tonks, D. L., 1993. Deviatoric stresses and plastic strain rates in strong shock waves for six metals. Tech. Rep. LA-12641, Los Alamos National Laboratory.
- Turneure, S. J., Renganathan, P., Winey, J. M., Gupta, Y. M., 2018. Twinning and dislocation evolution during shock compression and release of single crystals: Real-time x-ray diffraction. *Physical Review Letters* 120, 265503.
- Vagarali, S. S., Langdon, T. G., 1981. Deformation mechanisms in hcp metals at elevated temperatures -i. creep behavior of magnesium. *Acta Metallurgica* 29, 1969–1982.
- Van der Giessen, E., Needleman, A., 1995. Discrete dislocation plasticity: a simple planar model. *Modelling and Simulation in Materials Science and Engineering* 3, 689–735.
- Vegge, T., Rasmussen, T., Leffers, T., Pedersen, O. B., Jacobsen, K. W., 2001. Atomistic simulations of cross-slip of jogged screw dislocation in copper. *Philosophical Magazine Letters* 81 (3), 137–144.
- Wallace, D. C., 1981. Nature of the process of overdriven shocks in metals. *Physical Review B* 24, 5607.
- Walters, D. J., Biswas, A., Lawrence, E. C., Francom, D. C., Luscher, D. J., Fredenburg, D. A., Moran, K. R., Sweeney, C. M., Sandberg, R. L., Ahrens, J. P., Bolme, C. A., 2018. Bayesian calibration of strength parameters using hydrocode simulations of symmetric impact shock experiments of al-5083. *Journal of Applied Physics* 124, 205105.
- Wang, J., Li, N., Anderoglu, O., Zhang, X., Misra, A., Huang, J. Y., Hirth, J. P., 2010. Detwinning mechanisms for growth twins in face-centered cubic metals. *Acta Materialia* 58, 2262–2270.
- Wang, Z. Q., Beyerlein, I. J., LeSar, R., 2007. The importance of cross-slip in high-rate deformation. *Modelling and Simulation in Materials Science and Engineering* 15 (6), 675–690.
- Washburn, J., 1965. Intersection cross slip. *Applied Physics Letters* 7 (7), 183–185.
- Wei, B., Wu, W., Wie, D., Nastasi, M., Wang, J., 2021. Strength, plasticity thermal stability and strain rate sensitivity of nanograined nickel with amorphous ceramic grain boundaries. *Acta Materialia* 212, 116918.
- Williamson, G. K., Smallman, R. E., 1956. Dislocation densities in some annealed and cold-worked metals from measurements on the x-ray debye-scherrer spectrum. *Philosophical Magazine* 1, 34.
- Wolf, H., 1960. Die aktivierungsenergie für die quergleitung aufgespaltener schraubenversetzungen. *Zeitschrift für Naturforschung Part A - Astrophysik Physik und Physikalische Chemie* 15 (3), 180–193.

- Xiang, Y., Wei, H., Ming, P., Weinan, E., 2008. A generalized peierls-nabarro model for curved dislocations and core structures of dislocation loops in al and cu. *Acta Materialia* 56 (7), 1447–1460.
- Xu, S., Chen, X., 2019. Modeling dislocations and heat conduction in crystalline materials: atomistic/continuum coupling approaches. *International Metals Reviews* 64 (7), 407–438.
- Xu, Y., 2021. A non-local methodology for geometrically necessary dislocations and application to crack tips. *International Journal of Plasticity* 140, 102970.
- Xu, Y., Balint, D. S., Dini, D., 2019. A new hardness formula incorporating the effect of source density on indentation response: A discrete dislocation plasticity analysis. *Surface and Coatings Technology* 374, 763–773.
- Yaghoobi, M., Voyiadjis, G. Z., 2018. The effects of temperature and strain rate in fcc and bcc metals during extreme deformation rates. *Acta Materialia* 151, 1–10.
- Yaghoobi, M., Voyiadjis, G. Z., Sundararaghavan, V., 2021. Crystal plasticity simulation of magnesium and its alloys: A review of recent advances. *Crystals* 11 (4), 435.
- Yoo, M., 1981. Slip, twinning, and fracture in hexagonal close-packed metals. *Metallurgical Transactions A* 12A, 409–418.
- Zerilli, F. J., Armstrong, R. W., 1987. Dislocation-mechanics-based constitutive relations for material dynamics calculations. *Journal of Applied Physics* 61 (5), 1816–1825.
- Zhang, J., Korzhavyi, P. A., 2020. First principles investigation on thermodynamic properties and stacking fault energy of paramagnetic nickel at high temperature. *Metals* 10 (3), 319.
- Zhang, T., Jiang, J., Shollock, B. A., Britton, T. B., Dunne, F. P. E., 2015. Slip localization and fatigue crack nucleation near a non-metallic inclusion in polycrystalline nickel-based superalloy. *Materials Science and Engineering A* 641, 328–339.
- Zhang, X., Grabowski, B., Körmann, F., Ruban, A. V., Gong, Y., Reed, R. C., Hickel, T., Neugebauer, J., 2018. Temperature dependence of the stacking-fault gibbs energy for al, cu, and ni. *Physical Review B* 98, 224106.
- Zhou, H., Huang, C., Sha, X., Xiao, L., Ma, X., Werner Höppel, H., Göken, M., Wu, X., Ameyama, K., Han, X., Zhu, Y., 2019. *In-situ* observation of dislocation dynamics near heterostructured interfaces. *Materials Research Letters* 7 (9), 376–382.
- Zikry, M. A., Kao, M., 1996. Inelastic microstructural failure mechanisms in crystalline materials with high angle grain boundaries. *Journal of the Mechanics and Physics of Solids* 44 (11), 1765–1798.